Hydraulic modelling of a network of mining galleries used as a lower reservoir of a pumping-turbining scheme

Auteur : Ceresetti, Sara
Promoteur(s) : Erpicum, Sebastien; Archambeau, Pierre
Faculté : Faculté des Sciences appliquées
Diplôme : Master en ingénieur civil des constructions, à finalité spécialisée en "civil engineering"
Année académique : 2022-2023
URI/URL : http://hdl.handle.net/2268.2/17718

Master's Thesis : Hydraulic modelling of a network of mining galleries used as a lower reservoir of a pumping-turbining scheme

Sara Ceresetti

Hydraulics in environmental and civil engineering

Master's thesis for the degree of Civil Construction Engineer by Ceresetti Sara

Academic supervisors : Sébastien Erpicum, Pierre Archambeau

Jury : Serge Brouyère, Miroslav Marence

University of Liège - Faculty of Applied Sciences

Academic Year 2022-2023

Acknowledgements

I would first of all like to express my gratitude to my academic supervisors, Sébastien ERPICUM and Pierre ARCHABEAU, for their patience, their availability and above all their judicious advice, which helped to fuel my reflection. I would like to thank him for giving me the opportunity to study such an interesting subject.

I would like to thank Grégory THONARD, Maxime MATHIEU and Claude LHERMEROUT for their invaluable help throughout this work, for their availability and for the construction of the setup.

I would also like to thank Miroslav MARENCE for his availability, his precious advice that help me for my reflexion.

A big thank you to Romain THELEN for reviewing my report and giving me valuable advice on writing it.

Finally, I would like to thank my parents for their unfailing support during my studies.

Résumé

Ce travail de fin d'études porte sur l'étude hydraulique d'un système de pompage turbinage souterrain réutilisant des anciennes galeries minières. Dans le contexte de crise énergétique actuel, le stockage d'énergie est devenu un élément clé. Ce système permettrait de stocker de l'énergie comme un système classique de pompage turbinage mais avec au moins un des deux réservoirs souterrains. Ce travail se focalise sur l'étude du réservoir qui serait composé d'anciennes galeries minières. L'objectif est l'étude de cet écoulement de manière expérimentale et numérique afin de permettre de mieux comprendre ce qui se passe et avoir une idée plus claire de la façon d'utiliser ce type de système.

L'étude expérimentale porte aussi bien sur le remplissage que sur la vidange du réservoir inférieur. L'étude a ainsi permis de mettre en lumière les différentes phases présentes. Trois grandes phases ont été identifiées lors du remplissage. La première est la propagation du front d'ondes. La deuxième phase est la réflexion de ce front d'ondes. La troisième phase est le remplissage uniforme des conduites. Lors de la vidange, deux grandes phases ont été observées. Dans un premier temps la vidange est conditionnée par la pompe. Cette phase représente 60 % du temps de vidange totale quelque soit le débit de vidange et permet de vidanger 85 % de la hauteur d'eau du réservoir. Dans un second temps, la vidange est uniquement régie par la géométrie des conduites.

Une fois validé par les résultats de laboratoire, le modèle numérique offre la possibilité d'étudier un réservoir de taille réelle. Le réservoir étudié possède un volume de 2 506 990.93 m^3. Il permet de stocker 2561.7 MWh. Une étude de l'influence du débit sur l'écoulement met en évidence la différence du temps de remplissage ainsi que les différentes amplitudes du front d'ondes. La vitesse de propagation du front n'augmente pas proportionnellement avec le débit. Pour un débit de 250 m^3/s, la vitesse de propagation peut atteindre plus de 5 m/s. Un autre paramètre étudié est l'influence de la zone d'injection sur la mise en pression de celle-ci. Pour des raisons de stabilité de sol, l'écoulement doit rester à surface libre. Lors de l'arrivée de l'eau dans les conduites, un écoulement critique est observé, avant que la hauteur d'eau n'augmente. La hauteur critique a été étudiée comme une fonction du débit et de la section d'injection. Le diamètre de la section d'injection doit être au moins trois à quatre fois plus grand que le diamètre des conduites pour ne pas mettre en charge cette zone. Lorsque la section d'injection est deux fois plus grande ou de la même taille que la section des conduites, la section sera mise sous pression sauf lorsque les débits sont plus faible, 50 m^3/s ou 100 m^3/s par exemple.

L'influence du frottement est également un paramètre important. Les revêtements possibles pour ce type de système peuvent être du béton projeté ou simplement de la roche pure. L'étude est à la base menée sur des conduites en PVC qui n'entrainent presque aucun frottement. Un revêtement en béton entraine par contre un frottement plus important sans aucune oscillation complémentaire. La vitesse de propagation est quant à elle plus faible. Lorsque le revêtement est composé uniquement de roches, la vitesse de propagation représente la moitié de celle d'un revêtement en PVC. Des oscillations supplémentaires apparaissent également.

Mots clés : Pompage-turbinage souterrain, stockage d'énergie, modèle numérique, volumes finis, hydraulique, conduites circulaires, laboratoire, expérimental, anciennes mines

Abstract

This master's thesis involves the hydraulic study of an underground pumped-turbine system using old mining galleries. In the current energy crisis, energy storage has become a key element. This system would make it possible to store energy in the same way as a conventional pumped-turbine system, but with at least one of the two underground reservoirs. This work focuses on the study of the reservoir, which would be made up of old mining galleries. The aim is to study this flow experimentally and numerically in order to gain a better understanding of what is happening and to have a clearer idea of how to use this type of system.

The experimental study covered both the filling and emptying of the lower tank. The study highlighted the different phases involved. Three main phases were identified during filling. The first is the propagation of the wave front. The second phase is the reflection of this wave front. The third phase is the uniform filling of the pipes. During emptying, two main phases have been observed. In the first phase, emptying is conditioned by the pump. This phase accounts for 60 % of the total emptying time, whatever the emptying rate, and enables 85 % of the tank's head of water to be emptied. In the second phase, emptying is governed solely by the geometry of the pipes.

Once the numerical model has been validated by laboratory results, it can be used to study a full-scale reservoir. The reservoir studied has a volume of 2,506,990.93 m^3 and can store 2561.7 MWh. A study of the influence of the flow rate on the flow shows the difference in filling time and the different amplitudes of the wave front. The propagation speed of the wave front does not increase proportionally with the flow rate. For a flow rate of 250 m^3/s, the propagation speed can reach more than 5 m/s. Another parameter studied was the influence of the injection zone on its pressurisation. For reasons of soil stability, the flow must remain at a free surface. When water enters the pipes, a critical flow is observed, before the water height increases. The critical head was studied as a function of flow rate and injection cross-section. The diameter of the injection section must be at least three to four times greater than the diameter of the pipes so as not to overload this area. When the injection cross-section is twice as large or the same size as the cross-section of the pipes, the cross-section will be pressurised, except when the flow rates are lower, in the order of 50 m^3/s to 100 m^3/s.

The influence of friction is also an important parameter. Possible linings for this type of system can be shotcrete or simply pure rock. The study is based on PVC pipes, which cause almost no friction. A concrete lining, on the other hand, causes greater friction without any additional oscillation. The speed of propagation is also lower. When the pavement consists entirely of rock, the propagation speed is half that of a PVC pavement. Additional oscillations also occur.

Key words: Underground pumping-turbining, energy storage, numerical model, finite volumes, hydraulics, circular pipes, laboratory, experimental, old mines

Table of contents

List of Figures

List of Tables

Nomenclature

Part III : Methodology

ΔH	Difference of height [m]
η	Efficiency [Pa]
D	Diameter of the galleries [m]
L_{tot}	Total length of the galleries [m]
P	Power [MW]
Q	Flow rate [m^3/s]
Q_{labo}	Flow rate used in laboratory [€/kWh]
R	Radius [m]
S	Section of the galleries [m]
S_{model}	Section of the galleries in the laboratory [m^2]
t	Filling time [m]
V	Volume of the system [m^3]
$V_{model,water}$	Volume of the water inside the model [m^3]

Partie V : Presentation and results of the the numerical model

Δx	Spatial step [m]
t	Time step [s]
$\Omega(h)$	Wet section [m^2]
A	Section [m^2]
a_1	Range-Kutta constant [−]
CFL	Courant-Friedrichs-Lewy coefficient [−]
Fr	Froude number [−]
g	Acceleration of the gravity [m/s^2]
$g(h)$	Newton Raphson derivative [m]
h	Water heigth [m]
$Head_{loss}$	Head loss [m]
i	Bottom slope [m/m]
J	Friction slope [m/m]
K	Manning friction coefficient [$m^{1/3}/s$]

$L(h)$ Length in the galleries [m]

n Manning coefficient [s/m$^{1/3}$]

Q Total flow rate [m^3]

q_l Lateral contribution [K][m^2/s]

R_h Wet perimeter [m]

S_0 Bottom slope [m/m]

S_f Friction slope [m/m]

u Speed of the water flow [m/s]

v_x Speed in x direction [m/s]

x_1 Newton-raphson guess [−]

h^* Dimensionless water depth [m]

$t^*_{emptying}$ Dimensionless time for emptying test[s]

$t^*_{filling}$ Dimensionless time for filling test[s]

v_{prop} Propagation speed [m]

Part I
Introduction

This master's thesis fits perfectly in the context of the current energy crisis. Indeed, the European Union aims for zero carbon emissions in 2050. This ecological transition will take place via the increase usage of renewable energies. This type of energy is however neither constant in time nor flexible. Wind turbines and solar panels, for example, only produce energy for certain weather conditions. These conditions cannot be controlled, so it is important to be able to counteract this intermittency of renewable energies. This challenge allows energy storages to be put forward. [Alvarado et al., 2015; EUROPÉEN, 2018] This thesis focuses on energy storage via hydroelectricity. The specificity is that the lower basin would be underground and composed of the old mines. Belgium and especially Wallonia is known for its mining activities between 1830 and 1980 [miniers majeurs de Wallonie, 2011].

One of the big disadvantages of hydroelectric power plants is their size. When a dam is built, valleys are flooded. This can severely disrupt the fauna and flora, and people are sometimes relocated to allow the valley to flood. In a dam, water is often released into the river. The notion of a lower basin is less clear for this type of plant [Erpicum and Dewals, 2022]. When a hydro power plant is composed as the one in Coo Trois-Pont. This power station consists of clearly delimited upper and lower basins. They are ponds that can be filled or emptied quite quickly [Belousov, 1974]. The dams themselves can sometimes be used as a place of recreation. There is therefore a certain reluctance of a part of the population to install hydroelectric power stations such as the Coo power station.

Another problem is the available head since the energy produced is directly proportional to it. A large head is therefore well appreciated. In a country like Belgium, this is not easy to find. There is not a lot of differences in altitude and locations for this type of power plant. Countries like Canada are very suitable for this type of power plant. Belgium, and especially Wallonia, is a country that has exploited coal mines a lot in the past. No more mines are exploited at the moment. Some mines can be visited but most have been left abandoned. These mines could be used as the lower basin of a pumped storage system to store energy. [Erpicum et al., 2017.b] Having a basin below the ground means less disturbance to the population and the fauna and flora. It may also allow for a greater drop than by using only the surface topology.

In order to be able to use a pumped storage system in Belgium, it is interesting to study the issue of old mines. A typical pumped storage system contains an upper reservoir and a lower reservoir. There is a difference of altitude between the two reservoir. This difference in level can be high as the lower reservoir is under the level of the ground. To create potential energy, a level difference is needed as well as a flow rate. A turbine transforms the potential energy into energy useful for humans. Then, a pump is used to bring the water back in the upper reservoir. The pump is used when the electricity price and the demand are low. The turbine is used when the electricity price is high and when the demand is high. [Erpicum and Dewals, 2022]

Using these old mines or underground reservoirs, it leads to the study of these reservoirs with unusual geometries since the mine galleries have complex geometries. The flow in these unusual reservoirs must then be studied. It is obvious that the flow in galleries or in a large reservoir is not the same. It is therefore important, in the context of the current energy crisis, to study the feasibility of such a project.

Part II
State of the art

Hydroelectric pump storage power plants are not a new technology. It has already been implemented in several countries: 25 GW in Japan, 22 GW in the USA, 15 GW in China and up to 40 GW in Europe (9 GW in Germany) [Alvarado et al., 2015]. Underground pump storage power plants are not implemented yet. The study of underground hydro power plants can be realised through laboratory studies, numerical models and analytical models. Various geometries can also be considered.

Several technical aspects of this technology have been studied such as the problems of air pressure and venting of the pipes [Erpicum et al., 2017; Kitsikoudis et al., 2020; Menendez et al., 2019; Menéndez et al., 2020b]. There are also geotechnical and geomechanical problems [Erpicum et al., 2017; Pujades et al., 2016]. The pump-turbine cycles and the pumps to be used have also been studied as there are flow and hydraulic issues [Pummer and Schüttrumpf, 2018]. From a socio-economical point of view, this technology would enable new economical activities. [Madlener and Specht, 2020; Menéndez et al., 2019; Pickard, 2011; Wessel et al., 2020]

The concept of underground pumped storage systems is not that new. In the USA, a golden age rised from 1970 to 1985. During this period, there were many new newspaper articles and technical reports on the subject. However, there is no concrete construction on underground pumped hydro storages. From 1986 to 2000, gas prices in the USA were quite favourable. There is an increase in gas power plants and the construction of pumped storage systems slows down. All pumped-storage systems are concerned, even the conventional ones. Since 2001, the challenge of intermittency of renewable energies is more and more present. Several permits are therefore issued and some concern underground pumped storage. [Pickard, 2011]

1 Specifics problems

1.1 Selection of the site

The use of old mines raises multiple challenges which makes such projects too uncertain. These challenges are related to the stability of the galleries and their geometry. In order to reuse tunnels, it is necessary to know their locations as well as their dimensions and conditions. The different mines in Wallonia are not all well referenced and it is not easy to know the exact location of the different existing galleries [Erpicum et al., 2017.b; Kitsikoudis et al., 2020]. Some of the tunnels can be exploited but not all of them. In addition, some underground mining facilities are developed as temporary infrastructures for material extraction processes. These infrastructures are not made to be used permanently. The extraction process makes it a dynamic environment where some tunnels are cut off from others. However, a skeleton of tunnels is still maintained to ensure transportation and communication. Some tunnels can therefore be reused even if it means an additional investment to determine the geotechnical conditions or to re-excavate parts that would collapse over time. [Alvarado et al., 2013]

1.2 Influence of air pressure on the waterflow

When the upper tank is filled with water, the lower tank is filled with air. During the turbining process, the water will push the air. The air has to be able to get out, otherwise it will create pressure and disturb the cycle. The ventilation shafts allow the air to escape. Their diameter is generally between 0.5 and 2m. [Menendez et al., 2019]

[Menendez et al., 2019] studied the influence of the air in the pumping-turbining cycle. Two scenarios were analysed, both using high and low flow rates. Scenario 1 is for the Turbine 1 and scenario 2 for Turbine 2. Both turbine are Francis turbine with an efficiency of 91.4 %. Turbine one has a flow rate of 32 m^3/s and a net power of 125 MW. Turbine two has a bigger flow rate than turbine one. The flow rate of turbine two is 55 m^3/s and a net power of 214 MW. In order to study the airflow, a numerical model was implemented. Different tank designs were analysed in order to compare the amount of energy that would be produced as well as the water flow. One of the scenarios contains a single air shaft of 1m diameter while the other contains one of only 0.5m in diameter. When the Francis turbine/pump is operating at full load with a flow rate of 32 m^3/s, the air pressure values do not influence the energy production. Using the same configuration but this time with a flow rate of 55 m^3/s, an increase in air pressure is observed. This increase leads to a significant decrease in energy production. For the second system (0.5m diameter air shaft), the energy production can be decreased by up to 12.5%. It should be noted that the design of an air shaft can be very costly. It is therefore necessary to find an optimisation between cost and energy production. The influence of the number of air shafts is also studied in this article. The influence of the air on the energy production is shown in Fig. 1a for Turbine 1 and in Fig. 1b for Turbine 2. For six air shafts, the energy produced corresponds to 100% of the energy stored. For Turbine 1 and one air shaft, the production corresponds to 98.5% of the stored energy. For Turbine 2 with one ventilation shaft, the production corresponds to 87.5% of the stored energy. For six ventilation shafts 96.4% of the stored energy is produced. The difference is much more significant. [Menendez et al., 2019]

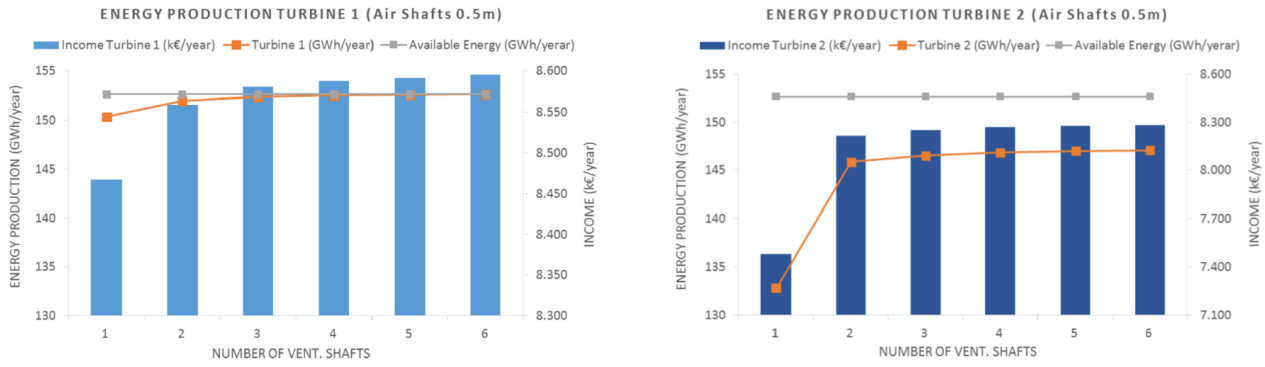

(a) Turbine 1 (b) Turbine 2

Fig. 1 Influence of the number of air shafts [Menendez et al., 2019]

[Menéndez et al., 2019] also studied the influence of the number of air shaft with a numerical model. Two model were considered. The two model are similar but one has six air shafts (Model A) and the other has only one air shaft (Model B). The model A has a slope of 2% while the B does not have one. The single air shaft has a bigger section than the ventilation shaft of the Model A. Model A has six air shaft with a diameter of 0.5 meter and Model B has an air shaft of 2 meters. The air pressures are higher in the model A than in the model B. The resistance of the model B for filling is lower. The pressures remain fairly stable over time for both models. However, the model B has lower costs as there is only one ventilation shaft. [Menéndez et al., 2019]

When the lower tank is not yet filled with water, it is filled with air at atmospheric pressure. When the water starts to fill the tank, it will compress the air. Thus, this interaction between air and water has to be managed. If the water pushes the air when it comes in, the air pressure will increase and it could alter the proper operations of the plant. For that reason ventilation

shafts connected to the parts of the mine at atmospheric pressure need to be provided. Another challenge will be to limit the number of air shafts, although they are essential. The effect of the air pressure can reduce the global efficiency of the underground pumped hydro storage plants. [Menendez et al., 2019; Menéndez et al., 2020a, 2020b]

1.3 Geomechanical aspect

Pump and turbine operations automatically lead to cyclic loading. These power stations fill their lower basin when energy prices are high and pump water up when they are low [Kitsikoudis et al., 2020]. Cyclic loading causes significant damages to the rocks. This progressively weakens them and causes them to fail at a lower load than the monotonic strength. For some materials, this loss can be less than 70% of the monotonic strength. [Erpicum et al., 2017]

When forming new cavities, the fatigue strength should be used instead of the monotonic strength. The loading of an underground pumped storage system is the hydrostatic pressure of the water. As water is in a porous and often permeable medium, it seeps into the rock. This leads to pore pressure [Erpicum et al., 2017]. This leads to oscillations in the groundwater level. When water is pumped, this can create a rapid gradient between the aquifer and the reservoir. This has an impact on the groundwater. These impacts on ground water flow obviously depends on the characteristics of the aquifer.

1.4 Hydraulic aspect

The lower reservoir where the flow is studied has an unconventional geometry. The geometry consists of a network of meshed galleries. The water arrives at only one point in the network before propagating throughout the entire network. The flow studied is a free-surface flow. The waves propagate through the galleries. Reflections appear at changes in direction. Depending on the angle and geometry, total, Mach or partial reflections are observed. [Alvarado et al., 2013; Alvarado et al., 2015; Pummer and Schüttrumpf, 2018]

In order to reuse old mines as the lower reservoir of a pumped storage system, a complete hydraulic study must be carried out. The upper reservoir is simply considered as a storage volume. The lower reservoir needs to be studied in more details. This study can be carried out numerically or by using a laboratory study. [Alvarado et al., 2013; Pummer and Schüttrumpf, 2018]

The study of [Pummer and Schüttrumpf, 2018] is based on the analysis of the different types of reflection, to know partial reflection, total reflection and Mach reflection. Partial reflection occurs when there is a change in pipe width. As this reflection is weaker than the other two, attention is not paid to it. The study of waves and especially their height is underestimated. This study is important because of the conversion of energy at the moment of reflection. The waves eventually lose their height and are damped. This damping is important for operational changes. These reflections are part of a hydrodynamic process that is important to take into account.

[Alvarado et al., 2013] has numerically studied the hydraulic flow in the lower reservoir that is composed of a gallery network with multiple levels. All galleries has a length around two kilometers and the slope are between 0.1-0.3 %. The filling and emptying processes have been studied. For the study, the roughness of the channel must be studied. This is estimated using Manning's formula. During all the simulations, the Froude number is kept above one. On average, this Froude number is equal to 0.5. A too high Froude number could cause damage to concrete or gallery materials. It is therefore important to keep it below 0.8. For the filling, the

velocities are 1 m/s and can reach up to 2.5 m/s. Since the emptying is carried out at lower flow rates, velocities are lower. The maximum speed observed during the emptying process is 1.5 m/s. During the emptying, the Froude number is kept below 0.6. The slope considered is 0.15 %. Hydraulic losses are also studied. These losses are important to consider because of the non-permeable flow conditions. These hydraulic losses can lead to energy losses in the system and therefore affect the energy produced. [Alvarado et al., 2013; Alvarado et al., 2015]

An other important aspect of the hydraulic part is the turbine and pump used in theses system. There are several types of turbine that can be used in hydroelectric power plants. The three main types of turbine used are the Pelton turbine, the Francis turbine and the Kaplan turbine. The Pelton turbines are used for large head and flow rate while the Francis and the Kaplan turbine are used for intermediate and low head respectively [Jacob, 1993; Pirotton, 2020]. The different ranges of applications for each turbine can be seen on Fig. 2.

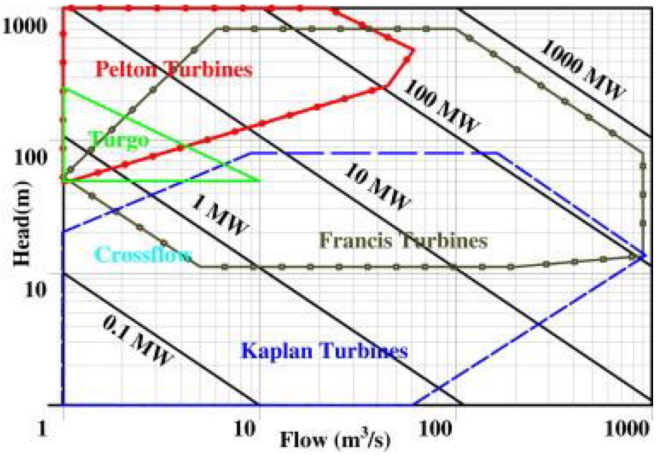

Fig. 2 Range of application for each type of turbines [Pirotton, 2020]

The Francis turbine is almost always positioned vertically. The water enters all around the wheel and the whole flow is under pressure. You also have to be very careful about cavitation in the turbine. [Erpicum and Dewals, 2022] A significant advantage of the Francis turbine is that it can operate both as a turbine and a pump. It is therefore not necessary to have two different machines [Pirotton, 2020]. The position of the pump/turbine is shown in Fig. 4. This is done to ensure sufficient pressure above the turbine and thus avoid cavitation as much as possible [Erpicum and Dewals, 2022].

The optimizing of the closing patterns of the gates is also important. This could reduce the number of water hammer. Minimising this phenomenon in a transient flow is very important to ensure the stability and safety of such an installation. Water hammer can cause damage in Francis pumps. [Menéndez et al., 2020b]

2 Laboratory study

When the flow is free surface, this leads to wave reflections in the connected galleries. This is due to the movement of water caused by differences in water levels. As this difference in level is necessary for a hydroelectric power plant, these reflections will be present. The laboratory setup can be either branched pipes or a single pipe. the two type of setup are tested and presented at Fig. 3. When branched pipes were tested, the angle between the pipes was 45°. The pipes were not closed at the top to allow aeration. This setup is represented at Fig. 3a. The pipe

alone was closed but ventilated. This setup is shown at Fig. 3b. In order to compare the two systems, their volume is identical. The length of the second gallery is therefore greater in order to maintain the same volume. [Pummer and Schüttrumpf, 2018]

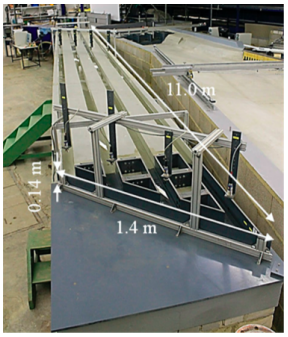

(a) Branched model

(b) Single-channel

Fig. 3 Laboratory setup [Pummer and Schüttrumpf, 2018]

Three types of reflection can be distinguished: partial reflection, mach reflection and total reflection. When there is a discontinuity in the width or height of the pipe, partial reflection is observed. Mach reflection is a special case. This is a reflection with an angle of incidence of less than 45° to the vertical wall. The wave does not leave the wall completely after impact with it. For total reflection, the wave leave completely the wall. Mach reflection shows a wave reflection on a vertical wall. The maximum height depends on the angle of incidence of the wave. If the angle is smaller than 20°, only Mach reflection occurs. When the angle is between 20 and 45°, Mach reflection occurs as well as classical reflection. [Pummer and Schüttrumpf, 2018]

The operating principles of these underground power plants can be exactly the same as those of a conventional hydroelectric power plant. However, the underground reservoir must be sized differently for reasons of surface stability. Old cavities where it is not possible to choose the geometry can be used. New galleries can also be dug. For economical reasons, the ratio of the volume of water and the volume of the reservoir should be as small as possible while keeping the surface flow free. When the wave reflection were analysed, it was found that the height of the waves were excessive. [Menéndez et al., 2020b; Pummer and Schüttrumpf, 2018]

3 Numerical study

3.1 Using existing mines

3.1.1 Martelange Mine

The exchange between the porous medium and the water in the lower reservoir is much greater in an underground pumped hydro storage than in a conventional hydroelectric plant. That is because the contact area is considerably increased. The exchanges are considerably influenced by the porosity and hydraulic conductivity of the aquifer, the characteristics of the lower reservoir, the relative elevations of the two reservoirs as well as the pumping and turbining cycles. [Kitsikoudis et al., 2020]

The Martelange mine in Belgium was studied by [Kitsikoudis et al., 2020] and [Morabito et al., 2020a]. This mine consists of nine large underground chambers with interconnected galleries. Each chamber is considered to be rectangular. They all have a length of 15m and a width of

45 m while the height varies. The first chamber is the lowest and reaches -150 m. The others are each 5 m higher than the next. All the chambers are fully ventilated. The surface level was considered to be horizontal at an elevation of 0m. All theses galleries together give a reservoir of 800 000 m^3. Close to the underground mine, river Sauer runs. This river can provide water to fill initially the reservoir. This river can also collect the exceeded of water in case of emergency. This kind of site can help to reduce the GHG emissions. For the Martelange mine, over two million tons of CO_2 equivalent can be avoided. That amount of CO_2 avoided correspond to 10% of the total emissions of CO_2 of Belgium in 2018. [Kitsikoudis et al., 2020; Morabito et al., 2020a]

The hydraulic model is done by modelling the flow in the upper reservoir and another model simulates the water movement in the lower reservoir. [Kitsikoudis et al., 2020]

However, there are still many doubts about the use of this technology. A suitable site is needed. Indeed, the rock must be of good quality, especially for deep reservoirs. Environmental consequences must also be considered. All the soil must be removed from the site when the reservoir is dug. The equipment is heavy and costly. [Pickard, 2011]

3.1.2 Coal Mine of Péronnes-lez-Binche

The Coal Mine of Péronnes-lez-Binche has been study by [Morabito et al., 2020a]. Two vertical walls reaching a depth of 500 meters were considered. There are crossed by three horizontal galleries at 200, 350 and 500 meters. The biggest challenge for this site is the available head in the system. The total volume of the three horizontal galleries is 15000 m^3 and provide quasi-steady state conditions for the pump (and the turbine). Two operational regimes are tested. The first one avoid high head variations by shutting-off the turbines' group and fully by-passing the water flow when the vertical wells are met. For the second regime, it operates continuously but it by-passes a turbine and splits the available head to the remainder of running machines.

3.1.3 Haniel Mine

The Ruhr region in Germany is an industrial region. There are more than 120 coal mines that have been or are being operated in this region. The Haniel mine consists of a network of tunnels distributed over seven levels. A one dimensional model was used to ensure good flow behaviour in the network. The flow rate was chosen while respecting two conditions: a Froude number lower than 0.8 and limiting the speed to avoid erosion of the concrete. The system can then be better controlled from a hydraulic point of view. The maximum speed allowed is 2.5m/s. A slope of 0.2% is also used to avoid supercritical flow conditions. Cavitation should also be avoided as much as possible. The filling process uses a flow rate of 40 m^3/s for 4 hours in turbine mode. [Alvarado et al., 2013; Alvarado et al., 2015]

3.1.4 Asturias (Spain)

In the last decades, coal mines have been exploited in the Asturias. Underground mines are generally 500-600 meters deep. The skeleton of these mines is usually composed of vertical pipes of 5 or 6 meters in diameter which were used for coal extraction. The network is obviously completed by horizontal pipes. Sometimes when mines are abandoned, they end up filling up with water. This water comes from groundwater and infiltration. [Menéndez et al., 2019]

The air in the tunnels when the water is in the upper tank will bring pressure when the lower tank is filled. This air pressure is a major issue in the choice of turbine flow rate. [Menéndez et al., 2019]

3.2 General geometry

In Wallonia, there are 5007 open sites, 361 underground mines for coal and metal and at least forty underground rock excavations. There are a lot of sites in Belgium but all of these cannot be exploited as a reservoir for a pump storage system. All old mines have their specific characteristics. The first criterion for the selection of a potential underground reservoir is the coherence of the host rock. The stability of the ground is very important. A second criterion is the geometrical typology of the residual voids of the extraction site as it is the key for efficiency. However, it is not possible to build an underground hydro power plant in all tunnel systems. The key factors are the geotechnical conditions and the type of network. [Alvarado et al., 2013; Erpicum et al., 2017.b; Erpicum et al., 2017]

For underground cavities that were exploited before the computer area, only paper-based archives are available. There is very small information for mines that closed before 1950. By only considering the mines that were active after 1960, the number of possible coal mines for this study is reduced from 154 to 39. [Erpicum et al., 2017.b; Erpicum et al., 2017]

In general, a mine is made of two vertical pipes with a circular cross section. The main galleries are with limited slopes and the cross-section is a circular arc. All this creates an interconnected network. Pipes in mines are usually 4 meters long. The depth is of 500 meters while the main gallery is usually 5 meters in diameter with a length of several hundred meters. [Erpicum et al., 2017.b]

The flow in the reservoir can affect the soil and the operation of the turbomachines. It is important to predict the movement flow in the reservoirs. That is why numerical models have been computed. Theses numerical model are process-oriented and distributed. They solve the mass and momentum conservation flow equations. The geometry depend on the site configuration. [Erpicum et al., 2017]

Numerical models can be of different kinds. A model can be in one, two or three dimensions. The conservation of mass and momentum equations are solved in the corresponding dimension. The flow is considered free surface and at atmospheric pressure. The simplest model is a one dimensional model. The equations solved are the same as those of the two-dimensional model. [Erpicum et al., 2017.b]

To carry out the various studies, a number of assumptions have to be made. Both tanks are at atmospheric pressure. When water fills the upper tank, the lower tank is filled with air. When the lower tank is to be filled with water, the water must push the air out. The air will be compressed and the pressure will increase. This pressure depends on the water flow rate and the cross-section of the air shaft. To keep the pressure atmospheric, the air must be able to escape. The presence of two fluids in an underground environment complicates the operation of underground hydro power plants. Indeed, there is an interaction between the air and the water. If the ventilation ducts are not properly designed, the air will create excess pressure. This will decrease the net load of the system, which means a reduction in energy production. This phenomenon differentiates an underground hydro power plant from a conventional hydro power plant. [Menendez et al., 2019; Menéndez et al., 2020b]

Stability problems can be observed as coal mines are operated as temporary infrastructure. They were not designed to last over time. Only the tunnels used for transport, coal extraction and communication are preserved. Some parts have been closed and are no longer in use. There may be rehabilitation work on accesses as well as re-excavation work on tunnels that may have

been destroyed. [Alvarado et al., 2013]

4 Conclusion

To conclude Tab. 1 lists the various articles used. The different articles are presented according to the problem they highlight. The first two columns represent the type of flow being studied. Either the flow is pressurised or it is free surface. In some cases, both types of flow can be considered. The next two columns represent the type of reservoir considered. The reservoirs are either known old mines or new cavities whose geometry can be chosen. As with flow, both cases can be studied in the same article. The last five columns represent the main problems addressed in the various articles. The first aspect is the geotechnical aspect. The second problem identified is the influence of air. The penultimate column presents the influence of pumping/disturbance cycles and their influence on the flow. The last column is not discussed in the context of this work because it concerns the economic part. However, the economic aspect remains a very important one, which is why it is mentioned in Tab. 1.

Articles	Pressurized flow	Free surface flow	Old mines	New cavities	Geotechnical aspect	Influence of the air	Influence of cycle/pump	Influence of hydraulic	Economic viability
[Pummer and Schüttrumpf, 2018]		■		■				■	
[Kitsikoudis et al., 2020]		■	■				■		
[Pickard, 2011]									■
[Pujades et al., 2016]		■	■		■				
[Morabito et al., 2020a]		■	■				■		■
[Wessel et al., 2020]									■
[Erpicum et al., 2017]		■	■		■	■			
[Erpicum et al., 2017.b]		■	■				■		
[Menéndez et al., 2020a]	■			■					■
[Menendez et al., 2019]	■			■		■	■		
[Menéndez et al., 2020b]	■			■			■	■	
[Alvarado et al., 2015]		■	■				■	■	
[Alvarado et al., 2013]		■	■				■	■	
[Menéndez et al., 2019]		■	■			■			

Tab. 1 Summary of the different articles

Looking at Tab. 1, it can be seen that many more studies have been carried out on known sites with fixed geometries than on new geometries. However, it is important to note that these geometries are not always perfectly known and that the states of the mines are not known. Most of the articles study free-surface flows while only a few articles study the geomechanical apsects. More articles study pumped-storage cycles to maximise energy production. Few of these articles really study the hydraulic aspect. The influence of air is also studied in a few articles.

Only one laboratory study has been carried out ([Pummer and Schüttrumpf, 2018]). All the others are numerical. There is therefore a lack of laboratory studies. For that reason, this

master's thesis will be based on a laboratory study coupled with a numerical model. First of all, a setup will be created to be as general as possible. The set up is not based on the geometry of an old mine. The setup will be created as if it were new tunnels. A series of laboratory tests will then be carried out. Once the phenomena have been identified and better understood in the laboratory, a one-dimensional numerical model will be produced. This model will be validated using the laboratory results and then will be applied to prototype geometries.

Part III
Methodology

In this section, a real size underground pumped storage hydropower plant will be designed to assess what could be achieved in practice. Then, the laboratory set-up will be designed and built based on the real size power plant while adding the constraints of a laboratory. The setup in the laboratory will be presented as well as all the instruments used. Then the method for the data acquisition and the data treatment will be presented.

1 Design of the setup

An underground pumped hydro storage is made of different parts that can be seen on Fig. 4. The upper reservoir can be at the level of the surface or underground. Because of the cavitation, the pump/turbine is located under the lower reservoir. The lower reservoir can be made of new cavities or can be made with old mines. Reservoirs do not necessarily have to be in the form of galleries. Several forms are possible, either new or the continuation of old abandoned underground structures. The lower reservoir can be made with one or two stages or even more. The geometry of this reservoir is free. The old mines can be used for some galleries and new galleries can be built. All this system will store energy to compensate the intermittency of the renewable energy and to balance the grid.

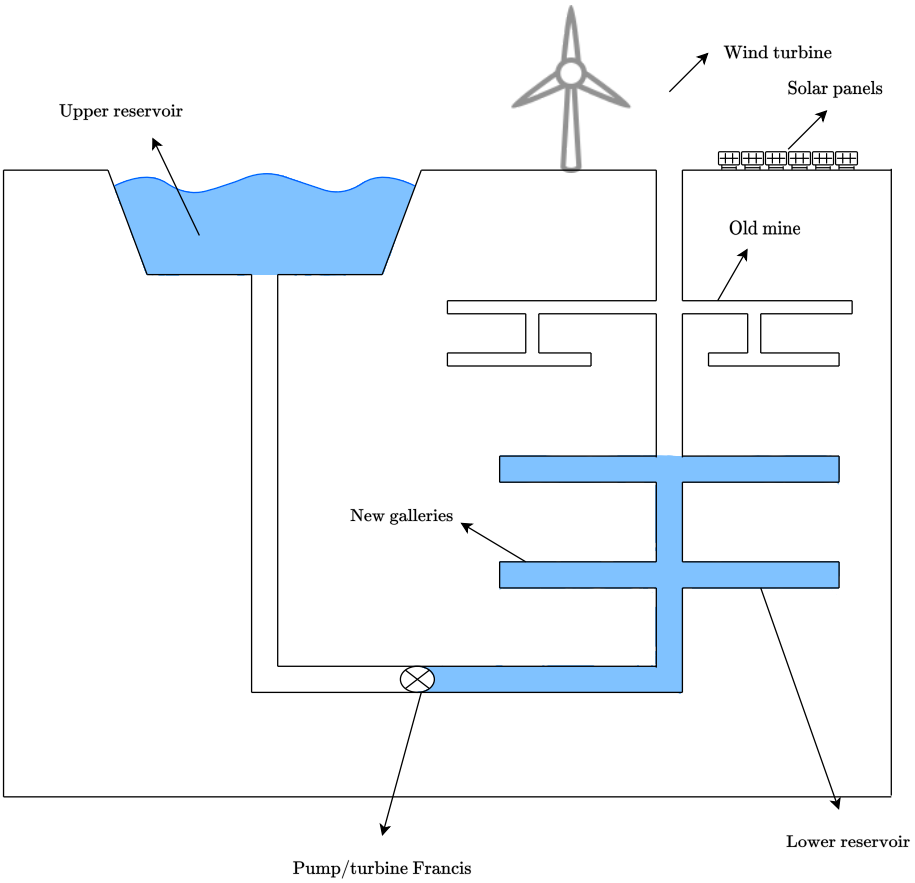

Fig. 4 Scheme of an Underground Hydroelectric Pump Storage

1.1 Real size setup

First the real size setup will be imagined and designed. In order to remain as general as possible, this setup is not based on a specific old mine. It will rather start with the construction of a new tunnel to be more generalist possible.

The flow remain a free surface flow and not a pressurised flow. Pressurized flow is too bad for the soil and stability. Flow under pressure would have a detrimental effect on the subsoil. Subjecting the pipes to pressure and vacuum cycles would affect the strength of the soil and reduce its fatigue resistance [Erpicum et al., 2017]. In the case of free surface flow, the lower part of the section must take the pressure of the water but the upper part is not subject to any pressure from the water. Thus, this type of flow allows for more favourable conditions. It is therefore important to ensure that the pipes do not become overloaded at any time during the filling process.

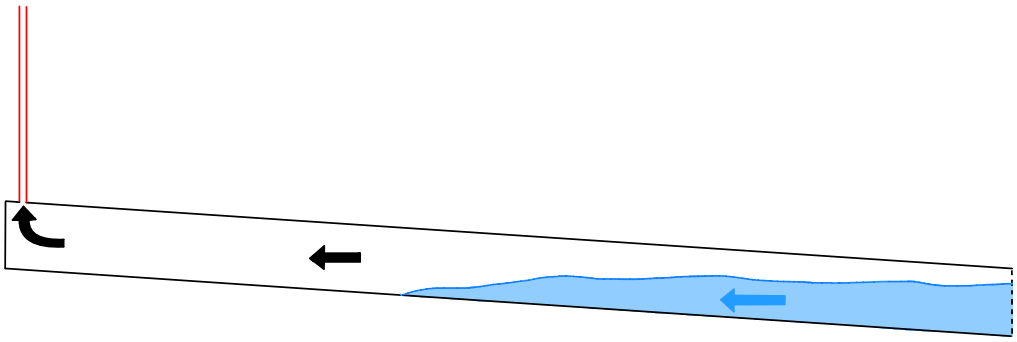

FIG. 5 Scheme of an air shaft

The air shaft is represented in red in the FIG. 5. It can also be seen on the picture that the water enter the gallery and push the air outside. The black arrow represents the path of the air to exit the duct. If the shaft is completely aerated, the air pressure will be atmospheric.

1.1.1 Sizing of the setup

The most suitable type of turbine for the application studied in this paper is the Francis turbine because of the large power required. Francis pumps/turbines can be single or multi-stage. Here it will be limited to single stage pumps. The height must therefore be limited. Indeed, if the head is too high, single stage Francis turbine pumps cannot be used.

To design the realistic set-up, it is first necessary to find the number of kilometers of gallery needed. For this purpose, it is interesting to look at the data of other hydroelectric storage plants in Europe as shown in TAB. 2. As far as hydroelectric storage plants in Belgium are concerned, only the one in Coo is very large plant while the others are all below 20 MW. As for the gas power plants in Belgium, their capacity ranges between 150 and 500 MW. Both gas and hydroelectric storage plants can easily be used for a flexible electricity production. It is therefore reasonable to aim for a capacity of 300MW for the realistic setup of this paper.

Storage	Power [MW]	Height [m]	Turbines	Volume [m^3]	Filling times [h]	Energy [MWh/day]
Coo	1164	275	6 Francis	8 450 000	5	5000
La Coche	320	927	1 Francis (5 stages)	2 100 000	14,5	/
Revin	800	250	4 Francis	9 000 000	3.45	2740
Montezic	910	423	4 Francis	30 000 000	40	38,800
Vianden	1096	283	10 Francis	6 840 000	4.20	4630
Reisseck II	430	595	2 Francis	/	/	/
Kops 2	450	800	3 Pelton	/	/	/
Tauernmoos	170	220	2 variable speed turbines	/	7.4	1260

Tab. 2 Data of different hydro power plant (both production and storage of energy) in Europe [Erpicum and Dewals, 2022; Freitag et al., 2011; Geth et al., 2015; Goekler and Meusburger, 2009; Herzog et al., 2022; Morabito et al., 2020b; Ortiz et al., 2022]

Only energy storage plants were presented. The last column represents the energy that can be stored per day in the various storage plants. The power shown is the maximum power. The filling time is calculated using the maximum power.

There are several assumptions to be made in order to determine the other parameters. Regarding the head, this is not limited by topography or site as the lower reservoir is underground. The head is chosen to be 500m as it is realistic with respect to what is technically feasible. It also corresponds to a reasonable depth for a Walloon mine as shown in Tab. 3. Moreover, it is a perfect match for a conventional single stage Francis pump/turbine.

Mines	Depth [m]
Blegny	236
Grand-Hornu	998
Bois-du-Luc	558
Bois du Cazier	1175

Tab. 3 Value of the different depths of the major mining sites in Wallonia [miniers majeurs de Wallonie, 2011]

The diameter of the tunnels must also be taken into account in the design. These will be excavated with a tunnel boring machine which generally have a diameter ranging from 1 to 17.6m. As most of them have a diameter of 10m, the diameter of the tunnels will also have that value. Such a diameter is optimal for good to medium rock mass conditions.

The efficiency of a conventional hydroelectric plant ranges from 90 to 95 %. For a storage plant, the efficiency vary from 70 to 80 % [Erpicum and Dewals, 2022; Menéndez et al., 2020a]. Most of them have an efficiency of roughly 75% [Schoenung et al., 1996]. It is therefore natural to use that value for the power plant studied in this paper.

Another important parameter to consider is the time required to empty the tank. As the tank used in the setup aims for daily regulation, a emptying time of 8 hours is chosen. It can be added that bigger reservoirs could be used for weekly or seasonal storage. To get an order of magnitude of the complete emptying time at maximal power, Tab. 2 should be read. It can noted that all the plants in this table are designed for storage only.

To summarise, the different parameters used in the design of the underground pumped hydro storage are listed in the Tab. 4.

Power	Height	Turbines	Efficiency	Gallery diameter	Filling time
300 MW	500 m	2 Francis	75%	10m	8h

Tab. 4 Data used for the calculation of the UHSP

It is therefore necessary to find the ideal volume of the tank satisfying these conditions. Once the volume found, the length of the galleries corresponding to the chosen section must be found. To find the volume the Eq. 1 is used.

$$P = Q \cdot \Delta H \cdot \rho \cdot g \cdot \eta \tag{1}$$

with

- P = 300 MW (power);
- Q = unknown (flow rate);
- ΔH = 500m (height);
- $\rho = 1000 kg/m^3$ (density of water);
- $g = 9,81 m/s^2$ (acceleration of gravity);
- $\eta = 0,75$ (efficiency).

The necessary flow can therefore be found through Eq. 1 as 81,55 m^3/s.

$$Q = \frac{P}{\Delta H \cdot \rho \cdot g \cdot \eta} = \frac{300 \cdot 10^6}{500 \cdot 1000 \cdot 9,81 \cdot 0,75} = 81,55 m^3/s \tag{2}$$

As both the head and the flow rate were computed in Eq. 2, Fig. 2 can be used to show that the design point is within the range of the Francis turbine. In the case of two turbines, each would only take 40.78 m^3/s. The assumption of taking two Francis turbines is therefore verified.

The volume required is computed by using the chosen flow rate and the filling time as shown in Eq. 3.

$$V = Q \cdot t = 81,55 \cdot 28800 = 2348623,86 m^3 \tag{3}$$

A volume of 2 348 623,86 m^3 is therefore required to be distributed in galleries of 10m diameter. As already mentioned, the flow must remain a free surface flow. Thus, section must not be completely filled as the flow would otherwise become loaded.

It has also already been explained that ventilation ducts should be installed. These should be placed at the highest point in the system and that is why a slight slope will be implemented. The lowest point is the injection point. Once the tank is completely filled, the section at the injection point could be almost filled. When the tank is completely full, the pipes must not be pressurized. When the water is at rest, it remains horizontal and must not put under pressure the top of the pipe. This situation is shown at Fig. 6.

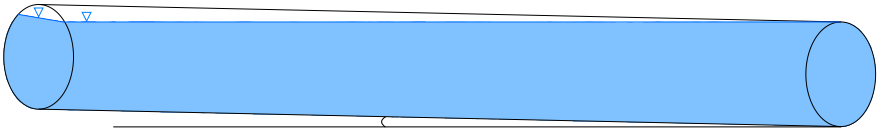

FIG. 6 Scheme of a duct filled with water

The volume of the galleries must therefore be calculated taking into account the geometry shown in FIG. 6.

The full cross-section of a gallery is given in EQ. 4.

$$S = \pi \cdot R^2 = \pi \cdot (\frac{D^2}{4}) = 78,18m^2 \tag{4}$$

As explained earlier, it is important to ensure that the pipes are not under pressure by filling the galleries as much as possible. In order to meet all these conditions, an optimisation was carried out. This optimisation allows to find the slope and length of gallery that minimises volume. This is done in order to find a gallery length that would respect the conditions explained above.

Once the number of kilometers and the slope are found, the geometry also needs to be determined. Ideally, the galleries should be arranged in a rectangle and not in a square to limit one dimension. This would avoid to take up an inordinate amount of space and make the setup longer and thus narrower. The setup will be symmetrical to facilitate the distribution of water in the galleries. The slope that is found is 0.023 %.

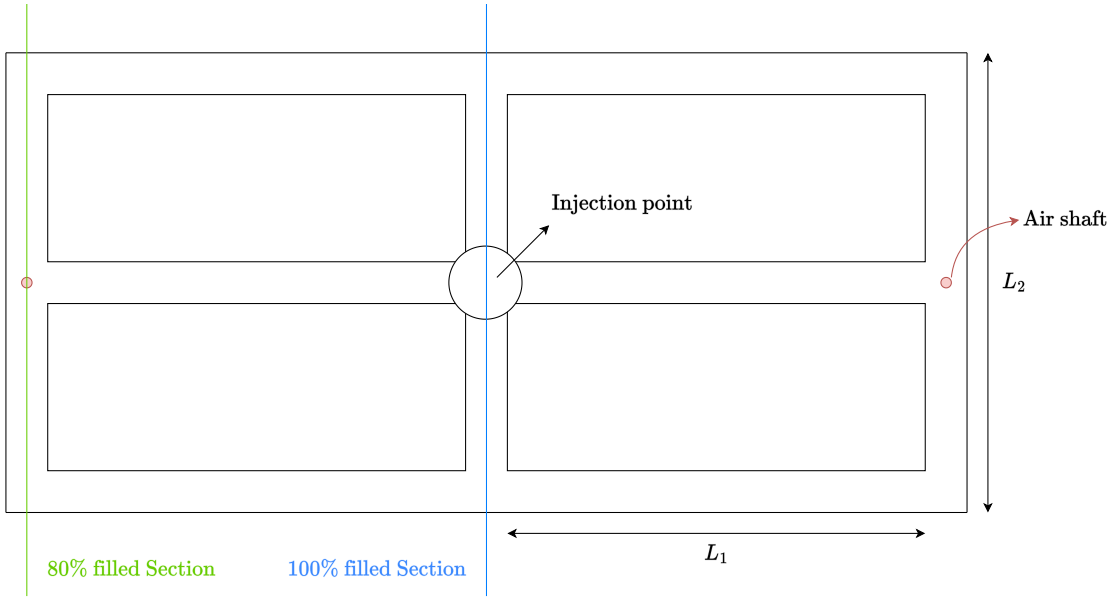

FIG. 7 Scheme of a duct filled with water

The actual setup is shown in the FIG. 7. The pipes of length L_2 remain horizontal. The small slope concerns the pipes of length L_1. The two pipes of length L_2 on the edges are thus filled up to 80 %. Ventilation shafts must also be positioned at the highest point. By distributing the required volume of water through these pipes, the following different lengths are obtained.The total number of kilometers of galleries is therefore 31.92km. If the full section

had been considered, this number could have been reduced to 29.9km.

$$\left.\begin{array}{l} L_1 = 4570m \\ L_2 = 1500m \end{array}\right\} L_{tot} = 31920m = 31,92km \tag{5}$$

1.2 Laboratory sized setup

1.2.1 Scaling of the laboratory sized set up

Now that the real plant has been designed, it must be adapted to the laboratory. In the laboratory, 10cm diameter tubes are available. The tubes have a diameter of 10cm, so the scale used is 1:100 to match the 10m diameter in the full size model. Smaller diameter are not considered because it would not allow to see correctly how the water propagates. However, if this scale 1:100 is applied, there would be galleries of 45m by 15m. It is obviously not feasible given the limited space available in the laboratory. A solution must therefore be found to reduce the length of the pipes. Since longitudinal pipes are large pipes with a one dimensional free surface flow, modelling it in the laboratory is not the most important. By doing this, the model can be reduced in size so that it can be made in the laboratory. To select the parts that will be kept or not, it is assumed that after a length of ten times the diameter, the flow is a simple one dimensional flow. The model must be modified to include only the parts of interest which are the injection point and the links between the galleries. Indeed, at the injection point, it is necessary to look at how the water will be distributed in the different galleries as well as the influence of the number of galleries where the water can move. The final dimension of the laboratory setup is shown at Fig. 8.

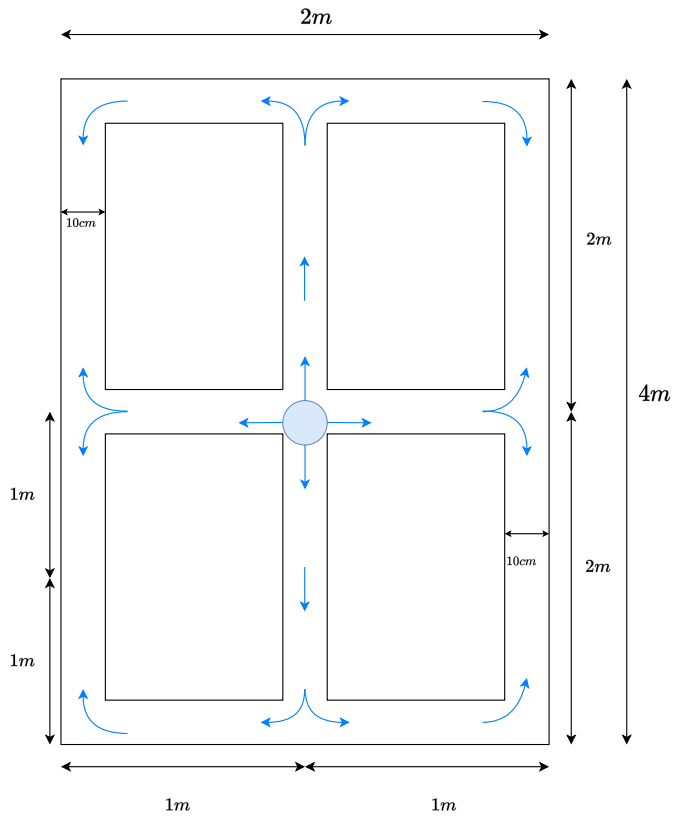

Fig. 8 Scheme of the setup in the laboratory

When the water changes direction, there is one meter to allow the water to reach a one dimensional flow. The slope must be represented to scale. To represent the slope of 0.023 %, the outer pipes must be raised by 0.46mm which is not realistic. Therefore, there will be no slope in the laboratory.

As far as air shafts are concerned, they will not be represented in the laboratory. The sensors for the water depth measurements will be placed above the pipes. In order to measure the water level in the pipes correctly, holes will have to be made in the pipes. These holes will allow perfect ventilation of the pipes.

As the geometric scaling has been carried out, the necessary flow rate in the laboratory must now be estimated. Since the flow is free surface, a Froude similarity is used. In a Froude similarity, the Froude number of the real size setup and the one of the laboratory setup are the same. This similarity is used for free surface flow. The Renolds similarity is used for prezzuried flow. The flow rate calculated with the Froude similarity can be found at Eq. 6.

$$Q_{labo} = \frac{Q}{100^{2.5}} = \frac{81,55}{100^{2.5}} = 8.155 \cdot 10^{-4} m^3/s = 0,8155 l/s \tag{6}$$

It is then possible to calculate the total volume of water required since the total section of the pipe is known and there are filled at 88 % of their total capacity.

$$S_{model} = \pi \cdot 0,05^2 = 0,0079\ m^2 \quad \rightarrow \quad S_{water} = 0,0069\ m^2 \tag{7}$$

The total length of the setup is :

$$L_{tot} = 4 \cdot 3 + 1 \cdot 6 = 18\ \text{m} \tag{8}$$

It is therefore possible to know the total volume of water needed in the laboratory setup.

$$V_{model,water} = S_{model,water} \cdot L_{tot} = 0.1251\ \text{m}^3 = 125,11\ l \tag{9}$$

Considerations should also be given to the geometry of the injection point as it is a critical point in the setup.

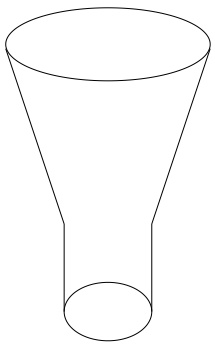

Fig. 9 funnel-shaped geometry

A funnel-shaped geometry like exposed in Fig. 9 could be considered. Such a shape allows a larger section at the entrance. It is interesting in order to not pressurized the section. However, it is quite complex to put this into practice in reality and in the laboratory. If this setup were to be built, it would be done with tunnel boring machines. The cross-section of these is constant, so it is not possible to build such a shape. This injection point represents the pool that would actually be used in the project.

Therefore, in order to facilitate the construction of the setup in the laboratory and match as closely as possible what will be possible in reality, a constant cross-section will be considered. Using a section with a ten centimeters diameter (similar to the diameter of the galleries) for the injection zone is not practicable. This would make problems in terms of pressure on the injection zone. The aim is to avoid pressure at the top of the injection zone, so a fairly large section is

required. The cross-section of the injection zone will therefore be larger than the cross-section of the galleries. The diameter of the injection area is 40cm.

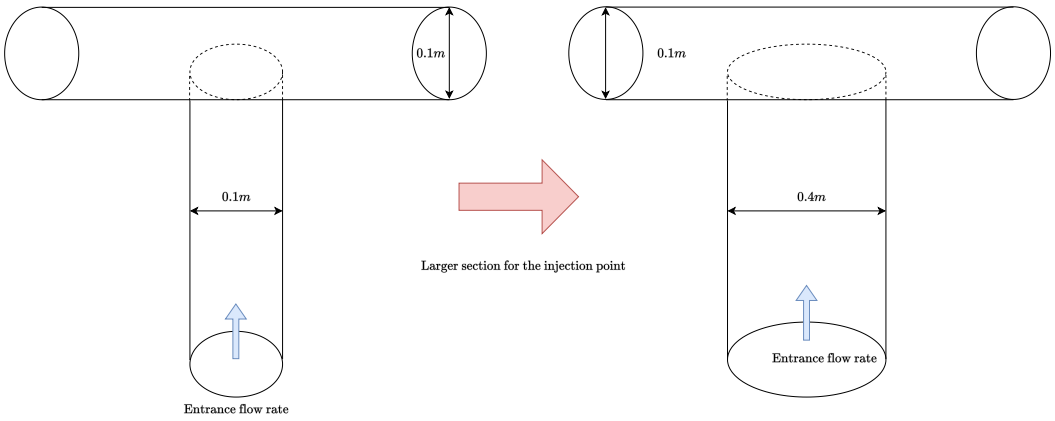

FIG. 10 Geometry of the injection point

The geometry of the injection point can be a point of study as its diameters can be a parameter influencing the pressurizing of the central point. The diameter of the injection zone is four times higher than the diameter of the pipes. The height of the injection point will be sixty centimeters and the water will be injected from below. Doing so allows the flow to be stabilised before it enters the galleries. It also eliminates any backflow that may be present when the pump is started.

1.2.2 Laboratory

FIG. 11 shows the setup in the hydraulic laboratory of the University of Liege.

FIG. 11 Setup in the laboratory

A tank contains the water upstream that will be sent into the system. The tank is connected to the setup by a circular pipe that goes through a pump and a flow meter. The pump is used to inject the water into the system while the flow meter allows to measured the flow rate injected

in the system. Fig. 12 shows the pump used in the laboratory. Fig. 13 show the tank for the injection point.

Fig. 12 Pump

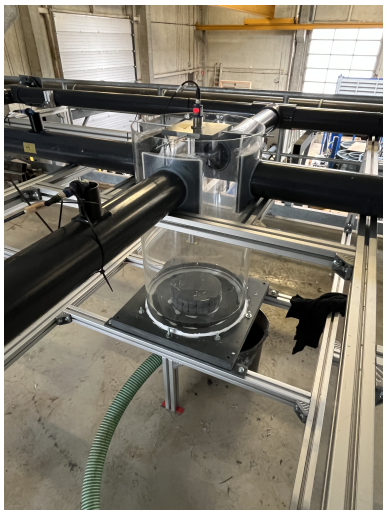

Fig. 13 Injection zone with an anti-removal device

As can be seen in the Fig. 13, there is a cylindrical piece with holes in the centre. This part allows a better distribution of water in the injection area. Without this part, at high flow rates, there would be a lot of waves inside. These waves do not allow to measure the data correctly. With this device the water rises uniformly in the injection zone without creating waves.

2 Instrumentation

In order to measure the water depth in the galleries, sensors must be used. These sensors must be able to measure the water depth in a closed circular channel. These are ultrasonic sensors that work according to the Doppler effect. The selection of the sensors was based on their function as well as on the measuring range. The heights to be measured must never be in the dead zone of the sensor.

To carry out the measurements, a hole is made in the pipe and the sensor is positioned above it. The sensors must be able to measure both small and large heights of water in the pipe. It can be noted that the holes in the pipes should be as small as possible so as not to reduce the height of the pipe too much.

2.1 Description of the sensors

The sensors chosen are pico+35/WK/I sensors. These sensors were chosen because they allow to measure correctly the water depth in the pipe. The pipes have a diameter of ten centimeters and the holes that allow the sensors to take measurements have a diameter of three centimeters. Since the pico+35/WK/I sensors have a dead zone of 65 millimeters [Microsonic, accessed in February 2023-a], they are positioned 60 millimeters from the top of the pipe. The Tab. 5 summarize the characteristics of the sensor pico+35/WK/I.

Characteristic	pico+35/WK/I
Measuring range	65 - 600mm
Special characteristic	90° head
Measuring procedure	Echo propagation time
Transducer frequency	400 Hz
Blind zone	65 mm
Service scope	350 mm
Ultimate scope	600 mm
Resolution	0,069 to 0,17 mm
Precision	± 1 %

Tab. 5 Characteristic of the sensor pico+35/WK/I [Microsonic, accessed in February 2023-a]

The resolution is a function of the analogue window. The precision of the sensors is due to a compensation of the internal temperature. By reducing the measurement window, this allows for greater accuracy and a more stable signal. Since the measurement will only be made in the pipes, the largest measurement will be the bottom of the pipes. There is therefore no need to have a measurement window larger than 200 millimeters.

With the *LinkControl* software it is possible to apply filters to the sensors to facilitate measurement. Three filters can be applied to the data :

- **F00** : The data is the first to be perceived by the sensor. It is therefore necessary to process the data after it has been collected.
- **F01** : The selected value is the smallest value that is recorded by the sensor.
- **F02** : The value used is the average of the values measured by the sensor.

For filters F01 and F02 a filter strength index varying from 0 to 9 is applied. It can be noted that the higher the index, the stronger the filter, the lower the index, the weaker the filter [Microsonic, accessed in February 2023-c]. For pico+35/WK/I sensors, the filter applied is F02 with the strength P03. The data will be processed afterwards to avoid outliers and keep only consistent data. This is because when measuring in a circular pipe, it is not easy to measure the bottom of the pipe. The F01 filter is therefore not suitable for this situation.

A vnc-35/IU/TC sensor is used to measure the water level in the injection zone. This sensor is used because only six pico+35/WK/I sensors are available in the laboratory. Its characteristics are summarized in Tab. 6.

Characteristic	vnp-35/IU/TC
Measuring range	65 - 600mm
Measuring procedure	Echo propagation time
Transducer frequency	400 Hz
Blind zone	65 mm
Service scope	350 mm
Ultimate scope	600 mm
Resolution	0,025 to 0,17 mm
Precision	± 1 %

Tab. 6 Characteristic of the sensor vnp-35/IU/TC [Microsonic, accessed in February 2023-b]

The measurement range is similar to that of the pico+35/WK/I sensors. The dead zone is also the same. The only main difference is the orientation of the sensor head, which is 90° in the case of pico+35/WK/I sensors. For the vnp-35/IU/TC the head is straight, but this makes no difference to the way measurements are acquired.

2.2 Position of the sensors

On Fig. 14 the position of the different sensors can be seen. It can be noted that it is not interesting to position the sensors too close to bends and intersections because wave reflections occur at these points. When there is reflection and water movement, it is complicated to know exactly what the catapult is measuring. If the measurements are not reliable, it is not possible to analyse them correctly. By placing the sensors away from intersections and bends, it will be easier to see the propagation of the waves. The sensors are placed at mid-pipe in the shorter pipes. For the two longest pipes, the sensors are placed at 1/3 and 2/3 of the pipe.

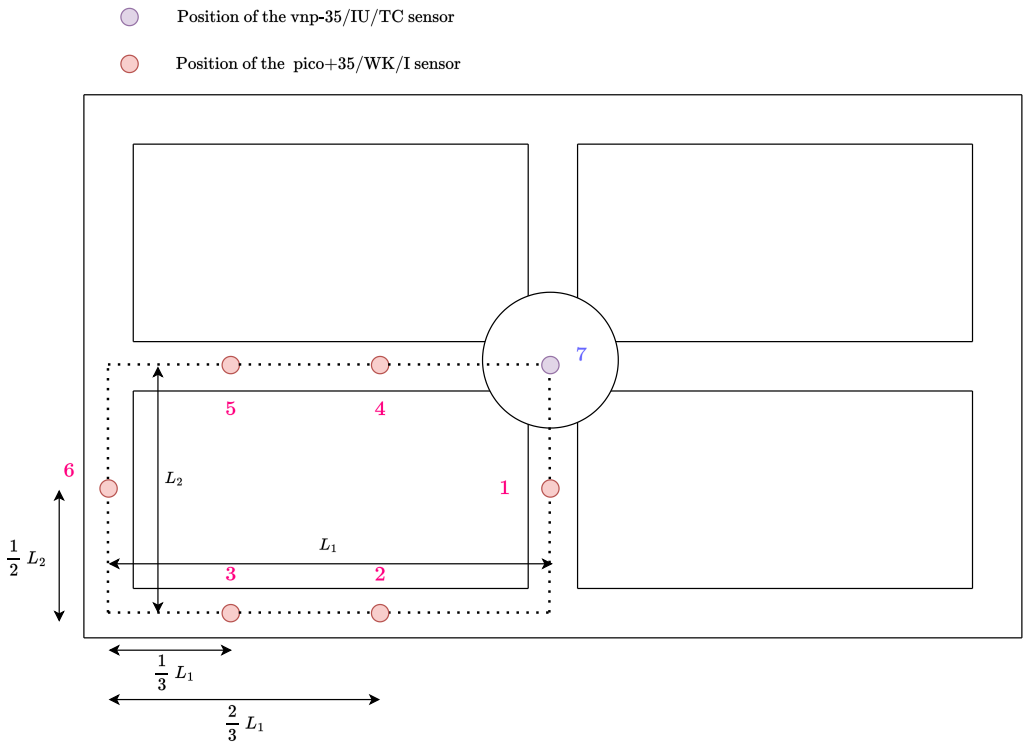

Fig. 14 Localisation of the sensors

The number position on Fig. 14 represent the sensor number that will be useful when presenting and analysing the results. The sensors are only placed on one quarter of the model since the water will be distributed symmetrically in the four parts of the setup. It is therefore not necessary to have sensors everywhere on the model.

Fig. 15 shows the support used to place the sensors above the pipes. A sensor pico+35/WK/I can also be observed.

FIG. 15 Support that hold the pico+35/WK/I sensor above the pipe

These supports are made of plastic and produced using a 3D printer at the University of Liege. They are fixed on the the pipe with silicone. A four centimeters diameter hole is therefore made in the pipe. The size of the hole must allow the sensor to measure the bottom of the pipes.The sensors send a signal that takes the form of a cone. It reflects off the first material it finds, whether it is water or PVC pipes. It is therefore necessary to ensure that the signal cone passes entirely through the pipe. If the hole is too small, the signal will be reflected on the edges of the pipe. It will not measure correctly inside the pipe. A four centimeters diameter hole allows to correctly measure the bottom of the pipes and to keep a stable signal over time.

2.3 Meter flow

To measured the water flow in the system, a flowmeter is used. FIG. 16 show the flowmeter that is used.

FIG. 16 Flowmeter used in the laboratory

The flow operates on the basis of Faraday's law. The flow is perpendicular to a magnetic field. When a conductor is moved at a certain speed perpendicular to lines of magnetic flux of a certain intensity, a voltage U_i is induced at the ends of the conductor. The voltage U_i is proportional to the speed of the flow. Tab. 7 show some of the useful properties of the flowmeter. [Siemens, accessed in February 2023]

Characteristics	Flowmeter
Measured range	0 to 10 m/s
Precision	0.2% ± 1 mm/s
Method	Faraday's law

Tab. 7 Characteristics of the flowmeter [Siemens, accessed in February 2023]

The measurement range can be reduced in the same way as for the sensors presented above. The measurement range will therefore be reduced to a smaller range to guarantee greater accuracy. The maximum flow rate that would be tested is 3 l/s. The range become therefore 0 to 3 l/s.

The flow meter, like the sensors, returns a voltage over time. It is therefore also necessary to perform a calibration in order to know the injected flow rate. Unlike sensors that measure water depth, the flowmeter has an integration constant. This means that the data is averaged every tenth of a second. The flow meter data will therefore be taken at a frequency of 10 Hertz. Taking measurements at a higher frequency would not provide any additional information because of the integration constant. It is therefore not useful to have an acquisition frequency of more than 10 Hertz.

3 Data acquisition and treatment

3.1 Data acquisition procedure

To launch a test, it is necessary to determine the discharge rate through the opening of the valve. Once the pump is switched on and the valve is open, the recording of the probes is started. The sensors record at a frequency of 100 Hertz, meaning that there are 100 data recorded per second. The data from the flowmeter are also recorded but at a frequency of 10 Hertz and not 100 Hertz as explained before. The flowmeter only measures in one direction. Once all the filling tests have been completed, it is inverted so that the emptying tests can be carried out.

The sensors return a voltage over time. The data are passed to an acquisition device and retrieved via the *LabView* software. They are acquired at a frequency of 100 Hz. After the acquisition of the data, the voltage must be transform into distance and after into water depth. It is possible to know the distance between the sensor and the water level in the pipe via a calibration. The relationship between voltage and distance is linear. Three known points are measured via the sensors. The three voltage corresponding to the three height will be know. With these three point, a calibration line can be implemented for each sensor. This calibration allows to know the distance between the water height and the sensor. The same method is applied with the flowmeter but with three different flow rates.

The position of all the sensors is known. It is therefore possible to find the water level in the pipe. As the pipes are not perfectly straight, when multiple sensor are show on a same graph, data are given in altitude. This ensure to see the same initial condition for all sensors. In order to know the altitude of the pipes, a perfectly horizontal laser plane is drawn. The plane

is horizontal due to the pendulum in the laser. Then the distance between this laser plane and the pipes is measured. The altitude of the pipes can thus be known.

3.2 Tests procedure

Two different test campaigns were carried out. First, filling tests and then emptying tests. The tests are all carried out in the same way. First, a valve opening is selected. The valve opening is used to determine the flow rate. The first step is to switch on the pump. Then the valve is opened. When the test starts, recording begins via *LabView*. When the water reaches the top of the pipes, the recording is stopped. The pump is then switched off. The valve remains in the same position for emptying. This allows the test to be repeated with exactly the same opening as the previous test. It is therefore possible to carry out several repetitions and compare them with each other.

For the emptying tests, the procedure is fairly similar. First the valve opening is chosen and will determine the outflow. Then the pump is switched on to fill the tank almost completely. Once the water reaches the pipes, the pump is stopped. This is when the recording begins. When the water reaches the bottom of the tank, recording is stopped. As with the filling tests, the valve is kept open so that tests can be carried out under the same conditions.

3.3 Data treatments

Once the signal is received, it must be processed before being analyzed since it is raw and contains outliers. Outliers are points that are isolated and far from the curve. These points should not be considered in the curve. Secondly, it is possible that there are some disturbance in the probe that needs to be removed before analysis.

The first processing to be done on the data is the removal of outliers. The method used for that is the moving average method. This method scans all the points received and averages them over a window centred around the point. The size of the window is obviously to be determined. It should not be too large in order to avoid smoothing the data and it should not be too small in order to remove the outliers. This method assumes that the distribution of points follows a normal distribution. On this point window, the mean and standard deviation are computed. If a point in this window is more than two times the standard deviation away from the mean, it is removed from the sample. According to the normal law, this means that 95.45 % of the points are retained. This step allow to remove most outliers in the signal.

The data are recorded at a frequency of 100 Hz, so the windows used should not be too large to smooth out the curve too much. Only the outliers should be eliminated. The aim of this first processing is only to obtain the signal without the noise of the probe. The chosen window size is 100. Fig. 17a shows the difference between the different window choices. The Fig. 17b shows a zoom that makes it easier to see the influence of the window size.

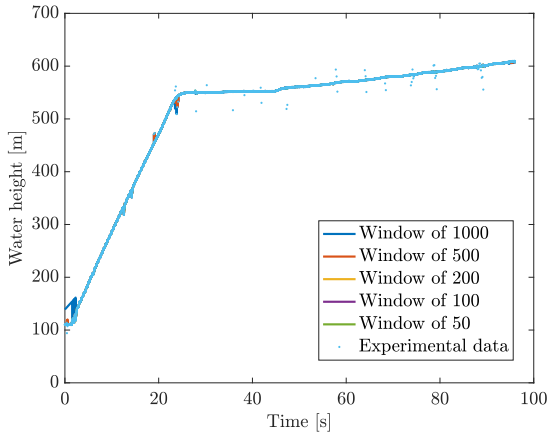

(a) Influence of the moving average window size on signal processing

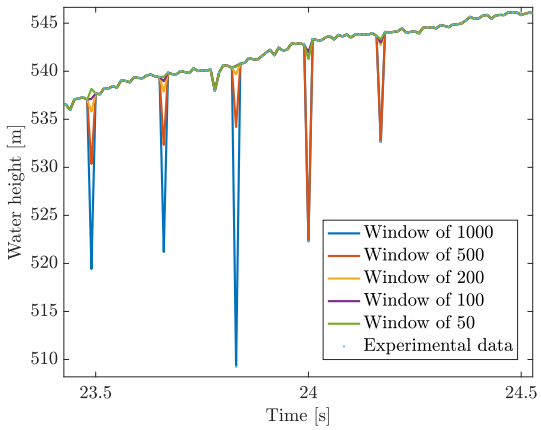

(b) Zoom on the change in slope to show the influence of the window size

FIG. 17 Influence of the window size

On the one hand, the larger windows, such as 1000 and 500, smooth out the curve too much when there are changes in direction. On the other hand, the smallest window tested, 50 points, removes almost no outliers as there are not enough points to spot the outliers. In order to remain as faithful as possible to the raw data but still remove outliers, a window of 100 points was chosen. The data cleaning can be seen in the FIG. 18. It can be seen that the data is recovered without the outliers. It can however be noted that the signal remains imperfect and is not completely smoothed.

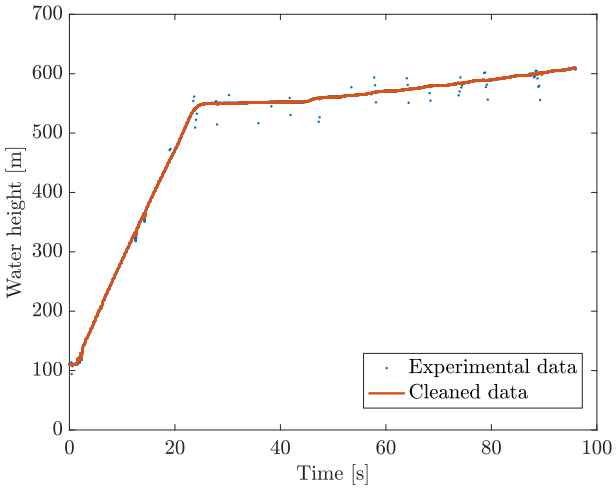

FIG. 18 Cleaned data and experimental raw data for the sensor above the tank

When a test is performed in the laboratory, it is performed several times in order to ensure that the data are correct. Indeed, there is noise in some signals that must be removed by comparing tests performed under the same conditions. This lead to the second data processing.

Despite the first processing of the data, some peaks are still present. These peaks are composed of several points and are therefore not considered as outliers. This is disturbance from the sensor. The measurement in circular pipe is not easy and the sensors can be very sensitive. In order to eliminate these peaks, the three tests are compared with each other. The entire curve

is covered. When points move away from a certain upper or lower limit, they are no longer considered. This second treatment can be seen on the Fig. 19.

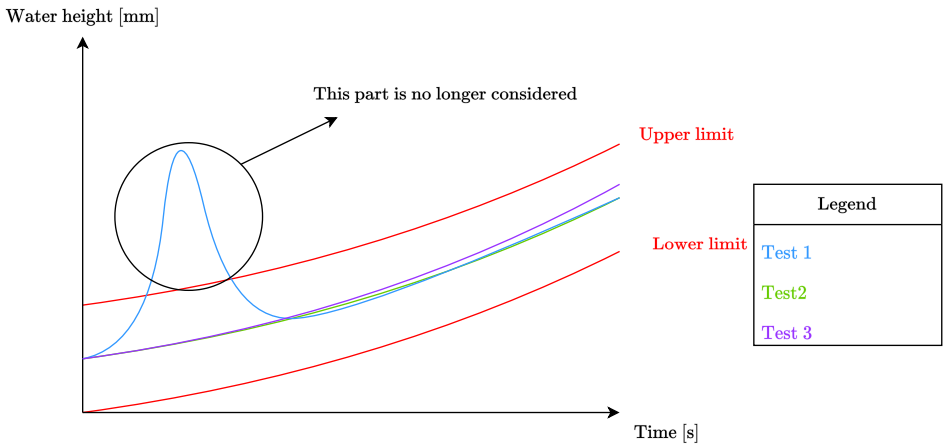

Fig. 19 Second treatment of the data

The distance between the upper and lower terminal is 2 mm. This removes most of the peaks present. By not considering these peaks when averaging the curves, the curves to be analysed are much smoother. Once this treatment has been completed, the average of the three tests is evaluated. It is this average curve that will be analysed in the following. The previous treatments have eliminated all the outliers and unwanted peaks. The results of the third treatment are presented at Fig. 20.

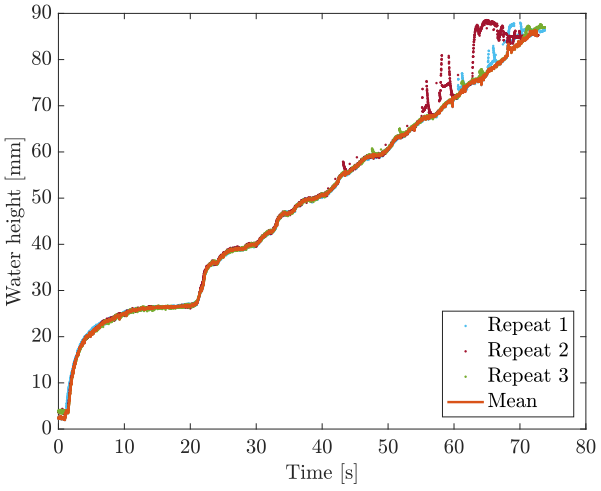

Fig. 20 Third treatment of the data

It can seen that the orange curve does not have all the oscillation of the reds dots at the end of the curve. All the pics of the the three tests are not considered in the orange curve. Thats is this curve that would be analysed.

Part IV
Experimental results

Only the experimental results will be presented in this section. For ease of use, each probe has a number and therefore corresponds to a position in the setup. The numbering of the sensors according to their position in the setup is shown on Fig. 14. The different hydrographs used and the configurations will be presented. Two types of tests were carried out. First, tests were carried out on the filling of the pipes. Theses tests correspond to the production of energy in reality. Secondly, tests on the emptying of the pipes were carried out. To present the results, the uncertainties of the different tests will be presented. Then, the results of the pipe filling tests will be described. Finally, the results of the draining tests will be described.

For all the simulation discussed in this section, the initial water head is calculated from the bottom of the pipes as shown in Fig. 21. For the filling of the pipes, time starts when the water in the tank reaches the level of the pipes. Time therefore starts when the water reaches the red line on Fig. 21. For the emptying of the pipes, the time starts when the emptying begins. The emptying of the tank will be considered with negative y values.

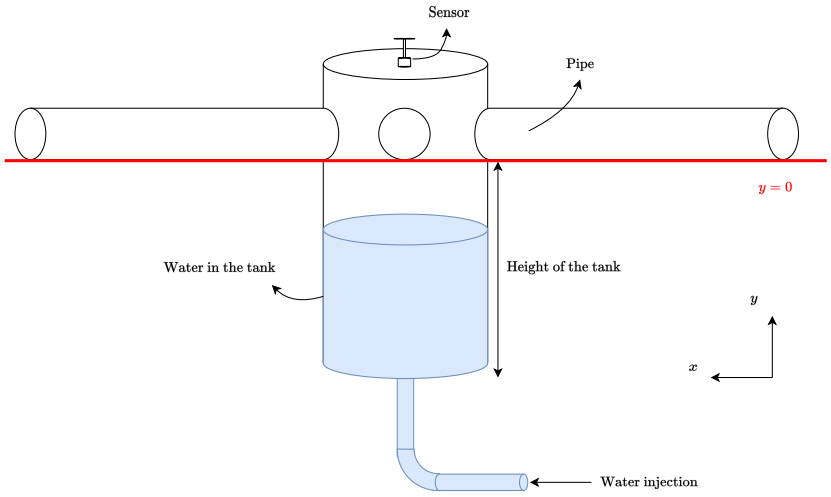

Fig. 21 Scheme of the location of the y_0

For the filling tests, the tank is always empty at the start while the pipes are not always completely empty. This is because the pipes are horizontal in the laboratory and it takes time for the water to empty. The initial conditions for each flow and test will be presented in due course.

Accordingly, the starting time is when the water enters the pipe. The study therefore focuses on the filling of the pipes and not on the filling of the tank. For the emptying test, the emptying of the tank will be part of the study. Tab. 8 shows the different configurations, and the number of repetitions. The theoretical time required to completely fill the tank in each configuration is also shown. For emptying, this is the theoretical total emptying time for the pipes. These times are calculated on the basis of the average flow rate for each test and the total volume of the tank.

Configuration	Average discharges	Number of repeat	Time
Filling of the pipes			
1	0,5 l/s	3	281.33 s
2	1,3 l/s	3	114.75 s
3	1,9 l/s	3	82.35 s
4	2,6 l/s	3	62.02 s
Emptying of the pipes			
1	0,34 l/s	3	611.28 s
2	0,64 l/s	3	321.05 s
3	0,74 l/s	3	279.33 s
4	0,97 l/s	3	217.93 s

TAB. 8 Configurations, mean discharges, number of repetitions and total filling/emptying time

Four discharges were tested for the filling and emptying. Each of these discharges was repeated three times. Thanks to these three repetitions, the uncertainty on the analysed data can be quantified. Two of the four proposed discharges for the filling are shown in FIG. 22a and FIG. 22b. They show the first and the last configuration of TAB. 8. The flow rate presented in TAB. 8 represented the average water flow rate during a test.

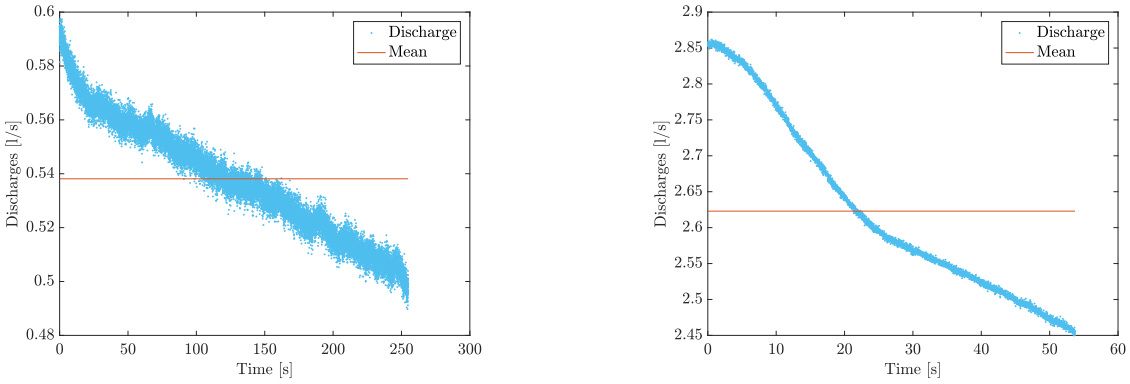

(a) Lowest discharge for the filling

(b) Highest discharge for the filling

FIG. 22 Discharges of configuration one and four for the filling

It can therefore be seen that discharges are not constant over time. On FIG. 22a, the variation of the discharges is 0.1 l/s. For the highest discharge the difference is 0.4 l/s. This phenomenon is due to the pump not delivering a perfectly constant flow rate and to the downstream load, which is constantly increasing.

FIG. 23 represent the flow rate when the pipes are emptying. These hydrographs are therefore conditioned by gravity flow. There are no pump to empty the reservoir and therefore the flow is solely based on gravity. The largest average flow rate is given by the maximum valve opening and it is shown at FIG. 23b. The minimum flow is achieved by closing the valve almost completely. This hydrograph is shown at FIG. 23a?

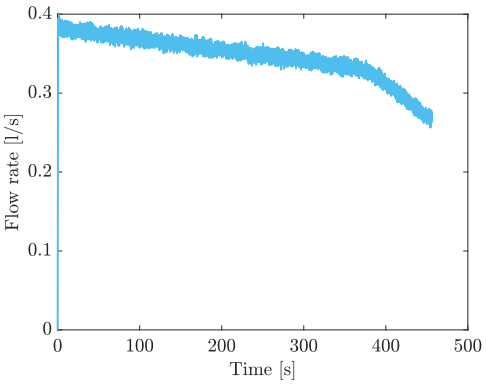

(a) Lowest discharge for the emptying

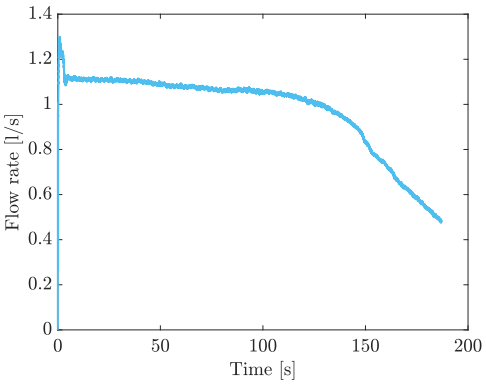

(b) Highest discharge for the emptying

FIG. 23 Discharge of configuration one and four for the emptying

The discharge flow rate and the filling flow rate are not constant over time. The upstream load decreases while the downstream load increases. Two trends are also observed. After a certain time, the slope of the flow rate increases. The first part corresponds to the emptying of the pipes. The second part of the curve corresponds to the emptying of the reservoir.

1 Uncertainty in experimental data

By looking at the difference between the three repetitions of each configuration, the uncertainty in the data can be quantified. FIG. 24 shows the three replicates of the third configuration at sensor 4. FIG. 24a shows the filling of the pipes while FIG. 24b shows the emptying of the system.

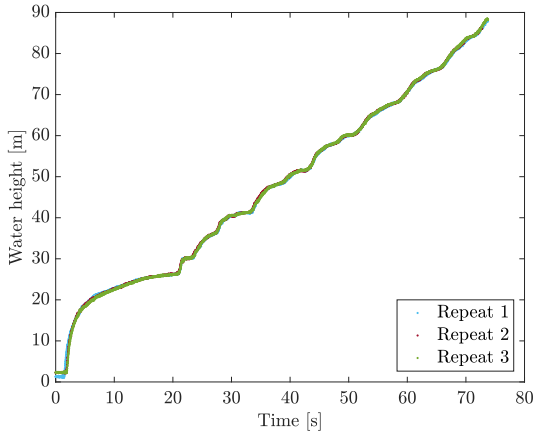

(a) Lowest discharge for the emptying

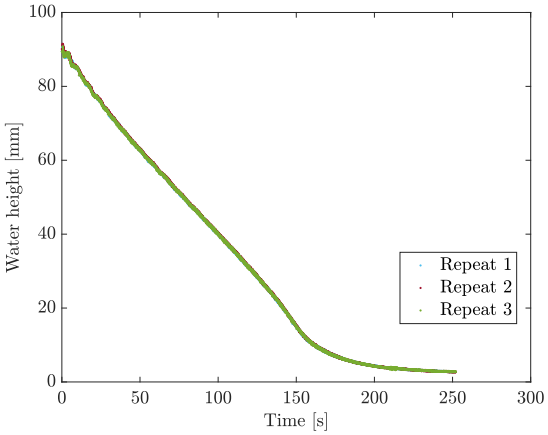

(b) Highest discharge for the emptying

FIG. 24 Three repetitions of the third configuration (for emptying and filling) at sensor 4

The maximum average difference for between the three repetitions of the filling test is 0.32 mm. The largest deviation between these three curves is 1 mm. This maximum deviation here is therefore 1 % of the total cross-section. The uncertainty of the data is therefore maximum of 1 % at the fourth sensor for one discharge. This uncertainty about the data is added to the uncertainty linked to the sensor itself. Indeed, as explained in PART 2.1, there is a uncertainty on the data return by the sensors due to their precision.

The average difference between the three curves is shown in Tab. 9. The blue percentages represent the emptying and the black one represent the filling. There is a difference between the two because the tests were not carried at the same time. The conditions might have changed in between. The maximum deviation is not shown because it corresponds to a pic that would not be considered in the average as explain in the Part 3. These large deviations are not taken into account in the average curve that will be analysed. This is done in the last part of the data cleaning.

	Configuration 1		Configuration 2		Configuration 3		Configuration 4	
Sensor	Average gap [%]	Average gap [%]	Average gap [%]	Average gap [%]	Average gap [%]	Average gap [%]	Average gap [%]	Average gap [%]
1	1.81	0.77	1.02	1.26	1.4	1.60	1.87	1.52
2	1.71	0.44	1.09	0.96	1.22	0.35	0.57	0.97
3	0.56	0.41	1.9	0.94	0.54	0.37	1.47	0.92
4	0.54	0.37	0.82	0.83	0.23	0.32	1.26	1.02
5	0.84	0.37	1.77	0.91	1.06	0.34	1.65	1.01
6	1.44	0.37	1.26	1.18	1.49	0.66	1.54	1.04

Tab. 9 Maximum and average difference between the three repetitions for every configuration and sensors

Looking at the table, we can see that the average gap remains relatively small as it is less than 2 % of the total section. For the first configuration of the filling, the average deviation is less than 1 % of the total section. The uncertainty on the first configuration is quite low since it is smaller than the uncertainty of the sensor. For the second configuration, apart from the first and sixth sensor, the other sensors have an average error smaller than 1 %. Concerning the emptying, the second configuration has a greater average gap. No sensor has a gap greater than 2 %. For the first sensor in configuration three, the maximum deviation is quite high. The order of magnitude is still less than 2 %. The other sensors have an average deviation smaller than 1 %. Configuration four has four sensors with a deviation greater than 1 %. These deviations remain very close to 1 % and are therefore close to the accuracy of the sensor.

2 Results of the filling tests

In this section, the results for the smallest discharge will be shown. The graphs presented show the evolution of the water depth in the pipe as a function of time for each sensor. The pipes are not empty at the beginning of the test. The initial condition is 1.9 mm in the pipes.

Fig. 25 shows the evolution of the water level in the first sensor after the tank for the first configuration. The total time of the simulation is 255 seconds.

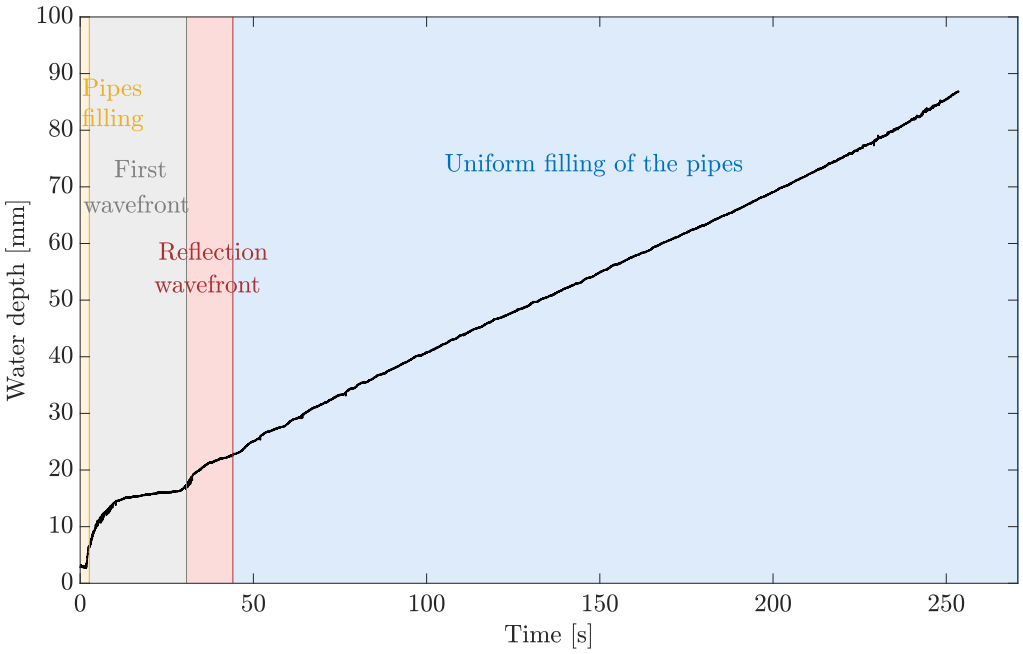

FIG. 25 Evolution of the water level at sensor 1 for the lowest discharge

The graph is divided into four zones. The first zone corresponds to the arrival of the water in the pipe. It takes a 2.81 seconds seconds before the water arrives. Then, the first wave front propagates with an amplitude of 16 mm. This wave propagation lasts 29.8 seconds. Then, the reflection of the front on the edge of the pipe can be observed. This is the one meter long pipe right after the tank. The amplitude of the wave reflection is 22.1 mm. This wave reflection lasts 15.8 seconds. Finally, the last phase is the quasi-uniform filling of the pipes. The volume increases uniformly in all pipes. This phase is the longest one and lasts 209 seconds. The maximum water depth observed in the pipe is 86.88 mm. As explained before, the pipes are not pressurized so the water depth does not reach the top of the pipe. With a constant discharge corresponding to the average discharge of the test, it would take 270.5 seconds to fill the entire system.

The evolution of the water level at the second sensor is shown on FIG. 26. This sensor is right after an intersection. The amount of water that arrives is divided by two compared to the first sensor. The four zones presented for the first sensor are the same for this second sensor but the height of the curve and the time of each phase are different.

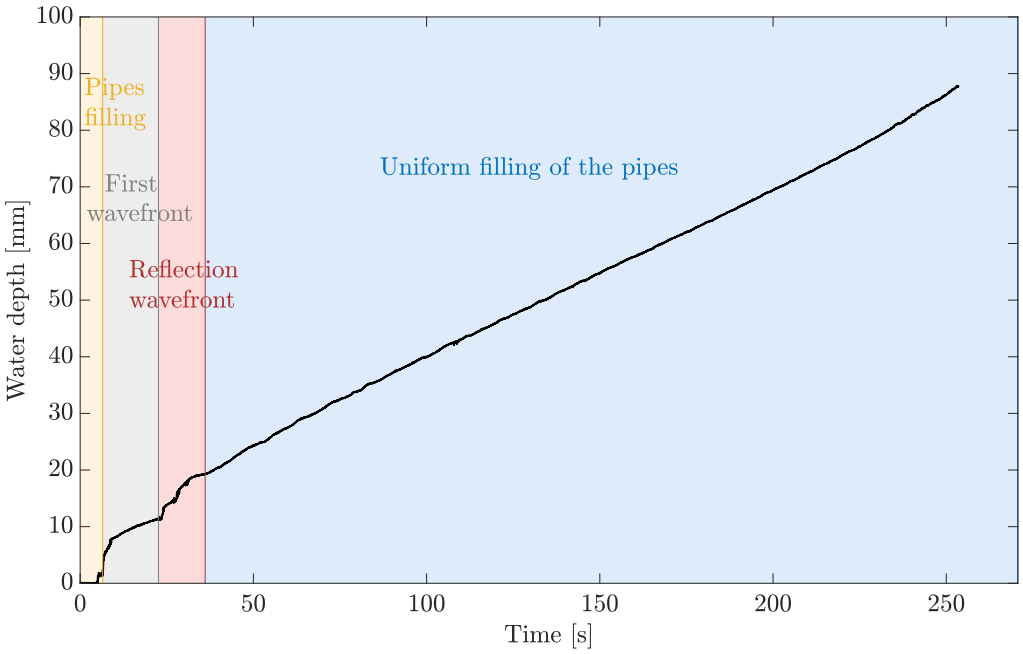

FIG. 26 Evolution of the water level at sensor 2 for the lowest discharge

The water takes 7.81 seconds to reach the location of the sensor. Then, the first wave front arrives. The amplitude of this first wavefront is 11.25mm. The propagation time of this front is 16 seconds. The pipe is two meter long and the water reflects at the end of the pipe. The reflection is less clear than for the previous sensor. The amplitude of this reflection is 17 mm. This reflection lasts for 13.5 seconds. Finally, the curve follows the uniform filling curve. The water at this sensor has risen to 87.75 mm. The water depth at the end of the test is a 0.87 mm higher than the water depth for sensor one. This can be explain be the precision of the sensor. The water level is not perfectly horizontal at the end of the test. Some little difference in the water depth can be found.

FIG. 27 shows the evolution of the water depth at the sensor three. This is the sensor on the same pipe than the sensor two. It is the last sensor that measured water in a pipe that will be presented.

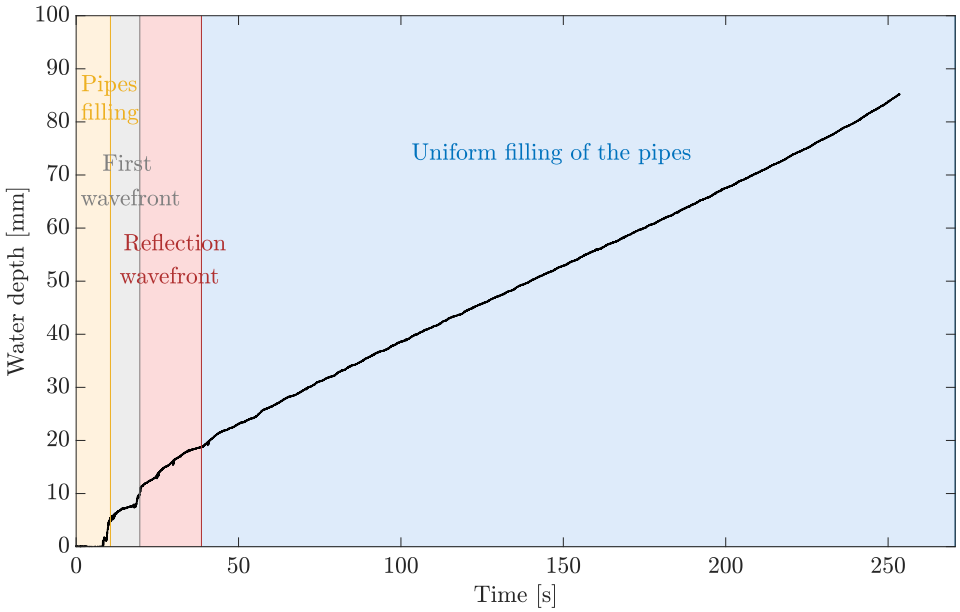

FIG. 27 Evolution of the water level at sensor 3 for the lowest discharge

It takes 10.5 seconds for the water to reach this sensor and the wave front can be seen. It propagates for 8 seconds with an amplitude of 7.6 mm. The duration is greater than for the two other sensors and the amplitude is lower. Then the wavefront is reflected on the end of the pipe. As this sensor is close to the end of the pipe, the reflection happens more quickly. Several reflection waves can be observed. Indeed, by being close to the end of the pipe, a large number of reflections occurs before stabilising. This phase lasts for 21.5 seconds. Finally, the uniform filling phase takes 215 seconds to reach an height of 85.15mm in the pipe.

The evolution in water level at sensors four, five and six are not presented here as they are similar to FIG. 25, 26 and 27 respectively. The biggest difference is that the sensor four and five are on the same pipe. Thus, there is no intersection between these two sensors. The duration of each part described above for each sensor is presented in the TAB. 10.

Time	Pipes filling	First wavefront	Reflection wavefront	Uniform filling
Sensor 1	2.64 s	27.36 s	16 s	209.1 s
Sensor 2	7.81 s	15.28 s	14.31 s	217.6 s
Sensor 3	10.5 s	8.1 s	21.3 s	215.1 s
Sensor 4	3.71 s	27.19 s	18 s	206.1 s
Sensor 5	4.39 s	21.5 s	21 s	208.1 s
Sensor 6	10.9 s	7 s	15 s	222.1 s

TAB. 10 Time of the different phase of the filling

The two closest sensors to the tank are sensors one and four. The two sensors closest to the reservoir see the water arrive first. Sensor one is 30 cm away from the tank while sensor four is 47 cm away from it. The water arrives faster at sensor one. The uniform filling phase is the longest for all sensors. The water first reaches sensors one and four and then sensors two and five. Since sensor five is on the same pipe as sensor four, the water arrives there faster. As the sensor two is after an intersection, the water takes more time to get there. Sensor three and six

are the furthest away from the tank and the water take more time to reach these two sensors. The propagation of the wavefront is also shorter for these two sensor. The sensor one and four have the longest wave propagation as they are the nearest to the tank.

Tab. 11 shows the water depth at the end of the four phases. The first column therefore represents the initial conditions which is the same for all sensors. Then, the second column represents the height of the wave front at the end of the propagation. The third column represents the water depth at the end of the reflection phase. The last column gives the water depth at the end of the test. As the filling is not perfectly uniform, the final height differs depending on the position of the setup. However, the different heights remain similar.

Water depth	Initial	First wavefront	Reflection wavefront	End
Sensor 1	1.9 mm	16.1 mm	22.3 mm	86.9 mm
Sensor 2	1.9 mm	11.2 mm	19.3 mm	87.75 mm
Sensor 3	1.9 mm	7.5 mm	18.6 mm	85.2 mm
Sensor 4	1.9 mm	14.8 mm	22 mm	86.35 mm
Sensor 5	1.9 mm	13 mm	21 mm	85.4 mm
Sensor 6	1.9 mm	7 mm	16.4 mm	87.75 mm

Tab. 11 Water height at the end of the different phase of the filling

It can be seen that the closer the sensors are to the tank, the greater the amplitude of the wavefront. When the sensors are after an intersection, the amplitude of the wavefront decreases. This is due to the fact that the water splits in two to leave on either side of the intersection. The sensors four and five are on the same pipe. The pipe is two meters long. This explains why the amplitude of the wavefront of these two sensors are similar.

For the other configurations, the description is the same. The major difference is the simulation duration and the amplitudes. The greater is the flow rate, the fewer simulation time is needed. The first zone is therefore shorter for the other configurations. As the flow rate increases, the amplitude of the wavefront is higher. The reflection is sometimes less pronounced at higher flow rates. Finally, the higher the discharges, the shorter the last zone. These graphs will not be presented in the description of the results.

Fig. 28 represents the evolution of the water in the tank. For this purpose, the whole curve has been represented, including the filling of the injection tank. This part of the curve is logically in the negative part of the graph because of the chosen frame of reference. The dot horizontal line corresponds to the zero water depth.

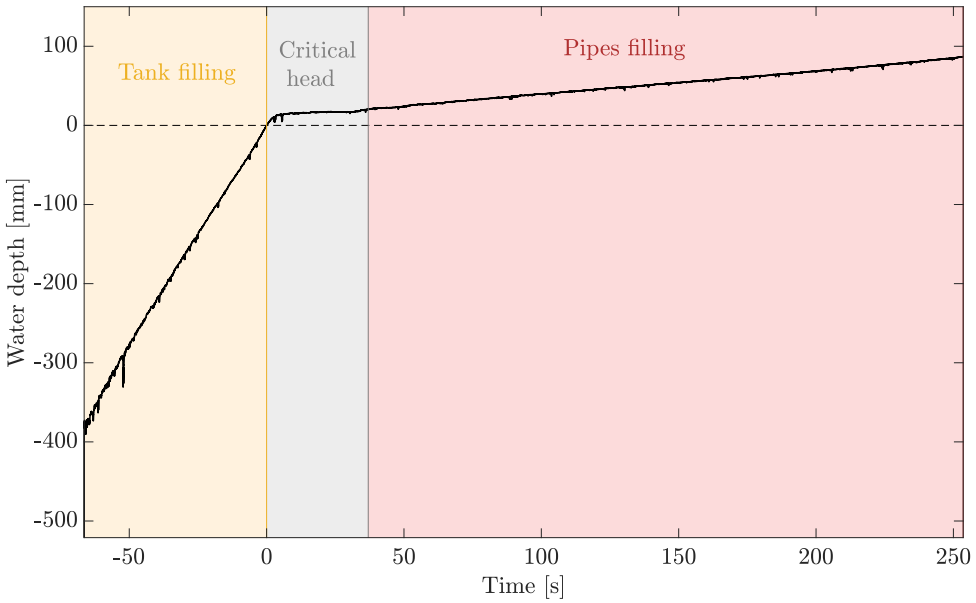

FIG. 28 Evolution of the water level at sensor 7 for the lowest discharge

The first area, which is entirely in the negative part of the graph, represents the increase of water in the tank. The filling follows a classic filling curve. It takes 60 seconds before the tank is filled. Then, a plateau corresponding to the entering of the water in the pipes is observed. At this point, a critical flow is observed. This critical flow takes place while equilibrium is being achieved with the pipes. The observed height of this tray is 16.5mm. This critical load is observed for 32 seconds. Then, uniform folding is observed in the same way as for the other sensors. The slope of the curve for this sensor is the same as for the others and corresponds to the slope of uniform filling.

3 Results of the emptying tests

The results presented in this section are those of the emptying tests. The flow is purely gravitational. Indeed, no pump or turbine is involved in the flow. It is however interesting to analyse these results. The pipes are not completely filled at the beginning of the flow. The pipes are never pressurized, so the pipes are filled to 95 % of their capacity for these tests.

As the graphs are similar for all configurations, only the configuration two is presented. As for the filling of the pipes, all the graphs are similar. Thus, only one sensor from the pipes will be analysed. As the sensor above the central tank gives a different result, it will also be presented.

FIG. 29 represents the evolution of the water depth at the sensor four for the second configuration. The pipe is initially filled at 95 % of the diameter of the pipe.

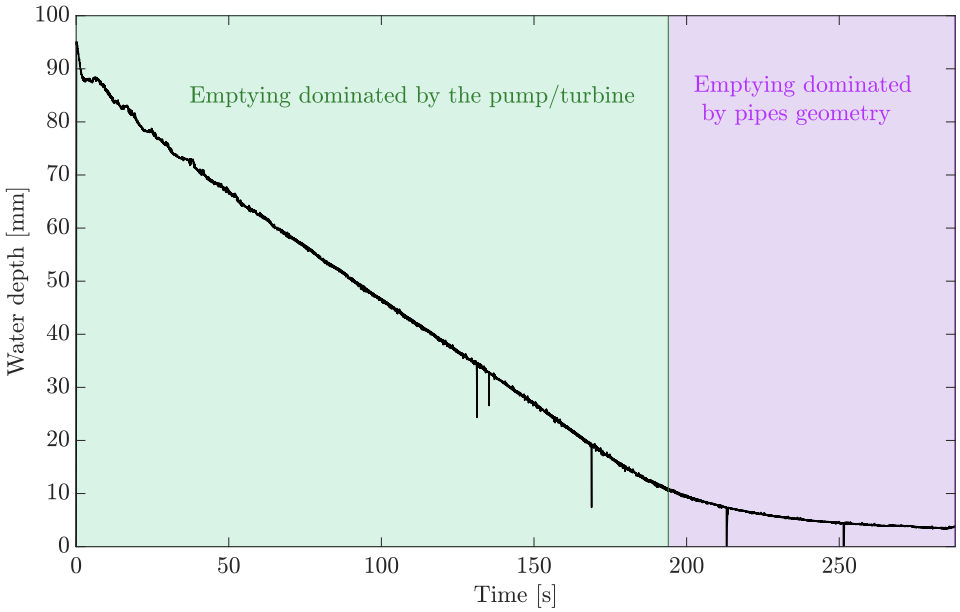

FIG. 29 Evolution of the water depth at sensor four for configuration two

The evolution of the water level can be divided into two phases. The first phase is conditioned by the pump/turbine. In reality, the pump determines the flow rate that allows the water to rise to the lower reservoir. In the laboratory, it is a gravity flow. The flow is therefore governed by gravity. Then, a second phase can be observed. The slope becomes relatively shallower. In this part of the graph, only the geometry of the pipes influences the flow. The water in the reservoir is lower than the level of the pipes. The flow is therefore determined solely by the pipes. This flow is a critical flow as it is a free-falling water flow. The line demarcating the two phases is positioned at the time when the water leaves the pipes.

At the very beginning of the curve, some small waves can be seen and then stabilise. When the valve opens, the height in the reservoir decreases. The water in the pipes is therefore drawn into the reservoir. As the cross-sectional area of the reservoir is much smaller than the one of the pipes as a whole, a balance is created. Once the equilibrium is created, the water flows back down into the reservoir. This process is repeated several times. The flow then follows the emptying curve.

FIG. 30 represents the evolution of the water depth in the tank. The height zero corresponds to the level of the pipes. The evolution in the reservoir is nevertheless presented. These heights are therefore in the negative part of the graph. The dot line represents the level of the pipes.

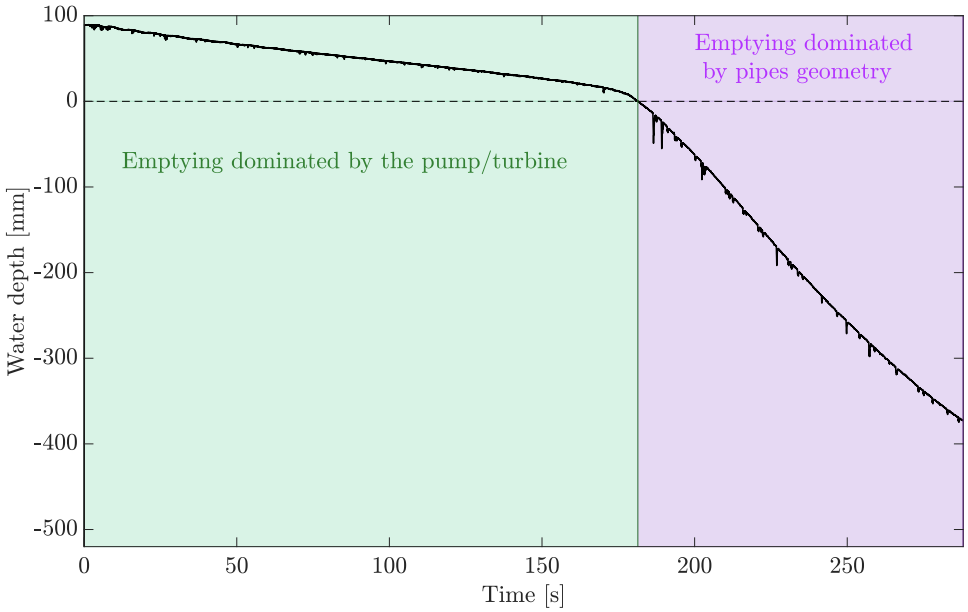

FIG. 30 Evolution of the water height in the tank for the second configuration

Here too, the graph can be divided into two main parts. The first part concerns the time when the flow is dominated by gravity. Then, the moment when the geometry of the system comes into play. After 180 seconds, the water level is lower than the level of the pipes.

At the beginning of the curve, small waves are also observed. This is due to the same reason as for sensor four. These small waves are obviously present here since the balance is between the pipes and the reservoir. The wave are less visible on this graph because the scale of the graph is different. However, they are clearly present.

For other sensors and other configurations, the graphs are all similar. They can be divided into two zones. A zone where the flow is governed by a pump/turbine and one governed by the geometry of the pipes. The larger the gates opening, the greater is the flow rate. The simulation time is therefore shorter. The wave at the beginning has a bigger amplitude for bigger flow rate. As far as the different sensors are concerned, the closer they are to the reservoir, the more the reservoir's influence is visible. The wave at the beginning are therefore more visible on the sensors closest to the reservoir.

Part V
Presentation and results of the numerical model

In this section, the numerical model implemented to model what happens in the laboratory will be presented. This model will be validated via several theoretical validations and via the laboratory results. It will therefore be able to represent what happens in the laboratory as well as what would happen in reality. The model only takes into account the hydraulic part of the setup.

1 Description of the method

The model implemented here is a one dimensional model that uses the finite volume method to solve the equations of mass and momentum conservation integrated on the gallery flow cross section. As the flow studied is unsteady, the explicit time integration is performed using two-step Range-Kutta. The value of the Range-Kutta constant is 0.5.

The conservation of mass equation is given at Eq. 10. The momentum conservation equation is given at Eq. 11.

$$\frac{\partial A}{\partial t} + \frac{\partial Q}{\partial x} = 0 \tag{10}$$

$$\frac{\partial Q}{\partial t} + \frac{\partial}{\partial x}\big(Q \cdot u + g \cdot A \cdot h\big) = g \cdot A(S_0 - S_f) + v_x \cdot q_l \tag{11}$$

In the conservation of momentum equation, some terms are neglected as there is no bottom slope. The term S_0 is therefore zero. There are also no lateral contributions and the term $v_x \cdot q_l$ equal to zero. The simplified equation is shown in Eq. 12.

$$\frac{\partial Q}{\partial t} + \frac{\partial}{\partial x}\big(Q \cdot u + g \cdot A \cdot h\big) = g \cdot A \cdot S_f \tag{12}$$

Being in a circular section, it is not possible to work in terms of water depth and specific flow as the width is not constant. The two working variables are the section and the full flow rate. The equations will therefore be discretised as described below. The discretised mass conservation equation is shown in Eq. 13.

$$\frac{A_i^{n+1} - A_i^n}{\Delta t} + \frac{Q^n_{i+\frac{1}{2}} - Q^n_{i-\frac{1}{2}}}{\Delta x} = 0 \tag{13}$$

The index i represents the spatial time step while the index n represents the time step. The working variables are evaluated at the node i from values reconstructed at the edges.

Eq. 14 represents the discretised conservation of momentum equation.

$$\frac{Q_i^{n+1} - Q_i^n}{\Delta t} + \frac{(Q \cdot u)^n_{i+\frac{1}{2}} - (Q \cdot u)^n_{i-\frac{1}{2}}}{\Delta x} + g \cdot \frac{(A \cdot h)^n_{i+\frac{1}{2}} - (A \cdot h)^n_{i-\frac{1}{2}}}{\Delta x} + g \cdot A \cdot Head_{loss} = 0 \tag{14}$$

The head loss is calculated using Manning's formula. The Manning's coefficient will be a parameter to be calibrated as it is not known. The pipes are in PVC, so it is possible to estimate this coefficient. The head loss is calculated via the Eq. 15.

$$Head_{loss} = \left(\frac{1}{K}\right)^2 \frac{Q^2}{\left(\frac{\Omega(h)}{L(h)}\right)^2 \cdot R_h^{4/3}} \tag{15}$$

To calculate this head loss, the hydraulic radius must be known. The hydraulic radius in circular section is calculated using Eq. 16. The variable D is the diameter of the pipe.

$$R_h = \frac{D}{4} \cdot \left(1 - \frac{\sin\left(2 \cdot \arccos\left(1 - \frac{h}{R}\right)\right)}{2 \cdot \arccos\left(1 - \frac{h}{R}\right)}\right) \tag{16}$$

Since the chosen scheme is an explicit one, it is important to pay attention to the numerical stability. In order to ensure this stability, the choice of the Courant–Friedrichs–Lewy coefficient is important. This coefficient is used to determine the time step. The expression of the Courant–Friedrichs–Lewy coefficient is shown at Eq. 17. The parameter c is the wave celerity. This parameter varies at each time with the speed and the water depth. The value of Δt is the smallest of the domain for a given time step. This represents the larger wave velocity.

$$\text{CFL} = c \cdot \frac{\Delta t}{\Delta x} \tag{17}$$

The larger the Courant–Friedrichs–Lewy coefficient, the larger the time step. The smaller the time step, the easier it is to ensure numerical stability. However, a balance must still be found in order to optimise the calculation time. If the time step is too small, the calculation time will increase. Although the parameters of the spatial and temporal steps are important for numerical stability, their values should not influence the result.

Tab. 12 shows the important parameters chosen for this numerical model.

Parameter	Value
a_1	0.5
Δx	0.01 m
CFL	0.2
Δt	0.02 s

Tab. 12 Important parameters of the numerical model

One other important parameter is the type of reconstruction. A volume is made up of a central node and two edges. When the value at the central node is known, we need to know the value at the edges. This is done via a reconstruction. The reconstruction can be constant. The value at the edges is equal to the value at the centre of the volume. The reconstruction can also be linear. The reconstruction method chosen will be linear reconstruction but a sensitivity analysis will be carried out later.

Although the working variable is the cross-sectional area, it is important to know the value of the water depth. Indeed, the value of the height is necessary in order to solve the conservation of mass equation. The data will be analysed in terms of height and not cross-section. The relationship between the height of the water and the cross-section is a non-linear relationship. When the height of the water is known, it is easy to find the cross section. This can be done via the equation in Eq. 18.

$$\Omega(h) = \frac{R^2}{2}\left(2 \cdot \arccos\left(1 - \frac{h}{R}\right) - \sin\left(2 \cdot \arccos\left(1 - \frac{h}{R}\right)\right)\right) \tag{18}$$

In the model, certain equations require an assessment of the water depth based on the cross-section. The Newton-Raphson method will be used. It is an iterative method for finding the numerical solution to an equation. First, an initial value x_0 must be chosen. This value must be close to the solution. Indeed, if there are several roots to the equation, the method might not find the right root. Then the slope of the function is calculated via the derivative. The derivative is calculated analytically via a classical derivative calculation. The expression of the derivative is at Eq. 19.

$$g(h) = \frac{\partial \Omega(h)}{\partial h} = \frac{R^2}{2} \cdot \frac{2}{\sqrt{1 - \left(1 - \frac{h}{R}\right)^2}} \cdot \frac{1}{R}\left[1 - \cos\left(2 \cdot \arccos\left(1 - \frac{h}{R}\right)\right)\right] \tag{19}$$

Then, the new guess can be calculated. The value of the new guess is calculated via the expression in Eq. 19. The variable $f(x_0)$ in Eq. 18 is evaluated in x_0. The variable $g(x_0)$ is the Newton-Raphson derivative (Eq. 19) also evaluated in x_0.

$$x_1 = x_0 - \frac{f(x_0)}{g(x_0)} \tag{20}$$

Once the new guess is evaluated, the value of $\Omega(x_1)$ is evaluated. Finally it is necessary to check if this solution leads to the convergence or not. If the convergence is ensured, x_1 is the Newton-Raphson solution. If convergence is not ensured, the process starts again from x_1.

2 Implementation

In order to implement what happens in the laboratory in a one-dimensional finite volume model, some assumptions must be made. Firstly, the input data will be the flow rate, which is retrieved from the laboratory via the flow meter. This will make it possible to reproduce what happens in the laboratory. Next, the symmetry of the model is used. The model is totally symmetrical in both planes. The water must therefore be distributed equally in the different pipes. Instead of modelling the four pipes starting from the central tank, only one will be implemented. This means that it is assumed that the flow divides symmetrically. In order to visualise the implementation of the model, the different finite volumes are presented in Fig. 31.

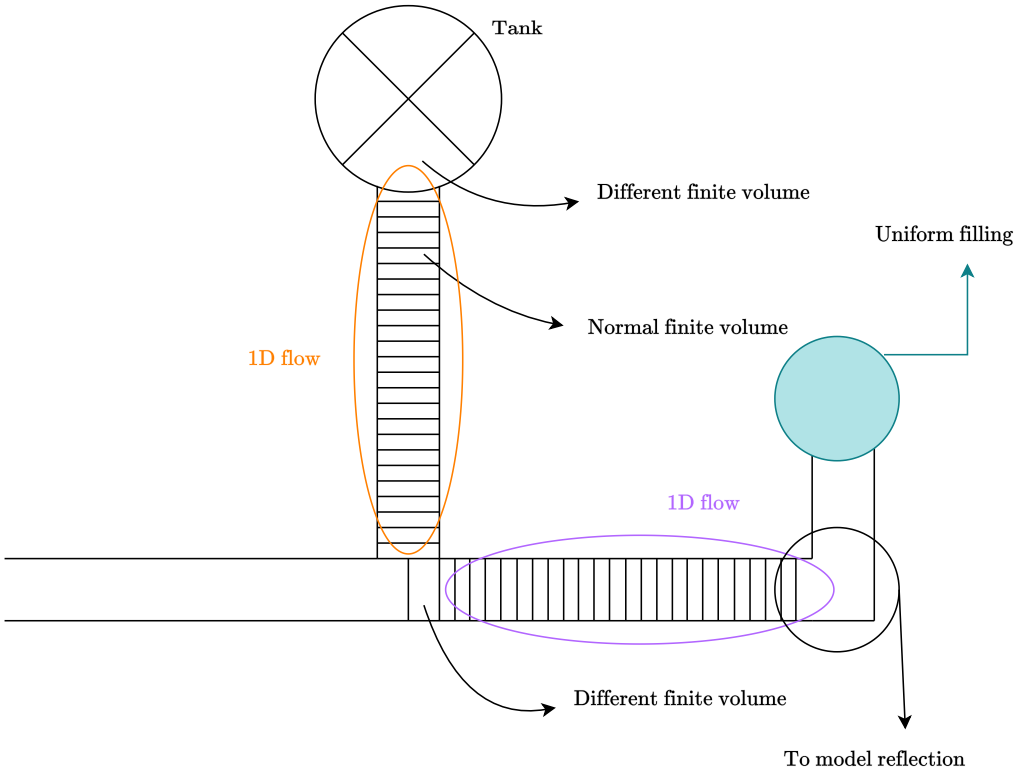

FIG. 31 Working principles of the 1D model

To model intersections, the same thing happens : symmetry is used. Intersections are right-angle intersections and by hypothesis, the water divides perfectly between the two pipes. Here again, only one pipe is modelled. A 1D flow is also taken in this pipe. To keep a one-dimensional flow, assumptions must be made about the finite volumes at the edges of the pipes.

The modelled pipe has a first finite volume with a different geometry than the others. The others are those that make up the circular pipe of 10cm diameter. The first volume represents a quarter of the injection area. For the pipes after the intersection (at the end of the first pipe), again symmetry is used. As for the first pipe, the second pipe has a different first finite volume. This first finite volume will have the characteristics of the last finite volume of the first pipe. Only here the height and flow rate are divided in two. This leads to the assumption that the flow rate is divided in two in both pipes.

3 Validation of the numerical model

In order to validate the numerical model, theoretical concepts will be used. Then, the numerical model will be compared with the laboratory results. Theoretical validation is used to check that the equations have been correctly computed and resolved correctly. Validation with laboratory data verifies that the model is correctly implemented and represents what happens in the laboratory.

3.1 Validation with theoretical concepts

The first step to validate the model was to draw a backwater curve in a linear gallery. The theoretical backwater curve was calculated following Eq. 21.

$$\frac{dh}{dx} = \frac{i - J}{1 - Fr^2} \tag{21}$$

The parameter i represents the bottom slope which is 0.05 mm/m. The parameter J is the friction slope and Fr is the Froude number which is calculated at each step. The expression of the Froude number is shown at Eq. 22

$$Fr = \frac{u}{\sqrt{g \cdot \frac{\Omega}{L}}} \tag{22}$$

The parameter g is the acceleration of gravity 9.81 m/s^2. The flow speed is u. The section and the length can be calculated based on the water depth.

The critical depth is known downstream and is 0.030 m. It is from this height that the backwater curve is calculated. The discretisation used is shown at Eq. 23.

$$h_1 = h_0 + \left.\frac{dh}{dx}\right|_{h_0} \cdot \Delta x \tag{23}$$

The chosen flow rate is $1.9 \cdot 10^{-3} m^3/s$. The friction coefficient K is fixed to 500 $m^{1/3}/s$. The same conditions are implemented in the model.

Fig. 32 represents the theoretical backwater curve and the curve of the numerical model. The condition of the flow implemented is supercritical. The critical water depth is above the uniform water depth. This flow do not represents something that would happen in the pipe. This model is only used to validate the model on the theoretical aspects.

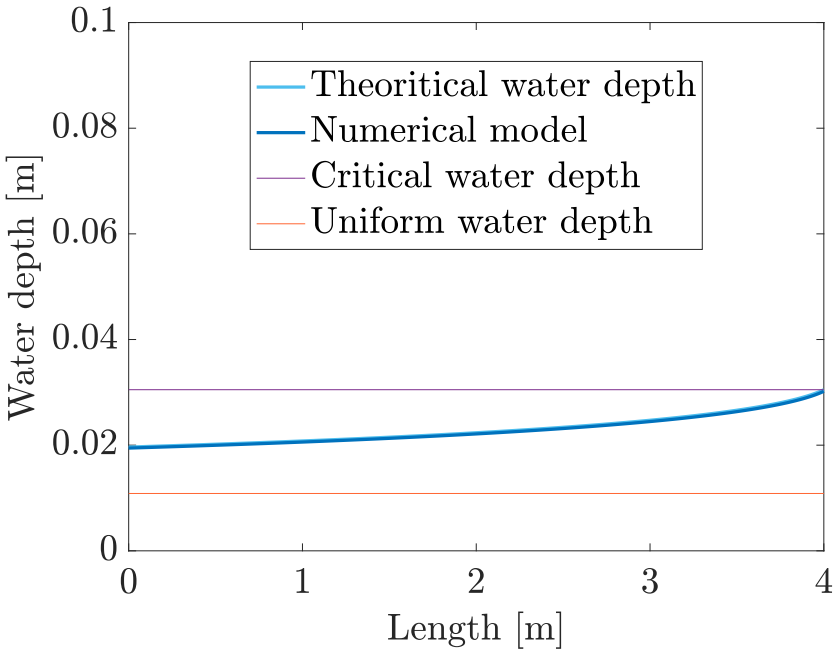

Fig. 32 Comparison between theoretical and numerical water line

The two curves are almost identical. The difference between them is less than one hundredth of a millimeter. It can therefore be concluded that the model correctly uses the equations for the conservation of mass and momentum.

Then, the first finite volume can be verified with the calculation of the critical head. The first finite volume corresponds to the reservoir. As it is explained for the laboratory results, a critical flow appears at the beginning. This plateau must be found in the numerical model. This volume is different from the other finite volume as it is explained at Section 2.

Fig. 33 shows the evolution of the water depth in the first finite volume that represents the reservoir. The discharges used in the model is the fourth configuration, thus the highest discharge. The discharge is not constant, so the plateau is not perfectly straight. The red line corresponds to the critical head that is calculated.

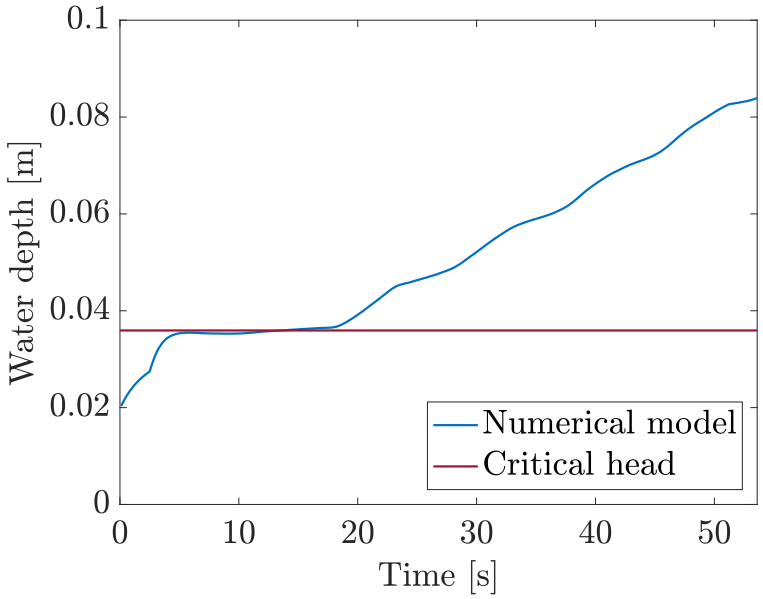

Fig. 33 Numerical curve in the tank compared with the critical head

As it can be seen on Fig. 33, the plateau corresponds to the critical head. After 18 seconds, the plateau is no longer visible on the digital curve and the pipes begin to fill almost uniformly. The first finite volume is therefore well within the critical load range. This volume can therefore be validated.

3.2 Validation with laboratory results

Once the model has been validated against the theory, it can be validated against the laboratory results. Since the discharges measured in the laboratory are injected into the model, the model must reproduce as closely as possible what happens in the laboratory.

Fig. 34 represents the water depth as a function of time for the first configuration. Dot lines represent the laboratory results. The results from three sensors are shown in Fig. 34. Full lines represent the numerical model. The results of the numerical model are presented in the same place as the sensor on the pipe. Each colour represents a position on the pipe, corresponding to the three positions of the three different sensors. Only the 90 first seconds are presented to have a better view on the results.

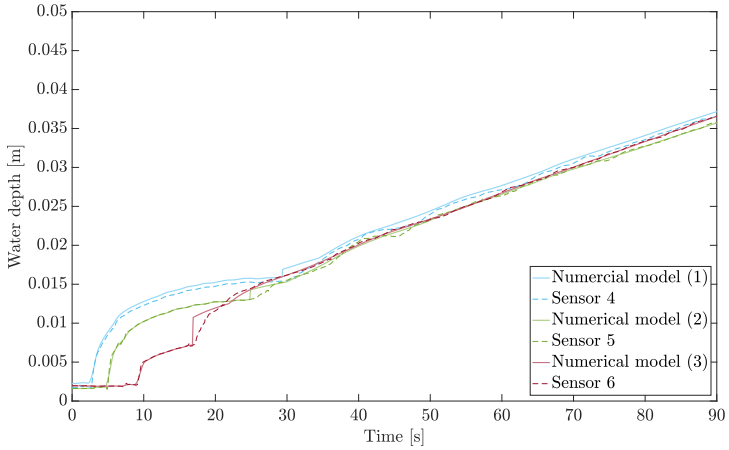

FIG. 34 Comparison between the numerical model and the laboratory measurement for the three last sensors (configuration one)

The arrival of water in the pipes for the numerical model follows the laboratory curve. The wave front arrives slightly earlier in the numerical model than in the laboratory results. This is visible for the three different positions. The numerical curve slightly overestimates the laboratory curve at the wavefront. After the wavefront has propagated, reflections are visible at all three sensors. This part is the least well represented by the numerical model. For sensor six, the curve rises a little too high and therefore does not perfectly follow the measured water level curve. Then, the uniform filling curve starts.

For a better view of the results, each sensor is represented separately on FIG. 35. FIG. 35a represents the location of sensor four (47 centimeters away from the tank). FIG. 35b represents the location of sensor five (1.34 meters away from the tank) while FIG. 35c represents the location of sensor six. The uniform filling curve is more visible on FIG. 35.

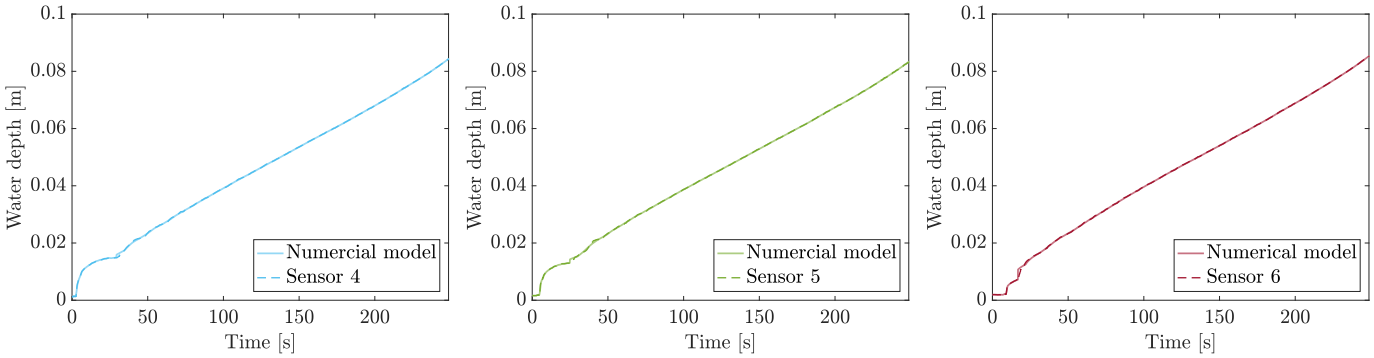

(a) Comparison between the numerical model and the sensor four

(b) Comparison between the numerical model and the sensor five

(c) Comparison between the numerical model and the sensor six

FIG. 35 Comparison between the numerical model and the water depth measured by the different sensors for configuration one

By looking at the different curves separately, it can be seen that the numerical model fits quite well the experimental results. This configuration has the lowest discharge. There is therefore little variations in the experimental curve. The uniform filling part is fairly smooth. The largest

difference between the numerical and experimental curves is less than 1 % of the total cross-section. The probes have an accuracy of 1 %, so it can be concluded that the numerical model is a good representation of what happens in the laboratory.

After comparing the numerical results for configuration one, it will be compared with configuration four. The first configuration is the one with the lowest discharge. This configuration has fewer oscillations. It is therefore interesting to see whether the model works in all configurations.

Fig. 36 represents the numerical model and three experimental curves for the fourth configuration. Again, the dot line represent experimental results while the full line represents numerical curves. A zoom is made on the half on the pipe and the time because beyond that it is the uniform filling curve. Indeed this part is know and the most interesting part is the propagation and the reflection of the wavefront.

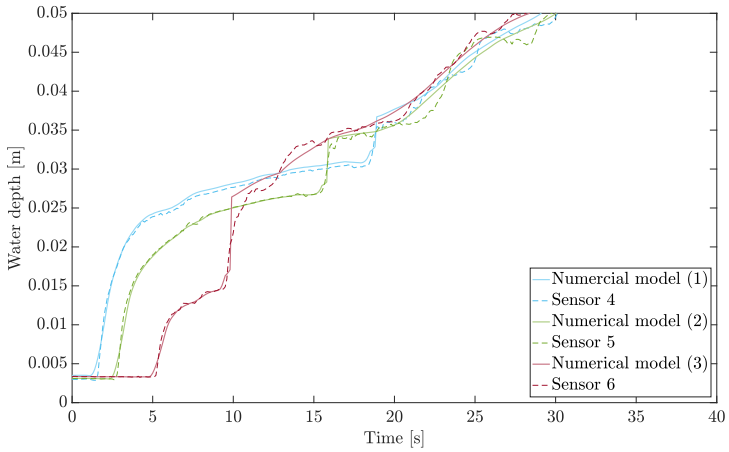

Fig. 36 Comparison between the numerical model and the laboratory measurement for the three last sensors (configuration four)

Blue curves represent the location of sensor four while green and red curves represents the location of sensor five and six respectively. The filling of the pipes and the propagation of the wavefront fit well. There is less than half a millimeter difference between the curves. The three curves represent the reflection after the propagation of the wavefront. For the three curves, the change between the reflection phase and the uniform filling phase is quite abrupt. However, the phenomenon remains well represented.

Fig. 37 represents separately the three sensors with the corresponding numerical curves. Fig. 37a represents the location of sensor four while Fig. 37b and Fig. 37c represents the location of sensor five and six respectively. There is no zoom on the data, the whole curve is shown.

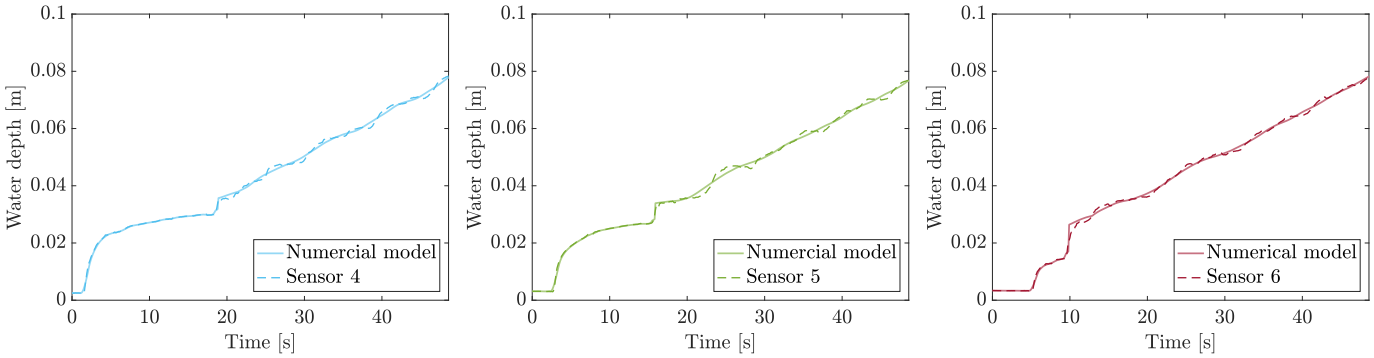

(a) Comparison between the numerical model and the sensor four

(b) Comparison between the numerical model and the sensor five

(c) Comparison between the numerical model and the sensor six

FIG. 37 Comparison between the numerical model and the water depth measured by the different sensors for configuration four

On FIG. 35, the waves produced by the experimental curve at the level of the uniform filling are quite visible. It can also be seen that the reflection is slightly higher in the numerical curve. The reflection is more marked as the FIG. 35b. There is a slight plateau due to the reflection before the uniform filling phase. This is also visible on the experimental curve. However, this phenomenon is more marked on the digital curve. For the comparison at probe six, the reflection phenomenon is even more marked. The reflection is almost vertical.

The maximum difference between the numerical and theoretical curves is always less than 1 % of the total cross-section. This difference does not take into account waves at the level of the uniform filling curve. These waves can cause a difference of 2 mm between the curves.

Then, after looking at the results of the water depth as a function of time, the longitudinal profiles will be studied. On these profiles, the two-meter-long pipe will be represented. Different times will be analysed with the sensor values at the corresponding points.

FIG. 38 and FIG. 39 represent the two-meter pipe connected to the reservoir. It shows several curves from the numerical model represented at different time steps. Each time step is represented by a different color. In order to validate the model, the water level measured by sensors four and five were represented. The sensor measuring in the reservoir was also represented at the beginning of the curve. This sensor is represented by a star. The height of water measured at a precise time by sensor four is represented by a diamond. Sensor five is represented by a square. As the sensors have a certain range of precision, this is represented by gray line in FIG. 38 and FIG. 39.

In order to match the laboratory data as closely as possible, the initial conditions have been implemented in the code. This is the first configuration. In this configuration, pipes are initially filled with two millimeters of water. The input flow rate corresponds to what has been returned by the flowmeter.

FIG. 38 represents the system after 7 seconds, 80 seconds and 120 seconds. The red curve represents the propagation of the wavefront while the green and blue curves represent the quasi uniform filling of the pipes.

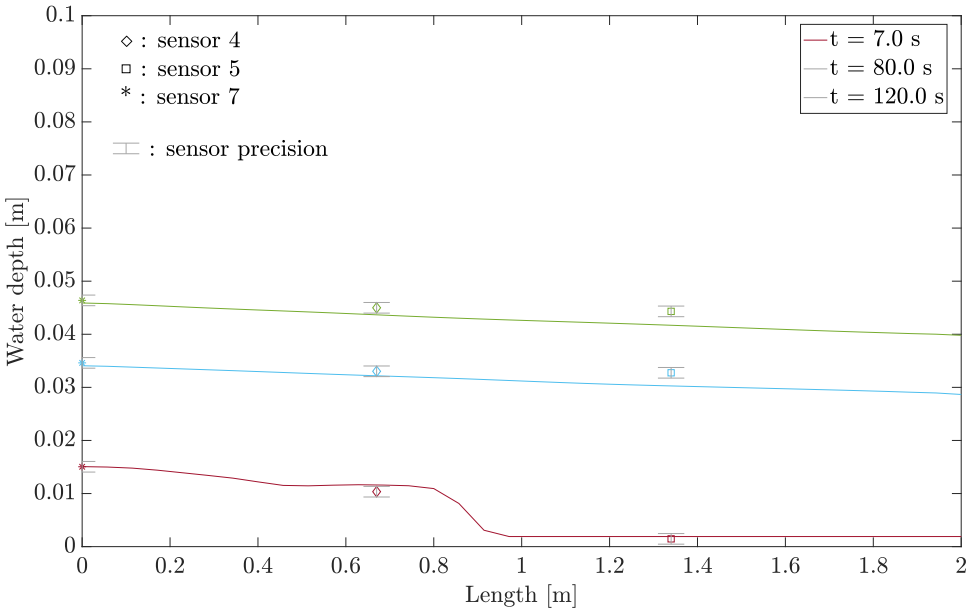

FIG. 38 Longitudinal profile of the two meters long pipe linked to the tank after 7, 80 and 120 seconds

By looking at the red curve, it can be seen that the various sensors follow the curve overall. The point corresponding to the water level in the tank is on the numerical curve. Sensor four is slightly below the curve. By taking into account the range of the sensor precision, sensor four do not correspond to the the numerical curve. The difference between the upper bound of the sensor precision and the numerical curve is less than a tenth of a millimeter. Sensor five measured the initial condition at that time, indeed the wavefront is not yet arrive. The point of the sensor correspond to the numerical curve. For the blue curve, the point corresponding to the sensor in the reservoir is above the curve. However, the numerical curve is in the range of precision of the sensor. This is the same for sensor four. Sensor five is above the curve and the range of precision is also above the numerical curve. The difference between the lower bound of the sensor precision and the numerical curve is 1.5 millimeters. For the green curve, the conclusions are the same than for the blue one except for sensor four which is a tenth of a millimeter above the numerical curve.

FIG. 39 represents the system after 13 seconds, 100 seconds and 200 seconds. The red curve represents the propagation of the wavefront. The difference with the FIG. 38 is the location of the wavefront.

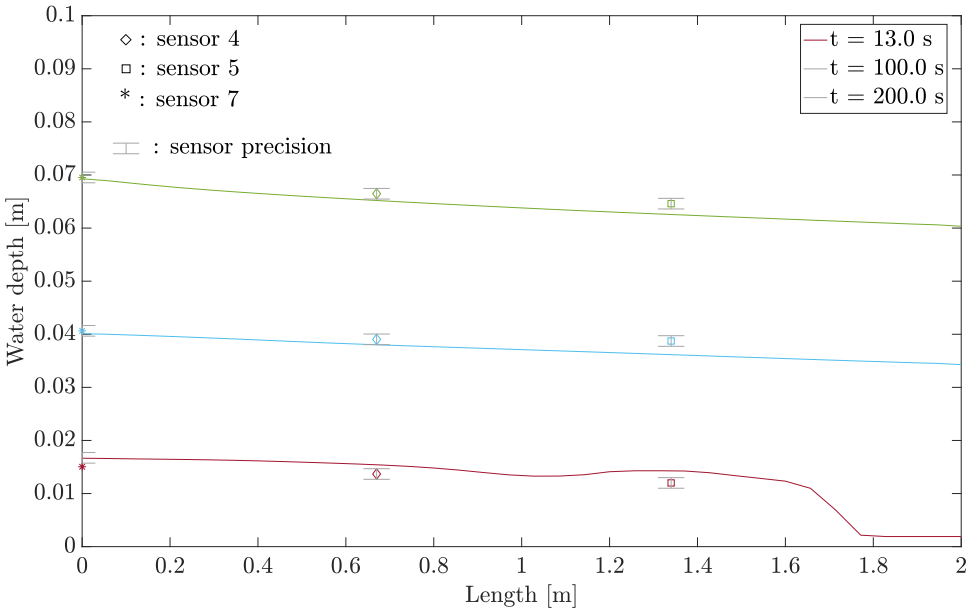

FIG. 39 Longitudinal profile of the two meters long pipe linked to the tank after 13, 100 and 200 seconds

By looking at the red curve, it can be seen that the numerical model overestimates the laboratory results except for sensor seven. The maximum overestimate is 1.5 mm. This is the difference between the numerical curve and the upper bound of the sensor precision. The beginning of the blue curve estimates correctly the laboratory measurements. The end of the curve underestimates the laboratory result. The lower bound of sensor five is 1.8 mm higher than the numerical curve. The conclusion for the green curve is almost the same. For sensor four, the lower bound is above the numerical curve but the difference between the two is less than a tenth of a millimeter. For sensor five, the difference is smaller than for the blue curve. The order of magnitude of this difference is 1 mm.

In conclusion, the differences between the results of the numerical model and the laboratory results are fairly small. The numerical model also corresponds well to the theoretical concepts. The model can therefore be validated.

4 Presentation of the results

Firstly, the evolution of the water level as a function of time will be presented. Secondly, the longitudinal profile will be presented for some different time. This profile would be shown on a two meter long pipe.

FIG. 40 represents the evolution of the water depth in function of the time. The location is fifty centimeter away from the entrance reservoir. The discharges used for this curve is the discharge of the first configuration. This configuration has the smallest discharges.

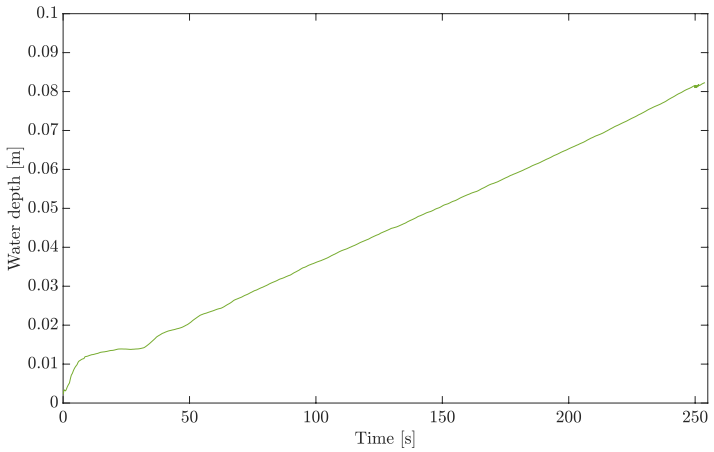

FIG. 40 Evolution of the water depth

There is an initial condition for this simulation. The pipes are not considered empty. There is three millimeters of water inside the pipes when the simulation starts. First, the wavefront can be seen, its amplitude is 16mm. Then, a small reflection can be seen. And the end of the curve is a uniform filling curve the system. This phase appears after 65 seconds.

FIG. 41 represents the water depth in a two meter long pipe at five different times. The discharge used for this profile is the third discharge. This discharge is greater than the discharge used for the evolution of the water depth in FIG. 40.

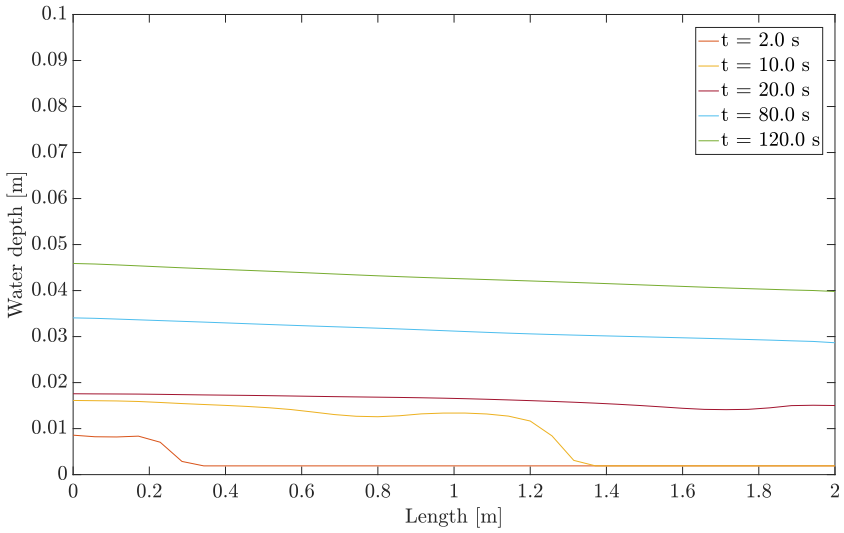

FIG. 41 Evolution of the water level in the pipe for several specified times

The orange curve represents the water in the pipe after two seconds. It shows the propagation of the first wave front and the presence of the two millimeters at the origin in the pipe. The front arrives 30 centimeters from the start of the pipe. The yellow curve shows the continuation of the wavefront propagation. The wavefront is 130 centimeters away from the start of the pipe. The wavefront is higher than at the very beginning. The bordeau curve shows the state of the pipe after 20 seconds. The wavefront has reached the end of the pipe. A slight reflection can be

observed at the end of the pipe. The blue and green curves represent the state of the pipes at 80 and 120 seconds respectively. The pipes are filling evenly.

5 Sensibility analysis

Various sensitivity analyses will be carried out in this section. Firstly, the spatial and temporal steps will be analysed. These should not influence the final results. Then, a sensitivity analysis of the friction coefficient will be carried out. Finally, the type of reconstruction will be analysed.

5.1 Spatial step

The choice of the spatial step should have no influence on the results. A larger step size will give a greater precision. However, the larger the spatial step, the longer the calculation time. A optimisation need to be done between the accuracy and the duration of the calculation. To test the influence of this parameter, all the other parameters are fixed and will remain identical for each spatial step. The CFL coefficient is fixed at 0.2 and the Manning friction coefficient is 200 $m^1/3/s$.

Four different spatial were tested. Fig. 42 represents the four different spatial steps at the time of 100 seconds. They have been all represented at the same time to allow the comparison.

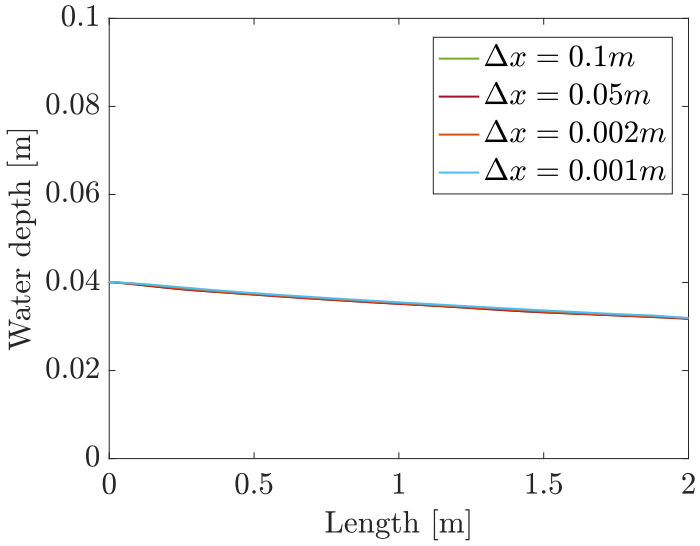

Fig. 42 Comparison between four spatial steps

The influence of the spatial step is not really visible. In fact, increasing or decreasing the spatial time step has no influence on the result. Now the calculation time should be analyse to not have a too long calculation time.

Δx [m]	Calculation time [s]
0,1	58,91
0,05	124,57
0,002	563,55
0,001	2055,26

Tab. 13 Calculation time for each spatial step tested

The calculation time increases considerably as the spatial step size decreases. It is not interesting to have a spatial step of 0.001 m as the accuracy do not increase and the calculation time is more than 30 minutes. The spatial spacing chosen will be 0.05m in order to limit calculation time.

5.2 Time step

The influence of the time step is analysed by analysing the influence of the CFL. The CFL coefficient is used to obtain the time step from the spatial step. For this analysis, the spatial step is set at 0.05m. The coefficient of friction is set at 200 $m^{1/3}/s$. This coefficient is used in Range-Kutta schemes to limit numerical oscillations. Taking this coefficient too large could therefore lead to unwanted oscillations.

As with the spatial time step, four different CFL coefficients will be analysed. An optimum balance between accuracy and computing time need to be found. Fig. 43 shows the evolution curve of the water depth as a function of the time. This represent a point thirty centimeters away from the reservoir for the four CFL coefficients chosen.

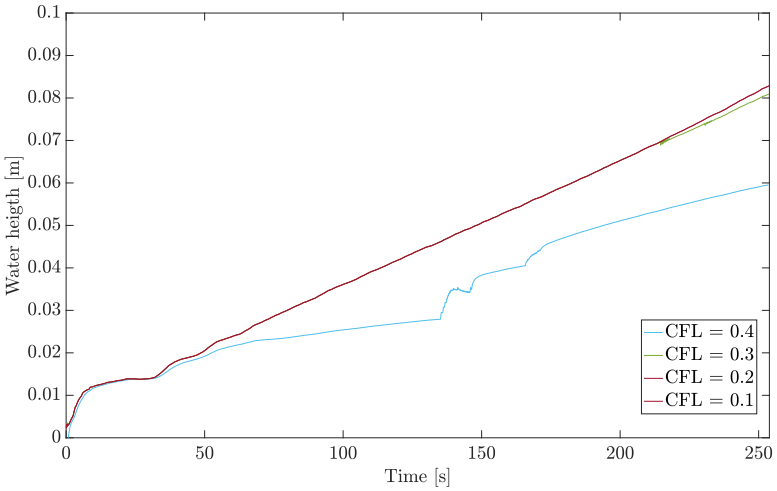

Fig. 43 Comparison between four different CFL coefficient

The two lowest CFL coefficients are similar and do not show any oscillations. The CFL coefficient of 0.3 gives a curve with a slight deviation and some oscillations at the end. The largest CFL coefficient tested gives numerical oscillations fairly quickly. It is not conceivable to work with such a large CFL coefficient.

Tab. 14 shows the calculation time for the four time steps tested in Fig. 43.

CFL [-]	Calculation time [s]
0.4	106.42
0.3	139.72
0.2	247.38
0.1	387.44

Tab. 14 Calculation time for each of the time step tested

The smaller the coefficient, the longer the calculation time. The two largest values, which do

not give good results, will therefore not be chosen. Given that the CFL coefficient of 0.2 and 0.1 give similar results, the CFL coefficient of 0.2 will be preferred given its shorter calculation time.

5.3 Friction coefficient

The law of friction used is Manning's law. The Manning's coefficient (K) must therefore be evaluated. This coefficient is not known in advance. However, PVC materials do not generate much friction. Once again, four different values will be tested. The various coefficients proposed are coefficients that can be found for PVC pipes. PVC coefficients often vary between 150 $m^{1/3}/s$ and 900 $m^{1/3}/s$. However, a lower coefficient will still be tested to see the influence.

FIG. 44 shows the evolution of the water depth in function of the time for four different friction coefficients. The discharge of the first configuration is used.

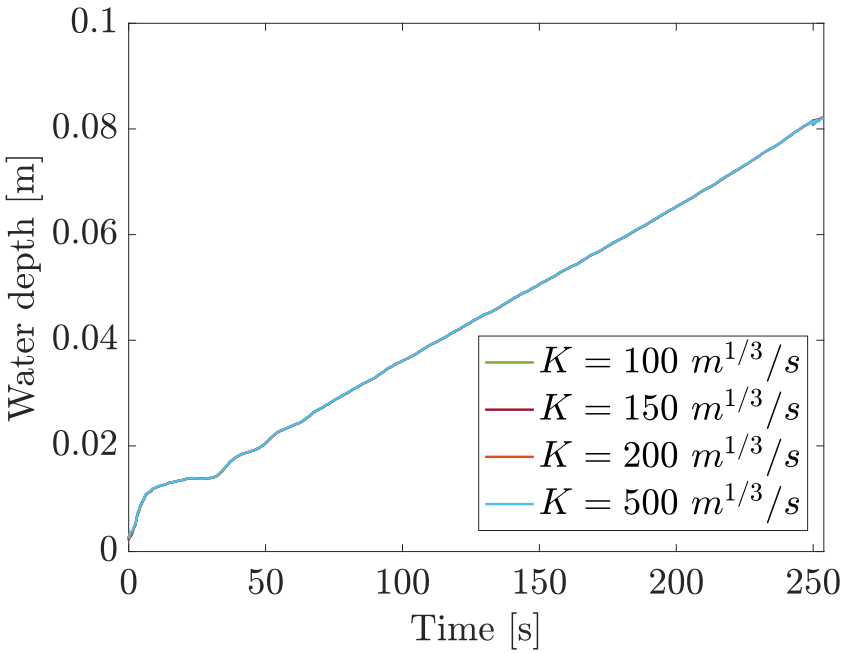

FIG. 44 Different friction coefficient

The coefficient of friction has no influence on the system. K coefficients greater than 150 represent very low friction. Virtually no friction is present. The lowest friction coefficient requires a change of parameter. The spatial step must be reduced to avoid numerical oscillations at the end of the curve. However, by adjusting the spatial step, no difference between the different coefficients of friction is visible.

5.4 Reconstruction type

In order to study the influence of the type of reconstruction, the calculation conditions will be similar for both. The discharge tested is the fourth, this is the highest flow rate. The spatial step is 0.05 m and the CFL coefficient is 0.2. The coefficient of friction is set at 200 $m^{1/3}/s$.

FIG. 45 shows the evolution of the water depth in function of the time for a constant and a linear reconstruction.

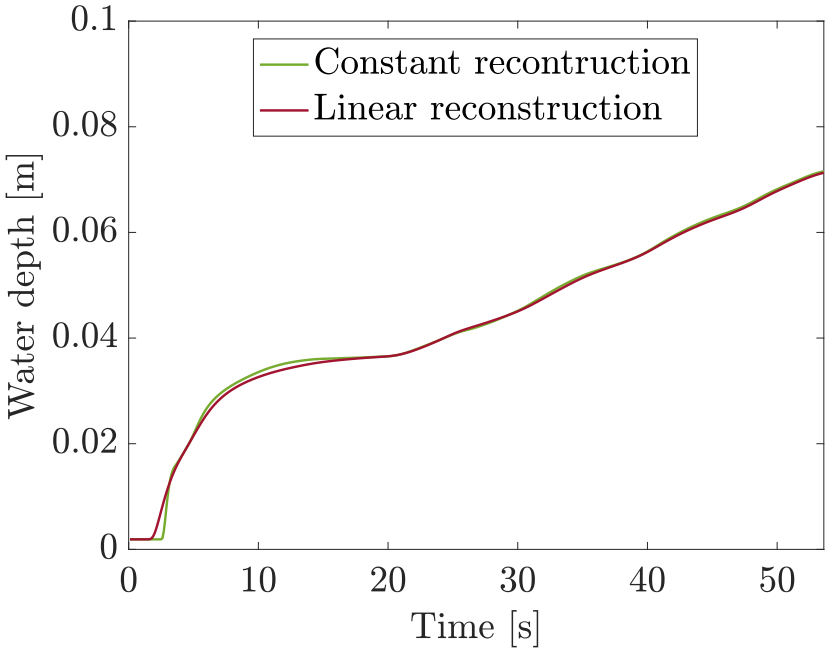

FIG. 45 Sensibility analysis of the different reconstruction type

The two curves are fairly close to each other. The trends followed by the curves are similar. When the wavefront arrives, the linear reconstruction starts less than half a second earlier. As the wavefront propagates, the constant reconstruction rises slightly above the curve. The maximum difference between these two curves is of the order of a millimeter. The difference between the two curves can therefore be described as small because it does not exceed the percentage of the complete section.

TAB. 15 shows the different calculation times for the two reconstruction times.

Reconstruction type	Calculation time
Constant	124.65
Linear	126.96

TAB. 15 Calculation time for the two reconstruction

It can be seen that the calculation times are quite similar. The difference is 2.31 seconds. As the curve corresponds quite good and the difference in the duration of the calculation is low, both reconstruction can be used. The chosen reconstruction type is a linear reconstruction. This reconstruction is theoretically more precise.

Part VI
Analysis and discussion

In this section, the results presented in the previous sections will be analysed and discussed. The laboratory results will be analysed first. As the numerical model has been validated with the laboratory results before, an application will be studied. A real size setup will be modelled. The analysis of the results will be discussed in this section.

1 Analysis of the laboratory results

1.1 Dimensionless variables

In order to have a better view on some results, the useful quantities will be dimensionless. To make the water depth dimensionless, the diameter is used. The characteristic length is shown at Eq. 24. This means that dimensionless depth is equal to one when the pipes are fully filled and equal to zero when the pipes are empty. This value will be the same for all discharges.

$$h^* = D = 0.1m \tag{24}$$

For making the time dimensionless, the characteristic value will be defined as the time it takes to fill the tank completely. The characteristic equation of time is shown in Eq. 25. The total volume of the setup is 0.1456 m^3. This volume is calculated by taking into account the size and cross-section of the pipes (assumed constant). The arrangement between the pipes and the main tank is also taken into account to ensure that the total volume is as accurate as possible.

$$t^*_{filling} = \frac{V_{tot}}{Q_{mean}} \tag{25}$$

The filling flow rate follows a downward curve but remains relatively constant. The average flow rate is therefore used to calculate the characteristic time. The discharge does not follow a constant curve. No pump can control the flow, so the flow follows a first curve, then a second. The first curve corresponds to the volume of the pipes and the part of the tank at the height of the pipes. The second flow rate slope corresponds solely to the tank flow rate. The characteristic time is therefore calculated using Eq. 26.

$$t^*_{\text{emptying}} = \frac{V_{pipes}}{Q_{mean1}} + \frac{V_{tank}}{Q_{mean2}} \tag{26}$$

It can be noted that, by definition, the characteristic time varies according to the configuration and that dimensionless time for configurations will vary between 0 and 1. The different filling levels according to the discharges are presented in Tab. 16. The values for the filling and emptying are shown. Since only gravity is used for emptying, the characteristic time is higher. For filling, it is conditioned by the pump, which allows faster filling.

Filling	Configuration 1	Configuration 2	Configuration 3	Configuration 4
t^*_f [s]	281.33	114.75	82.35	62.06
Emptying	Configuration 1	Configuration 2	Configuration 3	Configuration 4
t^*_e [s]	611.28	321.05	279.33	217.93

Tab. 16 Time to fully fill the pipes by discharges

1.2 Filling results

The experimental results can be compared in a number of ways. Firstly, the results for the different probes will be discussed. Then, the different propagation speeds will be discussed.

Fig. 46 shows the comparison between the four configurations with dimensionless variables at the sensor one. Fig. 47 shows the same comparison with dimension variables. This sensor is the first sensor after the tank.

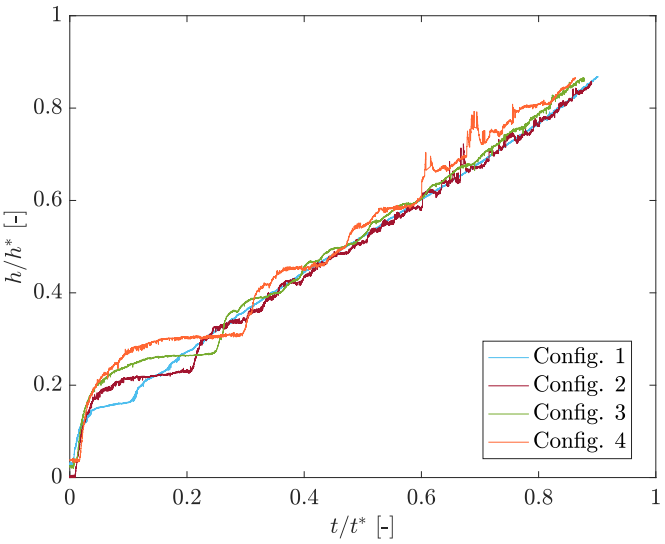

Fig. 46 Comparison between the four configurations for the first sensor with dimensionless variables

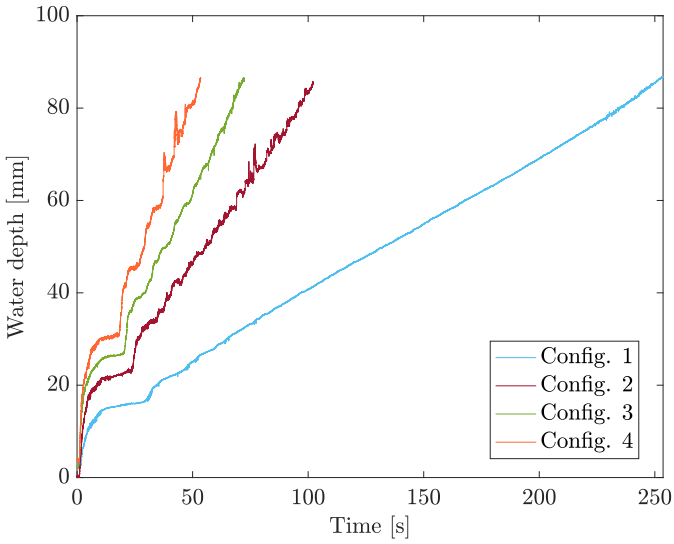

Fig. 47 Comparison between the four configurations for the first sensor with dimension variable

Fig. 46 and Fig. 47 show the difference in amplitude of the wavefront in each configuration. Fig. 47 clearly shows that it takes almost four times longer to fill the pipes in configuration one than in configuration four. Fig. 46 shows that, for configuration four, front propagation accounts for 30 % of the time taken to fill the system. In fact, front propagation is visible up to $t/t^*_{filling}$ equal to 0.3. For configuration one, on the other hand, front propagation represents 10 % of the total filling time. For configurations two and three, it represents 20 % and 25 % respectively.

The analysis is similar for the height of water in the pipe. For the configuration with the highest discharge, the wavefront amplitude represents a greater percentage of the total cross-section than for the configuration with the lowest discharge. For configuration four, the wavefront amplitude represents 36 % of the total cross-section. For the first configuration, it represents only 16 %. This is less than half the amplitude of the fourth configuration. For configurations two and three it represents 25 % and 31 % of the total cross-section.

On Fig. 46, it is not possible to see the difference between the slope of the uniform filling part. This difference can be observed on Fig. 47.

Fig. 48 shows the different configurations at sensor three with dimensionless variables. Fig. 49 shows the different variables at sensor three with dimension variables. The sensor three is on a pipe that is not related to the tank. It is also located near a bend. It is the furthest sensor from the tank.

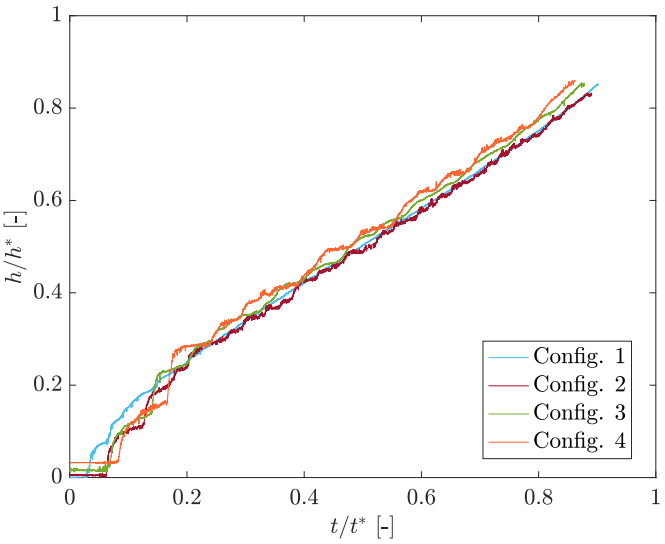

FIG. 48 Comparison between the four configurations for the third sensor with dimensionless variables

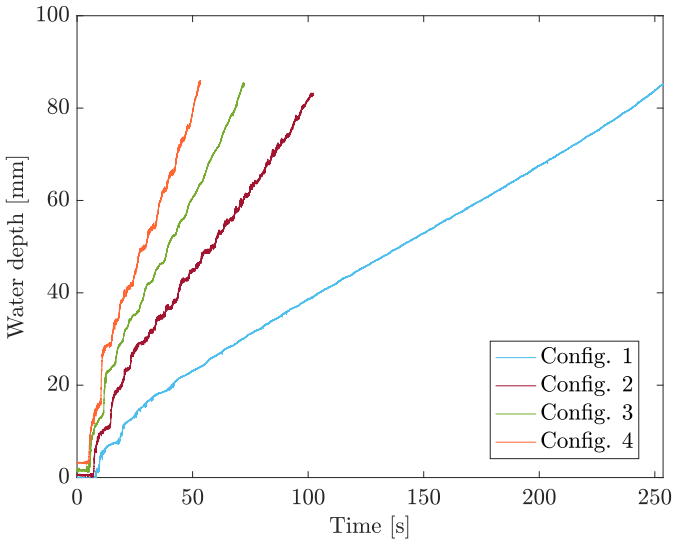

FIG. 49 Comparison between the four configurations for the third sensor with dimension variable

For this sensor, the first stage can be seen more clearly, which is the filling of the pipes. This part was not really visible on the FIG. 46 and FIG. 47 given the proximity of sensor one to the tank. Filling the pipes represents only 5 % of the total filling time for configuration one. For the fourth configuration, this phase accounts for 10 % of the time. When the discharge is low, it takes longer for the water to reach the sensor. This can be seen on FIG. 49 but the total filling time is also much longer than in the other configurations. Filling therefore represents a larger percentage of the filling time for the higher discharges although the times are actually shorter.

Since the sensor is located after an intersection and near a bend, the amplitude of the wavefront is much lower than for sensor one. This can be observed on FIG. 46 and FIG. 47). The propagation of the wavefront corresponds to 10 % of the filling time in configuration four. This corresponds to the same percentage as the filling of the pipes. For the other configurations, the observation is similar. The percentage of wavefront propagation time is similar to the percentage of time for pipe filling. This percentage is higher when the discharges are greater.

Although the amplitude of the wavefront is lower, the conclusions are the same as for the first sensor. The greater the discharges, the greater the amplitude of the wavefront. For the smallest configuration, the wavefront represents only 10 % of the total cross-section. For the last configuration, it represents 15 % of the total cross-section without considering the initial condition. By tanking it into account, at the end of the propagation of the front, it represents 18 % of the total cross-section.

The phase of uniform filling of the galleries represents 80 % of the total filling time for the lowest discharge (configuration one). For the configuration with the highest discharge, this phase represents 70 % of the total filling time. The curves have a similar slope on the FIG. 48 due to dimensionless variables, the different slope can be seen on FIG. 49. The slope of configuration one is four times lower than the one of configuration four.

A comparison of the four configurations at the tank sensor is shown in FIG. 50 and FIG. 51. The FIG. 50 uses dimensionless variables and the FIG. 51 uses dimension variables. Only

the part at and above the pipes is shown. The important thing to note about this sensor is the plateau at the beginning. This plateau corresponds to the critical head. The plateau is not exactly horizontal because the flow rate is not constant. However, as the variation of the flow rate is low, a quasi-horizontal plateau emerges.

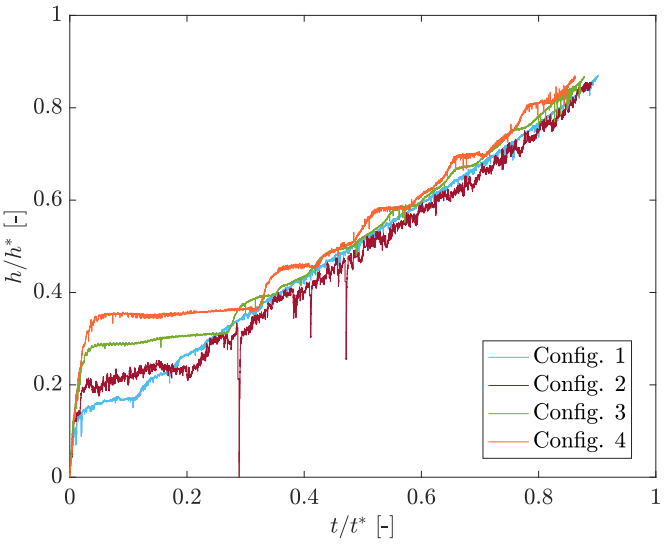

FIG. 50 Comparison between the four configurations for the sensor in the tank with dimensionless variables

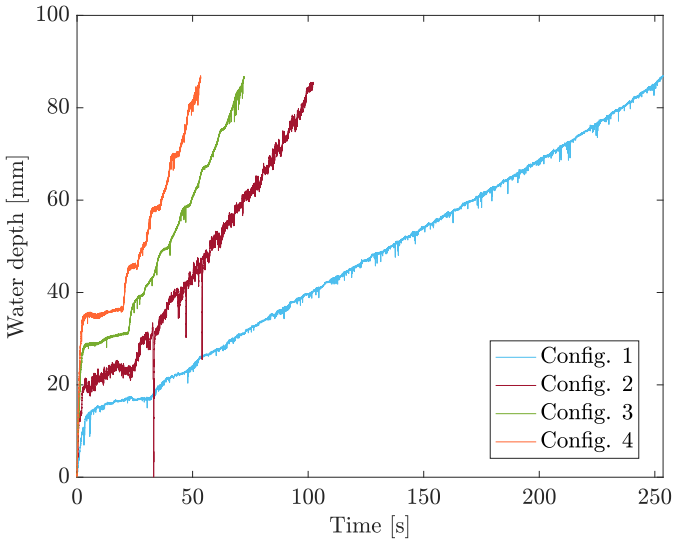

FIG. 51 Comparison between the four configurations for the sensor in the tank with dimension variables

The first observation is the rising slope of the tank, which is the same for all four configurations. For the configuration with the smallest discharges, the tray arrives first. The highest plateau is for the highest discharge. Although, on FIG. 51, the plateau of the first configuration is the longest, it represents a small percentage of the total filling time. It represents 17 % of the total time for the first configuration and 37 % of the total time for the last. However, in terms of duration, it is lower for the largest configuration. The uniform filling curve is similar to those presented for the other two curves.

With the cross-sectional area and flow rate known, it is possible to determine the critical head. The critical head can be compared to the water depth measured by the sensor in the tank. As the sensor is in the centre of the tank, there is no velocity at this point. If there is no velocity, the critical head corresponds to a water depth. TAB. 17 shows the measured head in millimeters and the calculated critical head.

Configuration	Measured head [mm]	Critical head [mm]	Difference [mm]
1	16.45	16.5	0.05
2	25.16	25.4	1.24
3	30.84	30.8	0.04
3	35.93	36.5	0.43

TAB. 17 Measured, calculated critical head and the difference between the two

The difference between the measured and calculated values is always less than 1 mm except for configuration two. The difference remains small as it is less than 1.5 % of the total section.

As sensors are accurate to within 1mm, the differences can come from there. As the plateau is not horizontal, this is an average. The calculation of the critical head is done with a constant discharges. The constant discharge is the average of the discharge recorded during the time of the plateau for each configuration.

Fig. 52 represents the elevation of the water in function of the time for the sensor four, five and six. The elevation is shown instead of the water depth because of the irregularities in the pipes. Pipes are not perfectly straight so there is little difference in the initial water depth.

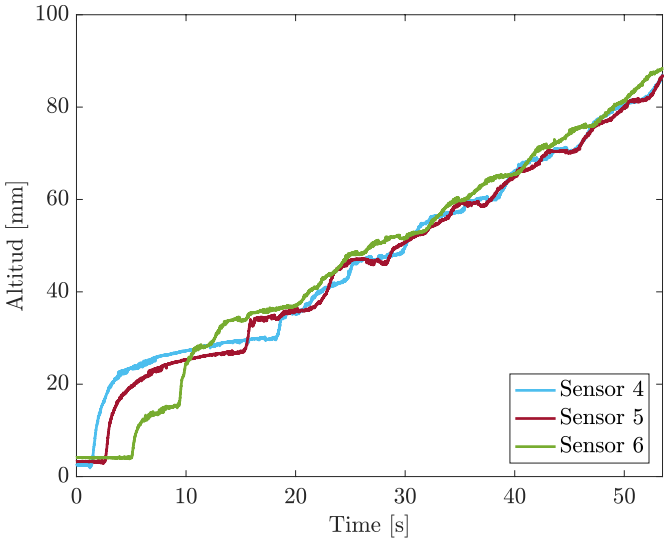

Fig. 52 Evolution of the water depth as a function of the time at sensor four, five and six

By looking at the propagation of the wave front in the pipes, it is possible to calculate the propagation speed. This propagation speed is calculated using two sensors on the same pipe. These are sensors four and five, which are present at Fig. 52. The time at which the wavefront arrives is known. The distance between two probes is also known. Using the scale applied to the setup, it is possible to determine the actual propagation speed in the system. Tab. 18 shows the average discharges for each configuration and the propagation speed for each configuration. This is done for the laboratory and for the real size setup.

Configuration	Average discharge in the laboratory [m^3/s]	Average discharge in reality [m^3/s]	Propagation speed in the laboratory [m/s]	Propagation speed in reality [m/s]
1	$0.5 \cdot 10^3$	50	0.30	3
2	$1.3 \cdot 10^3$	130	0.48	4.8
3	$1.9 \cdot 10^3$	190	0.5	5
4	$2.6 \cdot 10^3$	260	0.54	5.4

Tab. 18 Speed of the wave propagation in the lab and scale to reality

The actual flow rates and propagation velocities are calculated using a Froude similarity. The actual propagation velocities are quite high, even for a low average total flow rate. They range from 3 m/s to more than 5 m/s.

Fig. 53 represents the third discharge. The first three curves represent the first three sensors.

The first is directly connected to the tank. The next two are connected after an intersection. The last two curves are theoretical curves representing the uniform filling of the pipes. Using flow rate and time, the volume can be found. The volume can then be transformed into water head using the cross-section relationship. This is done using the Newton-Raphson method. The flow values are only known over a certain period of time. The purple curve go to the top of the pipe because it is calculated using the average flow shown in Tab. 8. The average water flow for the third discharges is 1.9 l/s.

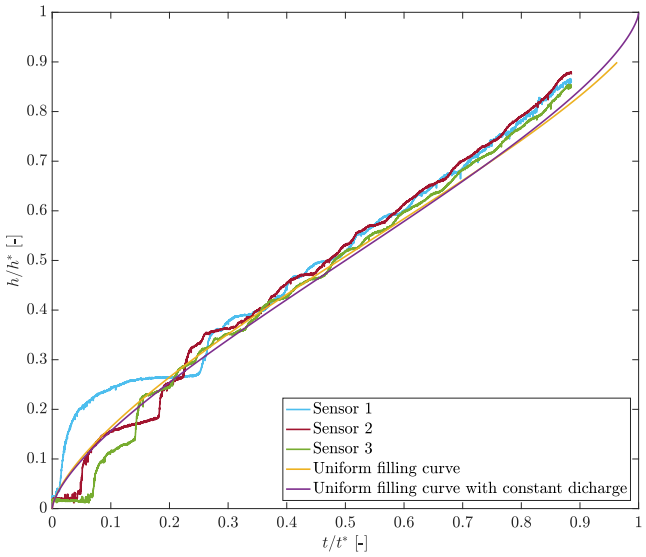

Fig. 53 Three first sensors compared to uniform filling curve and the uniform filling curve calculated with constant discharge

The uniform filling curves are therefore curves and not straight lines, due to the non-linear relationship between height and cross-section. The curve of the first sensor is above the uniform filling curve at the beginning. The wavefront is therefore larger. Then, the experimental curve falls back below it at the end of the wavefront and the start of the reflection. The difference in front size between the curve of sensor one and the curves of sensors two and three is explained by the fact that these two sensors are after an intersection. The quantity of water is therefore divided by two.

Fig. 54 shows the three last sensors curve and the two uniform filling curves for the third configuration that has a mean water flow of 1.9 l/s. The sensor four and five are on the same pipe that is directly connected to the reservoir. The sensor six is after an intersection.

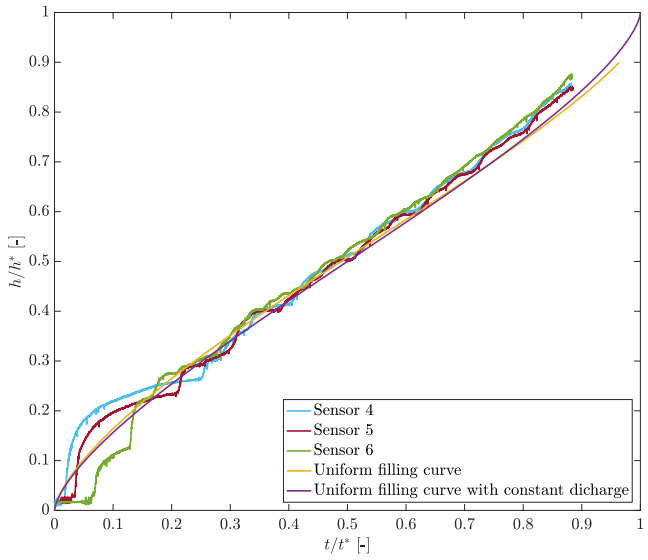

FIG. 54 Three last sensors compared to uniform filling curve and the uniform filling curve calculated with constant discharge

The uniform filling curve falls below the experimental curve for sensors one and two at the start of the front. The experimental curve for sensor one rises up to 8 mm above the theoretical uniform filling curve. The experimental curve of sensor five is below the uniform filling curve at the beginning of the filling. The experimental curve then rises again due to the amplitude of the front. On reflection, the theoretical uniform filling curve falls back below it. The experimental and theoretical curves merge during the uniform filling. The curve for the sixth sensor is constantly below the theoretical curve. As the sensor is after an intersection, the volume of water is halved compared to the other two sensors.

1.3 Emptying results

In this section, the emptying results will be compared. The four configurations will be analysed sensor by sensor. Three sensor will be represented as it is not necessary to analyse all of them since the curves are similar.

FIG. 55 and FIG. 56 show the four emptying configurations at sensor four. FIG. 55 uses dimensionless variables while FIG. 56 uses dimension variables.

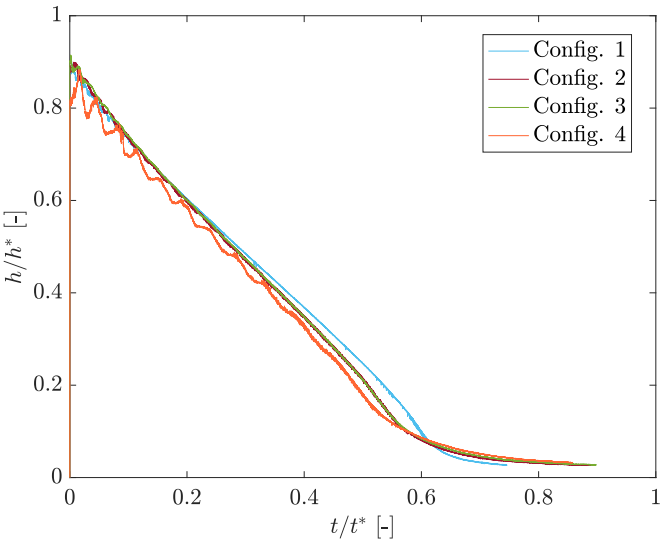

FIG. 55 Comparison between the four configuration for the emptying at the level of the sensor four

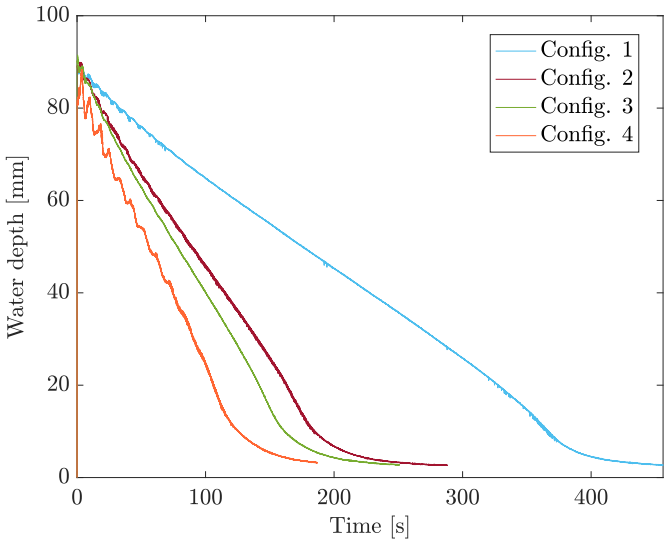

FIG. 56 Comparison between the four configurations for the sensor in the tank with dimension variables

On FIG. 56, the four different slopes can be seen. The first slope corresponds to the part dominated by the pump/turbine. The first part corresponds to the part which is dominated by the opening of the gate. The higher the opening, the higher the slope. This part corresponds to 60 % of the time for emptying the entire system. Thus, with this system, only 60 % can be controlled by the pump/turbine. The forty other percents are controlled by the geometry of the pipe.

In terms of height, only 10 to 15 % is not controlled by the pump/turbine flow. It therefore takes almost as long to empty 85 % of the tank as it does to empty the remaining 15 %. In practice, it is rare for tanks to be completely emptied because of the sediments. Most of the time, there's always a little water in the tank. It would therefore be interesting to leave 15 millimeters of water in the laboratory, which corresponds to 1.5 meters in reality. This height would only be emptied when the tanks are completely emptied, which is rare.

The oscillations at the start of the curve are more noticeable in the configuration with the highest flow rate. In fact, the flow goes from a transient condition to steady state condition several times before stabilising. When the gate is opening, the water in the tank goes down. The water in the galleries is then drawn down by the decrease in water in the reservoir. Once the water in the galleries reaches the water in the reservoir, there is a period of stabilisation. The water in the reservoir falls back down and drags the water from the galleries down again. After a few seconds, this phenomenon stabilises and the oscillations are no longer visible. This phenomenon occurs for all configurations. When the drive flow rate is high, the level in the reservoir rises. This can be seen on the orange curve in FIG. 55 and FIG. 56. These oscillations can also be seen in FIG. 62. Oscillations account for more than 35 % of the total tank emptying time. In terms of height, more than 60 % of the height is emptied during this phase. For the other three configurations, oscillations are present but the water does not rise in the tank. The drive of the water going from the pipes to the tank is not strong enough to make the water rise. Therefore the decrease in water depth can be seen and then a plateau. The water no longer goes down because the water in the pipes fills the tank at the same rate as it empties. The water level therefore stabilises. For the lowest flow rate, the oscillations represent only 10 % of the

emptying time. In terms of height, it represents a reduction of 15 %.

Fig. 57 and Fig. 57 represents the emptying results for the four configurations at sensor six. Fig. 57 uses dimensionless variables and Fig. 58 uses dimension variables.

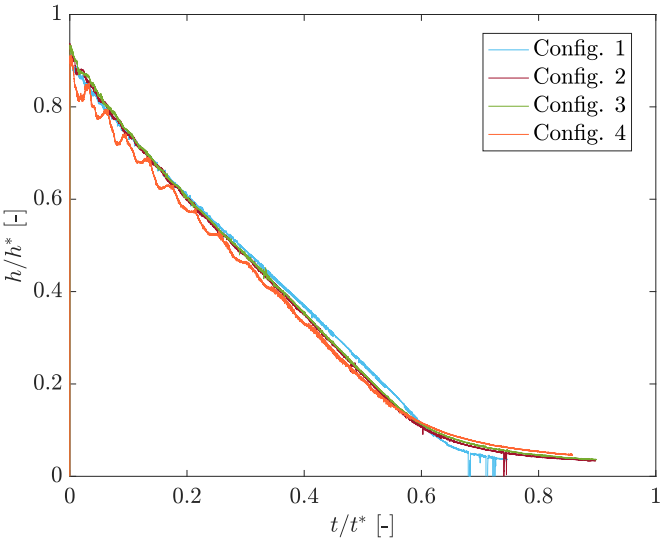

Fig. 57 Comparison between the four configuration for the emptying at the level of the sensor four

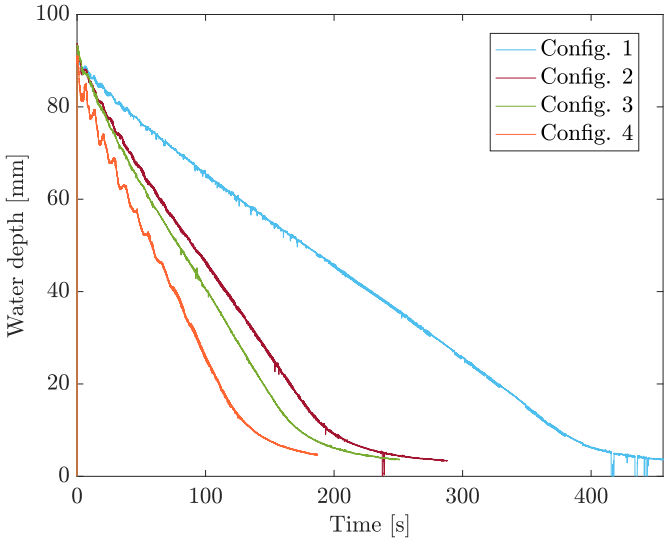

Fig. 58 Comparison between the four configurations for the sensor in the tank with dimension variables

The curves are quite similar to those of Fig. 55 and Fig. 56. Sensor six is the furthest away from the reservoir. There is therefore a slight time lag with the change in water level at sensor four, which is closer to the reservoir. The same phenomena as the other sensor are present. There are oscillations at the beginning which are more present in the fourth configuration. The break in slope is also visible between the part dominated by the pump and the part dominated by the pipe geometry.

The emptying dominated by the pump/turbine represents 65 % of the pipe emptying time. In terms of height, pump/turbine dominance enables 86 % of the total height to be emptied. The principal difference between the two sensor is the percentage of the total time used for the emptying dominated by the pump/turbine. For sensor six, this part represent 65 % and for sensor four it represents 60 %.

Fig. 59 represents the configuration one for sensor four, five and six. Fig. 60 represents the same sensors for configuration four.

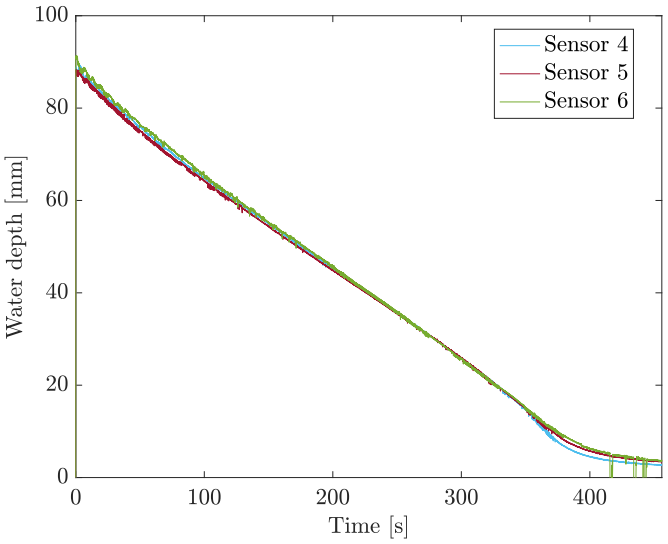

FIG. 59 Comparison between the sensor four, five and six for configuration one

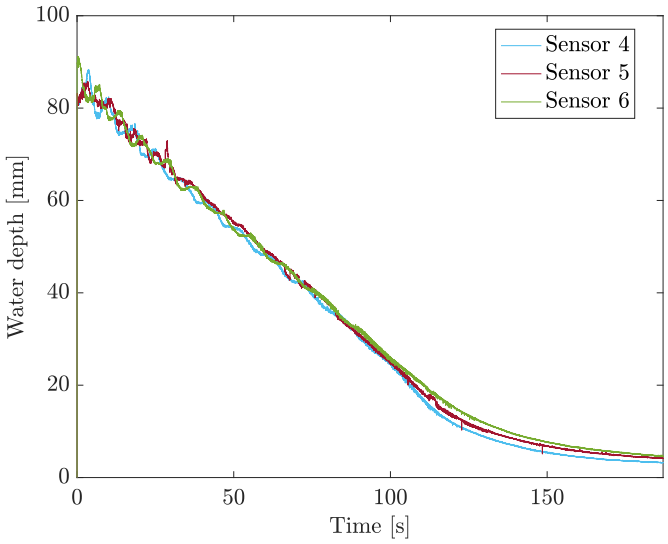

FIG. 60 Comparison between the sensor four, five and six for configuration four

There is no visible difference between the curve of the different sensors when the pipes start to empty. This is fairly instantaneous for each of the steamers. However, for the two configurations shown, the green curve is systematically above the two others. This curve represents the furthest sensor away from the tank. It therefore takes longer to empty the pipe. This curve is above the two others during all the simulations. For the configuration one on FIG. 59, the red curve is lower than the blue curve at the beginning. This can be explained by the fact that the water was not perfectly still when the test began. Thus, there was a height of water 1 mm higher at sensor four than at sensor five. For the two configurations presented, all curve are overlapped before the change of slope. When the slope changes, the blue curve is below the other two curves.

On FIG. 60, oscillations can be seen at the beginning. The oscillations of sensors four and five are in opposition. When water rises in one, the water depth decrease in the other. When the water leaves the tank, it passes in front of the sensor five and then in front of sensor four. First, the water flows out of the pipe and then, there is a moment of transition before the water starts to flow again. This effect can be seen in the curves.

FIG. 61 and FIG. 62 represents the four emptying configurations at the sensor above the reservoir. The black dot line represents the bottom of the pipe, which corresponds to the zero water depth in the pipe. The curve in the negative part corresponds to the evolution of water in the reservoir.

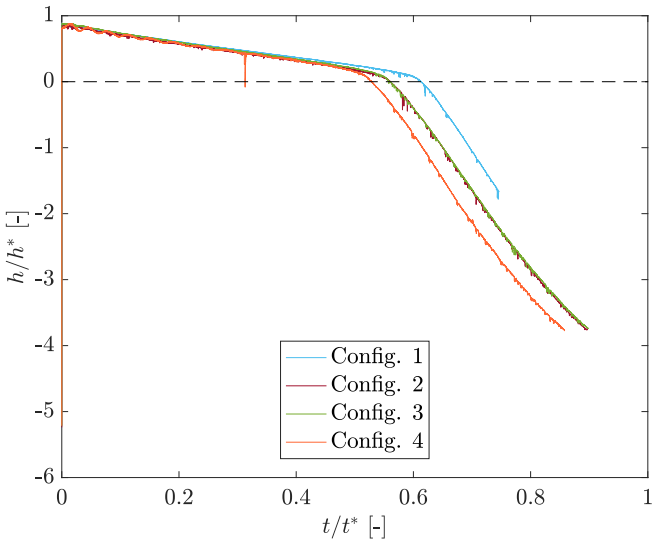

FIG. 61 Comparison between the four configuration for the emptying at the level of the sensor four

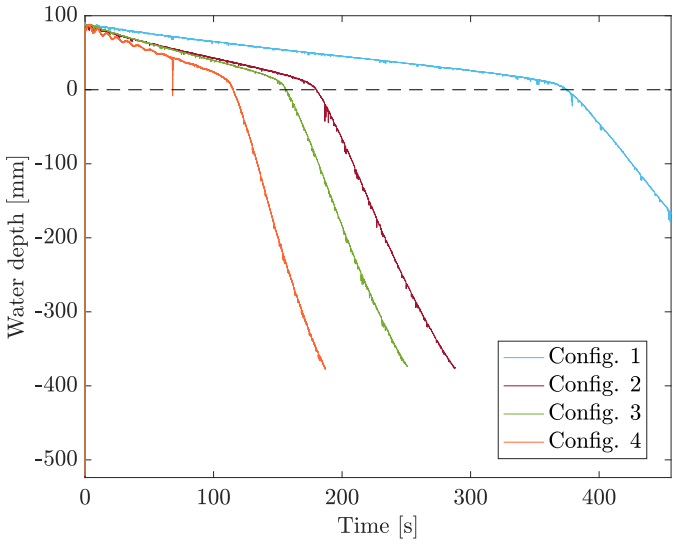

FIG. 62 Comparison between the four configurations for the sensor in the tank with dimension variables

The first slope is therefore similar here for all four configurations. On FIG. 61, using dimensionless variables, the slopes reduced by the geometry of the pipes are parallel. The curves for configurations two and three appear to be overlapped on the FIG. 61. This is due to the fact that the discharges of these two configurations are very close. The difference between the two average discharges is 0.1 l/s. The difference between the two curves can be seen on FIG. 62.

The part below the dotted curve corresponds to the emptying of the tank only. This is conditioned by the geometry of the reservoir. The water in the tank empties, although the pipes continue to run inside the tank. This volume of water is supplied by the water in the pipes, which continues to flow in the reservoir.

2 Real size model

Now that the numerical model has been validated by using laboratory results, it is possible to increase the dimensions of the numerical model. This will enable a full-size model to be produced. Using this full-size model, several parameters will be studied. Firstly, the influence of the flow rate will be studied with real flow rates. Then, the influence of the size of the injection tank will be studied as well as the influence of the friction coefficient for several surface.

This means that the pipes no longer have to be cut to fit the space available in the laboratory. The size of the model is the one that was designed to make the laboratory model. There are no longer any given discharges for input data. A constant flow rate will therefore be given as input to the model. The flow rate chosen is 100 m^3/s.

Characteristic	Value
Diameter	10 m
Section of the pipe	78.54 m^2
Total length	31 920 m
Total volume	2 506 990.93 m^3
Flow rate	80 m^3/s
Total filling time	31 337.9s
K	75 $m^{1/3}/s$

TAB. 19 Important characteristic of the real size setup

The diameter of the pipes is therefore 10 meters and the total length of the pipes is 31.92 kilometers. The galleries are laid out in the same shape as the laboratory. The longest pipe connected to the reservoir is 4570 meters long while the smallest one is 1500 meters. The chosen flow rate is the one used for the calculation of the volume. The influence of different flow rates will be analysed later. The chosen coefficient of friction correspond to a concrete surface. The influence of the friction will be tested later on. It would take 31 337.9 seconds to fill the entire volume of the reservoir. This correspond to less than eight hours. FIG. 63 shows a scheme of the real size model described.

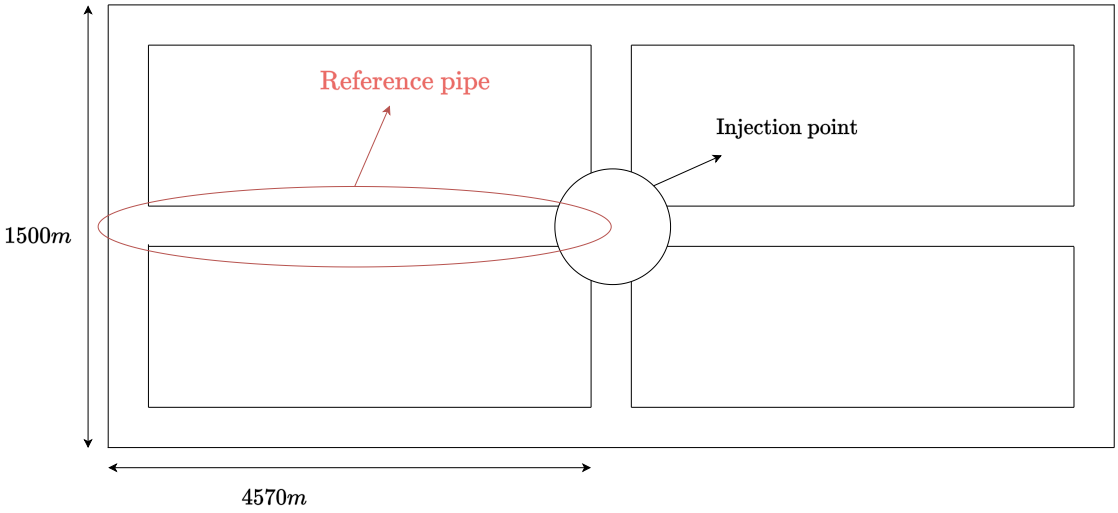

FIG. 63 Scheme of the real size model and location of the reference pipe

This real size model corresponds to the model that was used to create the laboratory model. The pipe surrounded in red is the reference pipe. All the graphs that will be presented in this section represents that reference pipe.

FIG. 64 represent the evolution of the water depth in the reference pipe at 10 meters of the tank. The galleries are initially filled with twenty centimeters. The maximum height in the tank is 8.3 meters so as not to overload the pipes.

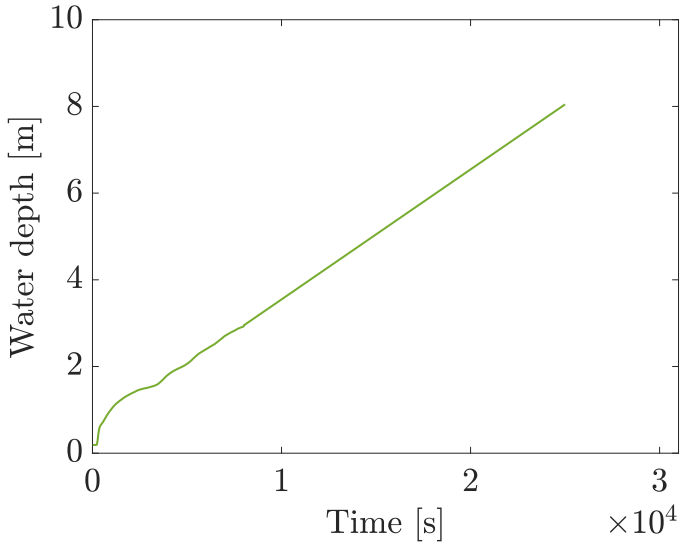

FIG. 64 Evolution of the water depth 10 meters away from the tank for a real size setup

The evolution of the water height in the real size setup is quite similar to the evolution of the water height in the laboratory setup. The first stage is the filling of the pipes. Then, the wave front propagates. This front propagates fairly vertically before spreading. The water height at the end of the wave front propagation is 1.8 meters. After this propagation, some oscillations are observed. There is a transitory period between the propagation of the front and uniform filling. The final and most time-consuming stage is the quasi-uniform filling of the pipes.

FIG. 65 represents the reference pipe. The system is modelled at five time on this profile. This to show the evolution of the water depth in the pipe.

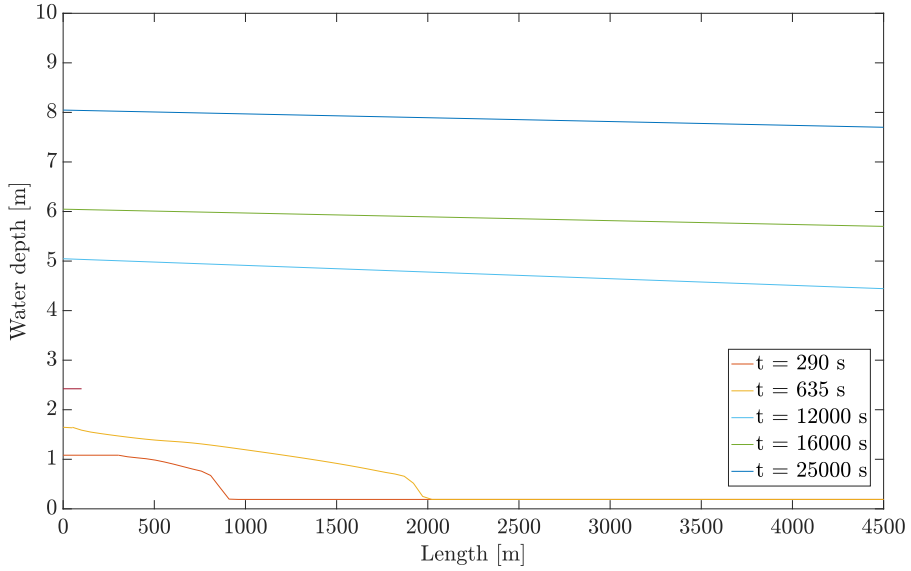

FIG. 65 Longitudinal profile of the reference pipe for a flow rate of 100 m^3/s for five different times

The red curve shows the arrival of the wavefront. This represents the state of of the pipe

after 750 seconds. On the yellow curve, the wavefront attenuates at the end. Thus, the front does not have the same size everywhere. The amplitude at the start of the flow is higher than the red curve, although there is a slight attenuation at the end. Then, for the three last times represented, there is uniform filling. The front spreads quite rapidly, taking only over 1,300 seconds to reach the end of the pipe. That is 21 minutes before the wavefront arrive at the end of the pipe. The wavefront propagation speed is 3.49 m/s. This is still a fairly high speed for this type of system. The following hours of filling are only uniform. The first thirty minutes are the most critical because they consist of the propagation of the wavefront and the reflection. The uniform filling part is less critical.

2.1 Influence of the flow rate

In this section, the influence of the flow rate will be studied. When the flow rate is higher, the filling time also decreases. When it comes to energy storage, filling time is very important. The longer the time, the greater the quantity of energy that can be produced. It is therefore important to have a fairly long filling time. Some storage plants can store energy for several days, and some for just a few hours. Although the filling time decreases as the flow rate increases, the power increases. This factor also needs to be taken into account when designing a storage station.

Tab. 20 shows the different flow rate tested with the corresponding power and filling time. The energy produced is not shown in the table as it is similar for the different flow rates. Its value is 2561.7 MWh.

Flow rate $[m^3/s]$	Power [MW]	Filling time [s]	Filling time [h]
50	183.93	50,139.8	13h50min
100	367.875	25,069.9	6h57min
150	551.81	16,713.3	4h38min
200	735.75	12,535	3h29min
250	919.69	10,028	2h47min

Tab. 20 Different flow rate simulated, associated power and filling time

A flow rate of 50 m^3/s would enable energy to be stored for a whole day. However, the power is quite low, at only 183.93 MW, so the greatest flow rate would only generate power for less than 3 hours. A balance therefore needs to be found. For a real system, it is possible to modulate the power. If the maximum flow of the system (conditioned by the pumps/turbines) is 250 m^3/s, it is not obligatory to turbine at the maximum flow all the time.

Fig. 66 represents the evolution of the water level in the first pipe related to the tank. The position of the water level studied is one meter away from the tank. The water depth goes from 20 centimeters to 8.2 meters. Fig. 67 represents the evolution of the water depth for a discharge of 200 m^3/s. The total duration of the simulation is smaller than in Fig. 66 and the flow rate of Fig. 67 is four time the flow rate of Fig. 66.

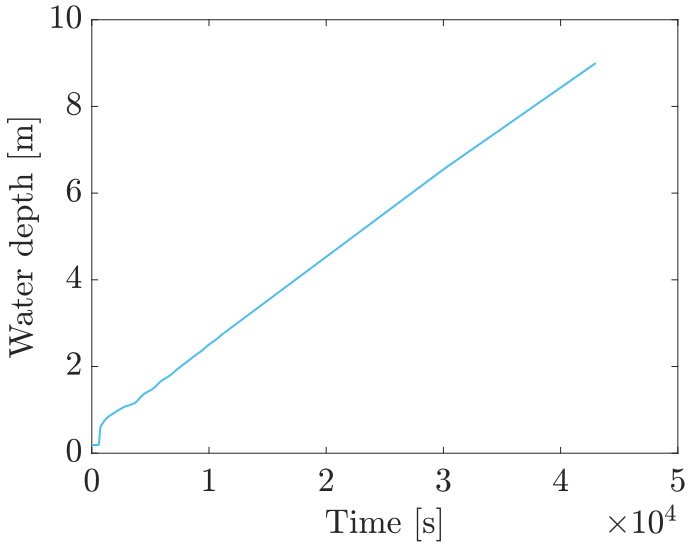

FIG. 66 Evolution of water level as a function of time for a constant flow rate of 50 m^3/s

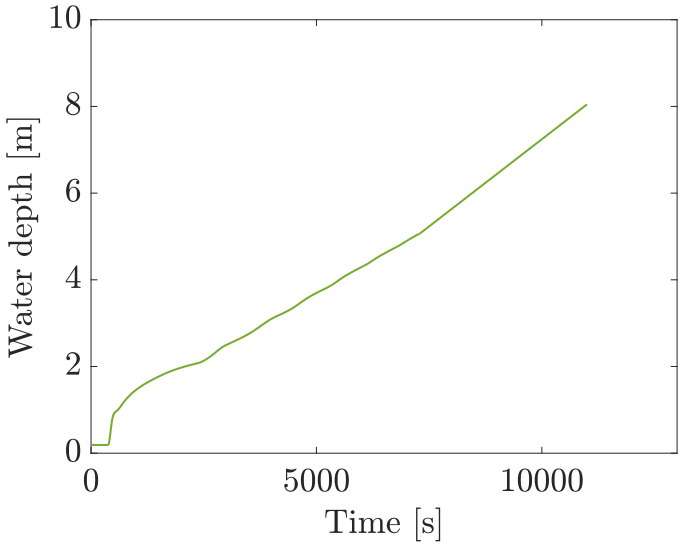

FIG. 67 Evolution of water level as a function of time for a constant flow rate of 200 m^3/s

The biggest difference between the two flow rate is the amplitude of the wavefront. The wavefront of FIG. 66 has en amplitude of 1.2 meters. The wavefront of FIG. 66 has en amplitude of 2 meters. The flow rate is four times higher and the amplitude of the wavefront is only twice as high. The wave front arrives fairly vertically for the two discharges. After the wavefront, there are some oscillations that might be due to the reflection. Then, the uniform filling appears.

FIG. 68 shows the longitudinal profile of the longest pipe related to the tank. The propagation of the wavefront can be seen.

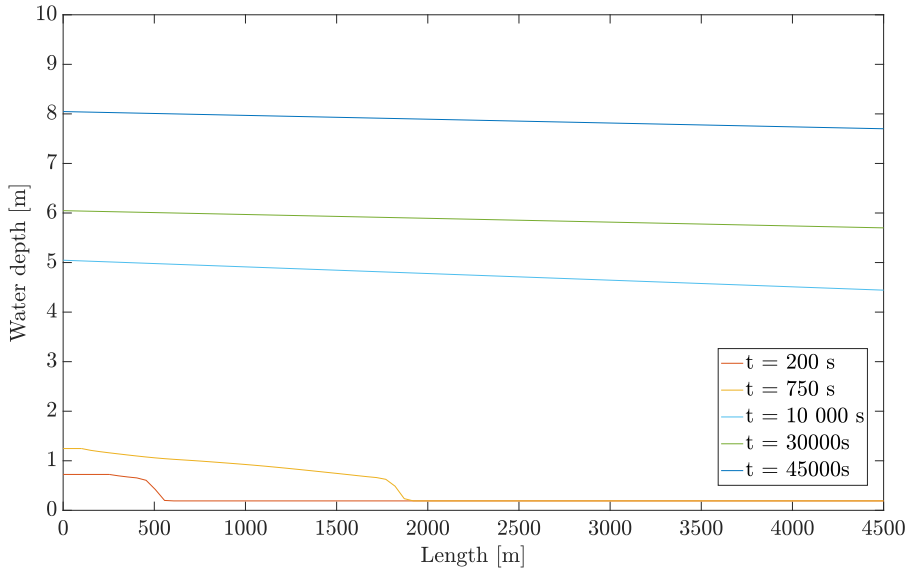

FIG. 68 Comparison between different time step in the longest pipe linked to the tank for a constant flow rate of 50 m^3/s

This profile is quite similar for all of the flow rates. The biggest difference with the other flow rates is the filling time and the amplitude of the wavefront.

Afterwards, the analysis of the propagation speed can be done. The propagation speed is calculated in the same way as above. By observing two selected points on the pipe, the precise time at which the front arrives is known. The distance between the points is known, as is the time difference. This means that the speed is known. The two wavefronts can be seen on Fig. 69. A zoom is made on the pipe to have a better view on the propagation.

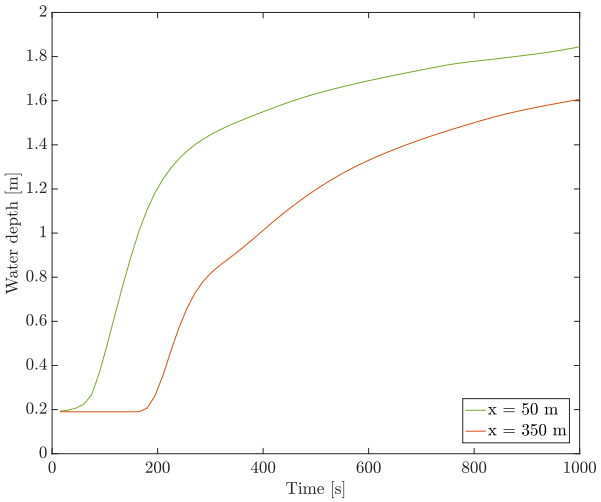

Fig. 69 Propagation of the wavefront

The green curve corresponds to the location which is 50 meters away from the tank. The wavefront arrive after 60 seconds. Then, the orange curve represents the location whih is 350 meters away from the reservoir. The corresponding time for the arrival of the wavefront is 180 seconds.

$$v_{prop} = \frac{\Delta x}{\Delta t} = \frac{300}{120} = 2.5 m/s \tag{27}$$

Tab. 21 shows the propagation speed of the wavefront for each flow rate. All the propagation speeds are calculated with an initial condition of 20 centimeters of water in the pipe. The conditions of friction are also the same.

Flow rate $[m^3/s]$	Propagation speed [m/s]
50	2.50
100	3.49
150	4.56
200	5.11
250	5.31

Tab. 21 Propagation speed of each flow rate

As the flow rate increases, the propagation speed increases as well. The speed increases but not proportionally with the increase of the flow. For a flow rates of 200 m^3/s and 250 m^3/s, propagation speeds are twice the speed propagation of a flow rate of 50 m^3/s. When the flow

rate is increase by five, the propagation speed only double. A propagation speed of more than 5 m/s is quite high for this type of system. The stability of the walls must be ensured with such high wave propagation speeds.

2.2 Influence of the size of the reservoir

The influence of the size of the tank is studied to see what influence it has on the pressurizing or not of the pipe. The aim is never to pressurise the pipes. The injection zone is the critical end point. If this area is pressurised with too much water, the pipes will be pressurised. In the flows tested previously, this area was not pressurised. It is therefore needed to see for which dimensions and flow rates this zone is pressurised.

The water level curve in the reservoir shows a critical flow corresponding to a critical load plateau. Thereafter, the height increases uniformly in the injection zone. This means that the curve follows the uniform filling curve of the pipes. If uniform filling starts before the pipes are pressurised at the injection point, then they will not be pressurised. Once uniform filling begins, the filling has to stop before the water level go to the top of the pipe. The study of the critical head as a function of the size of the tank is therefore needed. If the water depth is close to the top of the pipe, the flow needs to be analysed to see if it can remain a free surface flow.

FIG. 70 represents the influence of the diameter of the injection section on the critical head. The critical load corresponds to a flow where the Froude number is equal to one. This height varies according to the cross-section and the flow rate. The different sections tested in the injection zone are 40 meters, 30 meters, 20 meters and 10 meters. The black dot line represent the top of the pipe. If a point is above this line, the pipes are pressurized. The parameter D_p represent the diameter of the pipes which is ten meters. The parameter D_{res} correspond to the diameter of the reservoir that is a function of the diameter of the pipe. The cross-section used up to now has been four times greater than the cross-section of the pipes. This section does not put any pressure on the pipes.

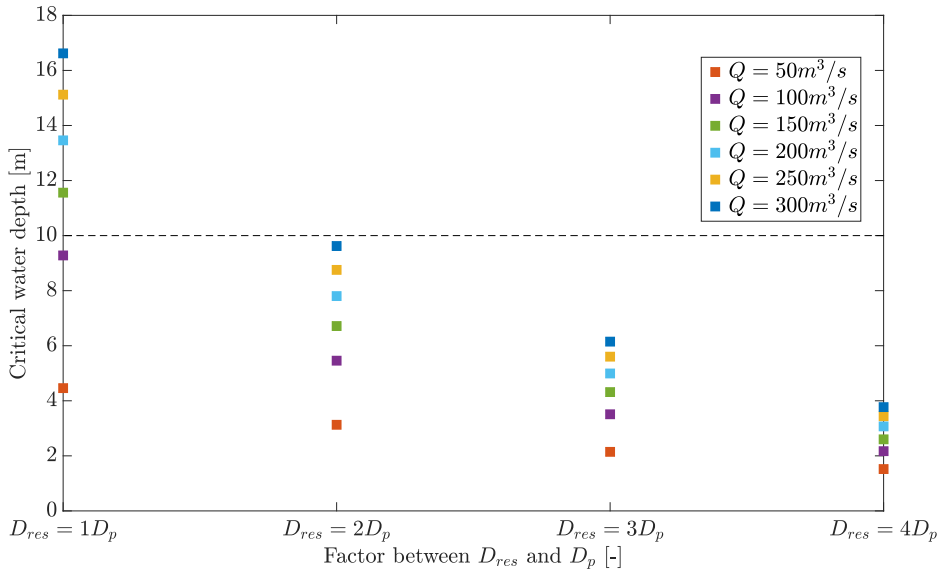

FIG. 70 Different critical head in the entrance section for different flow rate in function of the diameter of the entrance section

When the diameter of the inlet section is three times the diameter of the pipes, the highest height is 6.2 meters, corresponding to a flow rate of 300 m^3/s. This height is still higher than half the pipe. When the injection cross-section is three times larger than the pipe diameter, the heights are quite high. For lower flow rates, there is no problem. The highest flow rate gives a height very close to that of the top of the pipe. It is therefore not possible to have a flow rate of 300 m^3/s for an injection section 20 meters in diameter. The heights corresponding to flow rates of 250 m^3/s and 200 m^3/s are also very close to the top of the pipe. When the diameter of the injection zone is similar to that of the pipes, only two flow rates do not give a critical height greater than the height of the pipe. For a flow rate of 100 m^3/s, the critical water height is less than one meter above the top of the pipe. The other flow rates give critical heights well above the height of the pipes. It is therefore not feasible to have an injection section with the same diameter as that of the pipes unless the flow rate remains very low.

An injection section diameter of four times the diameter of the pipes will be optimal, whatever the flow rate. If the flow rate is high enough, the critical height will not exceed half the pipe diameter. For an injection cross-section three times the diameter of the pipes, there are no problems, even at higher flow rates. If the diameter is increased by a factor of two, the flow rates should remain low. Only the three lowest flow rates tested are suitable. The others do not exceed the height but lead to heights of more than 80 % of the pipe diameter. A cross-section similar to that of the pipes is not feasible except for very small flow rates.

2.3 Influence of the friction coefficient

The coefficient of friction used so far is the one of PVC pipes. This coefficient results in very low friction. In reality, PVC pipes are not an option. The pipes would either simply be made of blasted rock or sprayed concrete. Tab. 22 shows the Manning coefficient used for different materials.

Material	Manning coefficient K $[m^{1/3}/s]$	Manning coefficient n $[s/m^{1/3}]$
PVC	[120 ; 500]	[0.0083 ; 0.002]
Steel	95	0.0105
Concrete	75	0.0133
Blasted rock	[25 ; 45]	[0.04 ; 0.022]

Tab. 22 Manning coefficients for different materials

For the blast rock, the coefficient cannot be known with precision. Indeed, it depends on lots of factors like the host rock and the excavation method. To test this material, two different coefficients will be tested : K = 25 $m^{1/3}/s$ and K = 35 $m^{1/3}/s$. Steel is not considered as a wall covering material. The value is given simply as an indication. It will be used to test the influence of the coefficient of friction as far as possible.

Fig. 71 represents the evolution of the water depth in the reference pipe for different friction coefficient. The flow rate is 200 m^3/s for all of the curves. The point where the evolution of the water depth is shown is 10 meters away from the tank.

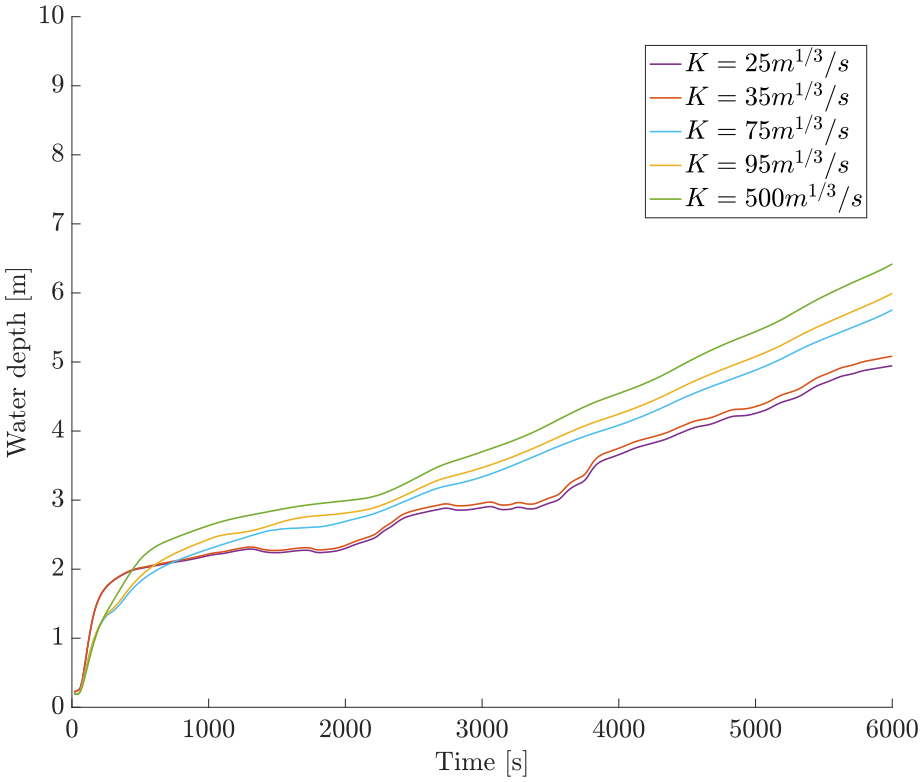

FIG. 71 Evolution of the water depth the reference pipe meters for different friction coefficients

The curve showing the fastest increase is the one with the highest K coefficient and therefore the lowest friction. The two curves representing blasted rock are the lowest ones. These curves also show a fair amount of oscillations. The fastest change in water level is the one of the coefficient representing the least friction. Then, the 95 $m^{1/3}/s$ coefficient is just below it. The blue curve representing concrete is still below the 95 $m^{1/3}/s$ curve. These three curves are quite similar in shape. The only difference is the height of the wavefront.

An interesting parameter to study when analysing the coefficient of friction is the speed of propagation. This speed is calculated as explained above. TAB. 23 represent the different propagation speeds of the wave front for different friction coefficients. The flow rate used for this calculation is 50 m^3/s.

Material	Friction coefficient K	Propagation speed [m/s]
PVC	500	2.73
Rough PVC	100	2.46
Concrete	75	1.76
Blasted rock	35	1.37

TAB. 23 Propagation speed in function of the friction coefficient for a flow rate of 50 m^3/s

It can be seen than the propagation speed decreases with the roughness of the soil. Blasted rock has the lowest propagation speed. There is a factor two between the speed of propagation on PVC and the speed of propagation on blasted rock. There is a difference of 1 m/s between the speed of propagation on PVC and the speed of propagation on concrete. The evolution of

the propagation speed on materials presented in Tab. 23 is shown on Fig. 72.

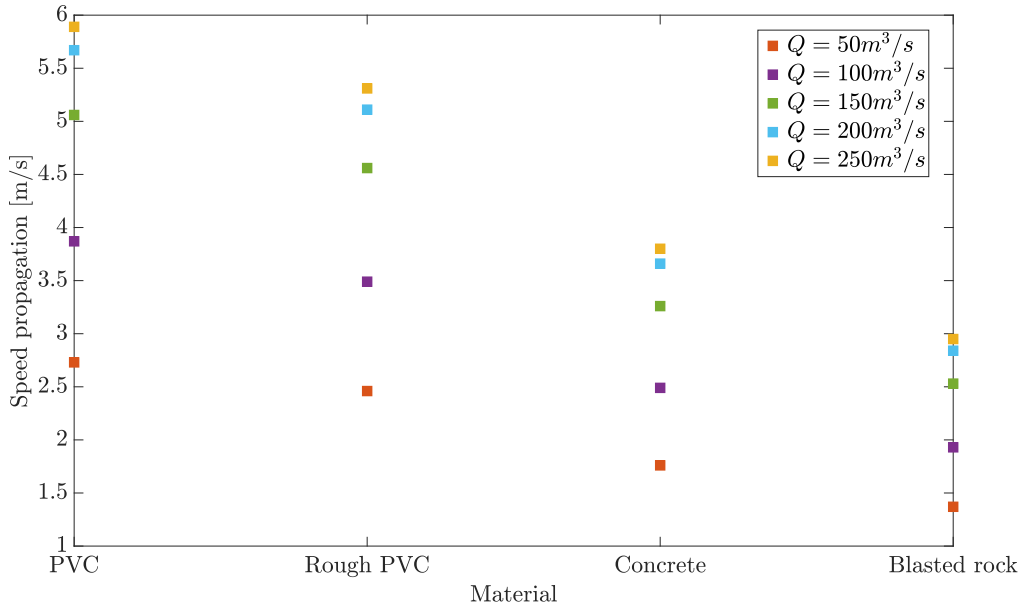

Fig. 72 Speed propagation on different material for five different flow rate

The difference between the K coefficient of 500 and the K coefficient of 100 coefficients of friction represented small friction. As discussed earlier, these coefficients cause virtually no friction. There is therefore only a small difference between the propagation speeds of these different materials. The biggest difference is between the coefficient of 100 corresponding to rough PVC and the coefficient of 75 corresponding to concrete. Concrete causes greater friction and greater loss due to friction. Then, the difference with rock is not as great.

3 Conclusion

The flow rate has an influence on the filling time and the propagation speed. This speed does not increase proportionally with the flow rate. However, propagation velocities remain very high for higher flow rates. The amplitude of the wavefront is also higher when the flow rate increases.

The design of the injection cross-section is also important when deciding whether or not to pressurise the pipes. When the flow rate is higher (more than 250 m^3/s), the injection section must have a diameter at least twice as large as the cross-section of the pipes. Under no circumstances can the diameter of the injection zone be equal to the diameter of the pipes. This would result in critical heights that are too high and would pressurise the injection zone.

Friction has a major influence on propagation speed. The higher the friction, the lower the propagation speed. The factor between the propagation speed of PVC and rock is two. Propagation on rock also causes oscillations that are not present on other surfaces.

Part VII
Perspectives

As mentioned above, there is a lack of information on the subject of underground pumped hydro storages. There are many different aspects to study, including geomechanical, hydraulic and economic aspects. As this master's thesis is being carried out in a fairly short amount of time, it is not possible to cover all the possible aspects. There is still a lot of research to do on the subject.

From a hydraulic point of view, there is still a lot to be done. Studies can be carried out in the laboratory or by using a numerical model. There is very little laboratory data and it would be interesting to have more of it. Other geometries can also be tested. It has been shown in this thesis that a one-dimensional finite volume model can reproduce quite well what is actually happening hydraulically. It is therefore not necessary to use complex three-dimensional models to get an idea of what would happen in reality.

FIG. 73 shows a new interesting geometry to test. The injection is no more in the center of the system ; the injection zone is a long pipe. Several other pipes are related to this injection pipe. The length of all the pipes should be determined as well as their sections.

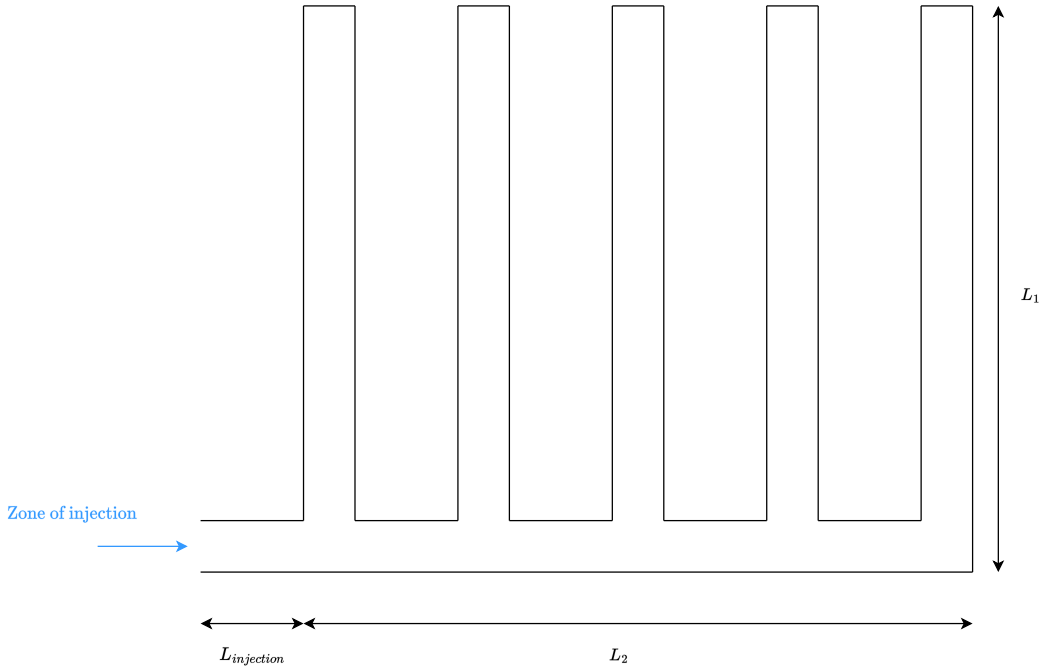

FIG. 73 New geometry to test

The study should be on the hydraulic part as well as the geometry. The geometry of the injection pipe should be analysed and studied.

An important parameter to investigate is friction. This parameter should be studied numerically but also in laboratory. There is no laboratory data on the subject. Tests carried out with a roughness close to reality would enable us to see the impact of it on the flow in the galleries. Tests under real conditions could provide answers to the question of friction. Given that the

main purpose of these structures is to store energy, it would be important to study the loss of charge and energy caused by this roughness.

Another important point from a hydraulic point of view is the injection zone. It would be interesting to test the influence of the number of pipes in the injection zone. In this master's thesis, four pipes were considered. More generally, the shape of the injection zone can be modified. In reality, it will not be arranged as it has been in this study. More realistic geometries should therefore be used.

Feasibility studies also need to be carried out to find out where these systems could be installed. This would provide a better understanding of the local geology and therefore of the geometry that could have been achieved there.

In conclusion, there are still a huge number of aspects to be studied before the first underground pumped storage hydropower station is developed.

Part VIII
Conclusion

In this master's thesis laboratory tests were carried out as well as a numerical model. The numerical model was validated using the laboratory results. A full-scale model was then studied on the basis of the numerical model.

During the laboratory study, two types of test were carried out. Firstly, tests to fill the lower reservoir, which corresponds to energy production. These tests highlighted the different phases of this type of flow. The first ones is the propagation of the wave front. Then, the reflection of this wave front at the bottom of the pipe. The last phase is the uniform filling of the various pipes. The flow in the injection zone was also studied. It confirmed a critical flow at the beginning of a test at the entry of the pipes.

The lower reservoir was then emptied. This is when the water is pumped into the upper reservoir. These tests revealed two phases. The first phase where the flow is directed by the pump/turbine. Then, in the second part of the flow, it is the geometry of the pipes that governs the flow.

A numerical model based on a two-step Range-Kutta scheme is produced. This is validated by using the laboratory results and with theoretical concepts. It is therefore possible, with a one-dimensional model, to reproduce fairly well what happens in the laboratory. This model was used to carry out a simple study of a real case. This setup is capable of storing 2561.7 MWh, and a number of analyses have been carried out to draw conclusions about the model.

Increasing the flow rate essentially affects the time it takes to fill the lower reservoir. The greater the flow rate, the less time the energy can be stored. But the power is obviously greater. The speed of propagation of the wave front and the amplitude of the wavefront, is higher.

It was also analysed that the smaller the injection zone, the lower the flow rate. The study of the critical load in the reservoir showed that when the diameter is four times the diameter of the pipes, flow rates of up to 300 m^3/s can be achieved without any worries about loading the injection zone. This study obviously depends on the flow rate and the geometry chosen. However, it is possible to conclude that the injection zone should be at least twice the size of the pipes for small flow rates. At higher flow rates, the cross section of the injection zone should be at least three to four times the size of the galleries.

A study of friction has identified the differences between several surfacings. A coating of blasted rock gives greater oscillations and a lower propagation speed. Propagation speeds are halved compared with those on PVC. The study was also carried out on a blasted type surfacing. This coating also results in a lower propagation speed than PVC but higher than rock. No large oscillations appear on a surface like concrete.

References

Alvarado, R., Niemann, A., & Schwanenberg, D. (2013). Concepts for pumped-storage hydroelectricity using un-derground coal mines. *Proceedings of*.

Alvarado, R., Niemann, A., & Wortberg, T. (2015). Underground pumped-storage hydroelectricity using existing coal mining infrastructure. *E-proceedings of the 36th IAHR world congress*, *28*.

Belousov, N. (1974). World water power engineering and hydraulic construction.

Erpicum, S., Archambeau, P., Dewals, B., & Pirotton, M. (2017.b). Underground pumped hydroelectric energy storage in Wallonia (Belgium) using old mines - Hydraulic modelling of the reservoirs.

Erpicum, S., Archambeau, P., Dewals, B., Pirotton, M., Pujades, E., Orban, P., Dassargues, A., Cerfontaine, B., Charlier, R., Poulain, A., Goderniaux, P., Ronchi, B., Frippiat, C., & Veschkens, M. (2017). Underground pumped hydro-energy storage in Wallonia (Belgium) using old mines – Potential and challenges.

Erpicum, S., & Dewals, B. (2022). "design and execution of dams and water networks [notes from the course]".

EUROPÉEN, A. P. (2018). Communication de la commission au parlement européen, au conseil, au comité économique et social européen et au comité des régions. *Une stratégie européenne sur les matières plastiques dans une économie circulaire*, 0–22.

Freitag, M., Larcher, M., & Blauhut, A. (2011). The reißeck ii pumped storage power station/das pumpspeicherkraftwerk (pskw) reißeck ii. *Geomechanics and Tunnelling*, *4*(2), 119–128.

Geth, F., Brijs, T., Kathan, J., Driesen, J., & Belmans, R. (2015). An overview of large-scale stationary electricity storage plants in europe: Current status and new developments. *Renewable and Sustainable Energy Reviews*, *52*, 1212–1227.

Goekler, G., & Meusburger, P. (2009). Kops ii on the grid–first experiences and lessons learned. *Proceedings Hydro*, *2009*.

Herzog, P., Voringer, J., Kühner, W., Reiter, F., & Lang, G. (2022). The tauernmoos pumped-storage hydro power plant–energy storage for the austrian railway. *Geomechanics and Tunnelling*, *15*(5), 491–501.

Jacob, T. (1993). *Evaluation sur modèle réduit et prédiction de la stabilité de fonctionnement des turbines francis* (tech. rep.). EPFL.

Kitsikoudis, V., Archambeau, P., Dewals, B., Pujades, E., Orban, P., Dassargues, A., Pirotton, M., & Erpicum, S. (2020). Underground pumped-storage hydropower (upsh) at the martelange mine (belgium): Underground reservoir hydraulics. *Energies*, *13*(14), 3512.

Madlener, R., & Specht, J. M. (2020). An exploratory economic analysis of underground pumped-storage hydro power plants in abandoned deep coal mines.

Menendez, J., Fernandez-Oro, J. M., Galdo, M., & Loredo, J. (2019). Pumped-storage hydropower plants with underground reservoir: Influence of air pressure on the efficiency of the francis turbine and energy production. *Renewable Energy*, *143*, 1427–1438.

Menéndez, J., Fernández-Oro, J. M., Galdo, M., & Loredo, J. (2020a). Efficiency analysis of underground pumped storage hydropower plants. *Journal of Energy Storage*, *28*, 101234.

Menéndez, J., Fernández-Oro, J. M., Galdo, M., & Loredo, J. (2020b). Transient simulation of underground pumped storage hydropower plants operating in pumping mode. *Energies*, *13*(7), 1781.

Menéndez, J., Loredo, J., Galdo, M., & Fernández-Oro, J. M. (2019). Energy storage in underground coal mines in nw spain: Assessment of an underground lower water reservoir and preliminary energy balance. *Renewable Energy*, *134*, 1381–1391.

Microsonic. (accessed in February 2023-a). Extrait de notre catalogue en ligne : Pico+35/wk/i. *pico+ capteurs à ultrasons.*

Microsonic. (accessed in February 2023-b). Extrait de notre catalogue en ligne : Vnp-35/iu/tc. *vnp capteurs à ultrasons.*

Microsonic. (accessed in February 2023-c). Linkcontrol version 7.6 programming of ultrasonic sensors. *EW-DO-021316 Rev. 9-267434.*

miniers majeurs de Wallonie, S. (2011). Candidat au patrimoine mondial de l'unesco, dossier de présentation.

Morabito, A., Spriet, J., Vagnoni, E., & Hendrick, P. (2020a). Underground pumped storage hydropower case studies in belgium: Perspectives and challenges. *Energies*, *13*(15), 4000.

Morabito, A., Spriet, J., Vagnoni, E., & Hendrick, P. (2020b). Underground pumped storage hydropower case studies in belgium: Perspectives and challenges. *Energies*, *13*(15), 4000.

Ortiz, O., Lauters, F., Brunet, L., & Couzon, P.-Y. (2022). Instrumentation de stations de mesure en continu des flux de sédiments en suspension à l'usine de la coche dans les alpes francaises (savoie). *LHB*, 2087541.

Pickard, W. F. (2011). The history, present state, and future prospects of underground pumped hydro for massive energy storage. *Proceedings of the IEEE*, *100*(2), 473–483.

Pirotton, M. (2020). "hydraulique [notes from the course]".

Pujades, E., Willems, T., Bodeux, S., Orban, P., & Dassargues, A. (2016). Underground pumped storage hydroelectricity using abandoned works (deep mines or open pits) and the impact on groundwater flow. *Hydrogeology Journal*, *24*(6), 1531–1546.

Pummer, E., & Schüttrumpf, H. (2018). Reflection phenomena in underground pumped storage reservoirs. *Water*, *10*(4), 504.

Schoenung, S. M., Eyer, J. M., Iannucci, J. J., & Horgan, S. A. (1996). Energy storage for a competitive power market. *Annual review of energy and the environment*, *21*(1), 347–370.

Siemens. (accessed in February 2023). Electromagnetic flowmeters sitrans f m mag 3100. *SITRANS F.*

Wessel, M., Madlener, R., & Hilgers, C. (2020). Economic feasibility of semi-underground pumped storage hydropower plants in open-pit mines. *Energies*, *13*(16), 4178.